T.R.
GEBZE TECHNICAL UNIVERSITY
GRADUATE SCHOOL

COMPUTATIONAL EVALUATION OF CELL MEMBRANE DESTRUCTION BY BACTERIOPHAGE K HOLIN PROTEIN

NURGUL ERAYDIN

A THESIS OF MASTER OF SCIENCE
DEPARTMENT OF BIOTECHNOLOGY

ADVISOR: ASSOC. PROF. MEHMET OZBIL

JULY 2025

T.R.
GEBZE TECHNICAL UNIVERSITY
GRADUATE SCHOOL

COMPUTATIONAL EVALUATION OF CELL MEMBRANE DESTRUCTION BY BACTERIOPHAGE K HOLIN PROTEIN

NURGUL ERAYDIN

A THESIS OF MASTER OF SCIENCE
DEPARTMENT OF BIOTECHNOLOGY

ADVISOR: ASSOC. PROF. MEHMET OZBIL

JULY 2025

T.C.
GEBZE TEKNİK ÜNİVERSİTESİ
LİSANSÜSTÜ EĞİTİM ENSTİTÜSÜ

BAKTERİYOFAJ K HOLİN PROTEİNİ HÜCRE ZARI YIKIMININ HESAPLAMALI DEĞERLENDİRMESİ

NURGUL ERAYDIN

YÜKSEK LİSANS TEZİ
BİYOTEKNOLOJİ ANABİLİM DALI

DANIŞMAN: DOÇ. DR. MEHMET ÖZBİL

TEMMUZ 2025

MASTER of SCIENCE JURY APPROVAL FORM

A thesis submitted by Nurgül ERAYDIN defended on 9/07/2025 before the jury formed with the 30/06/2025 date and 2025/34 numbered decision of the GTU Graduate Administration Board, has been accepted as a MASTER of SCIENCE thesis in the Department of Biotechnology.

JURY

MEMBER (THESIS ADVISOR)	: Assoc. Prof. Dr. Mehmet ÖZBİL
MEMBER	: Assoc. Prof. Dr. Murat Oluş ÖZBEK
MEMBER	: Assist. Prof. Dr. Lalehan ÖZALP

APPROVAL

Gebze Technical University Graduate Administration Board

…..…/…..…/..…… date and ……/…….. numbered decision

SIGNATURE/SEAL

Bal'a…

ABSTRACT

Antibiotic resistance poses a major threat to the treatment of infectious diseases. Holin proteins derived from bacteriophages—which induce bacterial cell lysis by targeting the cell membrane—have attracted attention as alternative therapeutic strategies. This thesis study was conducted to investigate the effects of two different phage-derived holin proteins—phage K and mycobacteriophage D29 - on the cell membranes of antibiotic-resistant pathogens, including the gram-negative *Escherichia coli* (*E. coli*) and gram-positive *Staphylococcus aureus* (*S. aureus*), at the molecular level. The ultimate goal of the study is to analyze the structural impacts of these holins on cell membranes, understand their oligomerization processes, and assess the potential of this knowledge for biotechnological applications.In this context, the holin protein from mycobacteriophage D29 (HolPhage-D29) was modeled in 3D using AI-based modeling (AlphaFold), while the phage K holin protein (HolPhage-K) was modeled using homology modeling. Subsequently, both holin proteins—modeled as monomeric, dimeric, and tetrameric configurations—were embedded into bacterial membrane models specific to their host species, and subjected to molecular dynamics (MD) simulations. Based on the data obtained from the MD simulations, the effects of these proteins on cell membranes were analyzed in detail via structural assessments. Notably, the parallel dimer and tetramer configurations of HolD29 were found to increase membrane compactness and markedly alter lipid ordering, with the protein's C-terminal region exhibiting strong interactions with the membrane.The findings reveal clear insights into the oligomerization strategies of holin proteins, and highlight the C-terminal flexibility as a pivotal factor in membrane destabilization. This study demonstrates that holin proteins can be pre-screened using structure-based approaches—potentially saving significant time and resources ahead of experimental isolation processes. At the molecular level, these insights may serve as a valuable foundation for the future development of phage-based biotechnological tools and peptide models to combat antibiotic-resistant bacteria.

Keywords: Bacteriophage K, *Staphylococcus aureus*, Molecular Dynamics, mycobacteriophage D29, *Escherichia coli*, Holin

ÖZET

Antibiyotiklere karşı gelişen direnç, enfeksiyon hastalıklarının tedavisinde büyük bir tehdit oluşturmaktadır. Bakterileri hedef alarak hücre lizisini tetikleyen bakteriyofaj kaynaklı holin proteinleri, alternatif tedavi stratejileri arasında dikkat çekmektedir. Bu tez çalışması, gram-negatif Escherichia coli (*E. coli*) ve gram-pozitif Staphylococcus aureus (*S. aureus*) gibi dirençli patojenlerde etkili olabilecek iki farklı faja ait – bakteriyofaj K (FajK) ve mikobakteriyofaj D29 (FajD29) – holin proteinin hücre zarına etkisini moleküler düzeyde incelemek amacıyla gerçekleştirilmiştir. Çalışmanın nihai amacı, bu holinlerin hücre zarına olan yapısal etkilerini analiz ederek, oligomerleşme sürecini anlamak ve bu bilgilerin biyoteknolojik uygulamalar için potansiyelini değerlendirmektir.Bu kapsamda, mikobakteriyofaj D29'a ait holin proteini (HolFaj-D29) proteini yapay zekâ destekli modelleme (AlphaFold) ile, Bakteriyofaj-K holin proteini ise (HolFaj- K) proteini ise homoloji modelleme yöntemiyle üç boyutlu olarak modellendi. Ardından her iki holin proteini de, tekli, dimer ve tetramer konfigürasyonlarında, ait oldukları bakteri türlerine özgü zar modelleri ile modellenip Moleküler dinamik (MD) simülasyonlarına maruz bırakıldı. MD simülasyonlarıyla elde edilen veriler doğrultusunda, proteinlerin hücre zarına etkileri yapısal analizlerle detaylı olarak incelenmiştir. Özellikle HolPhage-D29'un paralel dimer ve tetramer yapılarının, zar kompaktlığını artırarak lipid düzenini belirgin şekilde etkilediği, C-terminal bölgesinin ise zarla güçlü bir etkileşim gösterdiği ortaya konmuştur.Elde edilen bulgular, holin proteinlerinin oligomerleşme stratejilerini açıkça ortaya koymuştur. Ayrıca, C-terminal bölgelerin esnekliğinin zar destabilizasyonunda önemli bir rol oynadığı belirlenmiştir. Bu çalışma, holin proteinlerinin yapı-temelli yaklaşımlarla ön taramaya tabi tutulabileceğini ortaya koydu. Böyle bir yaklaşım, deneysel izolasyon sürecinden önce önemli ölçüde zaman ve kaynak tasarrufu sağlayabilir. Moleküler düzeyde elde edilen bu öngörülerin, gelecekte antibiyotik dirençli bakterilere karşı geliştirilecek faj temelli biyoteknolojik araçlar ve peptit modelleri için önemli bir temel oluşturabileceği sonucuna varılmıştır.

Anahtar Kelimeler: Bakteriyofaj K, *Staphylococcus aureus*, Moleküler Dinamik, Mikobakteriyofaj D29, *Escherichia coli*, Holin

ACKNOWLEDGEMENTS

First and foremost, I would like to express my sincere gratitude to my advisor, Assoc. Prof. Mehmet Özbil, with whom I have had the privilege of working for seven years, starting from my undergraduate education. His academic dedication, patience, guidance, and the scientific perspective he has helped me develop have been invaluable. Working with him has been a tremendous opportunity not only for my academic but also for my personal growth.

I would like to thank Gizem Nur Duran, a PhD student who has made the greatest contribution to my learning and whose support I have always felt throughout this journey. My heartfelt thanks go to my dear friend Sinem Nur Açıkgöz, who has shared every moment of my undergraduate and graduate education, standing beside me through every step of the way. I also thank my beloved friends Semanur Bulut and Görkem Güngör, whose friendship and support have never wavered. I am also grateful to Dr. Lalehan Özalp for her valuable contributions and kind support.

Although I cannot mention each one by name, I would like to thank all members of the Computational Biochemistry Group, of which I am proud to be a part, for their contributions to my personal development and the inspiration they have provided.

I would also like to extend my thanks to Ezgi Yiğit and Kübra Demiral, who have always been with me emotionally and never let me feel alone. I am deeply grateful to all the professors from whom I took courses during my graduate studies, for sharing their knowledge and experience with me.

I would also like to thank TÜBİTAK ULAKBİM for providing the computational resources, and Gebze Technical University for making this research possible.

To my family, who have always stood by me with unconditional love and support I extend my deepest gratitude.

And of course… to my beloved husband, Türker Samet Eraydın, who has been my greatest source of strength during this challenging and intense process, as he has been in every moment of my life. Thank you for never letting go of my hand and for always supporting me with faith and love.

I extend my heartfelt thanks to all the individuals and institutions who contributed to, supported, and inspired the development of this thesis

TABLE OF CONTENTS

	Page
ABSTRACT	vi
ÖZET	vii
ACKNOWLEDGEMENTS	viii
TABLE of CONTENTS	ix
LIST OF SYMBOLS AND ABBREVIATIONS	xi
LIST OF FIGURES	xiii
LIST OF TABLES	xvi
1. INTRODUCTION	1
1.1. Bacteria	1
1.1.1. History of Bacteria Discovery	1
1.1.2. Cellular Structure of Bacteria	2
1.1.3. Pathogen Bacteria and Treatment Alternatives	6
1.1.4. Antibiotic Resistance	7
1.1.5. *Escherichia coli* (*E. coli)*	8
1.1.6. *Staphylococcus aureus (S. aureus)*	9
1.1.7. Alternative Treatment	10
1.2. Bacteriophages	11
1.2.1. General Structure and Infection Mechanism	11
1.2.2. Phage Based Infection Treatment Strategies	13
1.2.3. Computer-Aided Phage Therapy Strategies	14
2. AIM OF STUDY	16
3. METHOD	18
3.1. Holin Structure Prediction	18
3.1.1. Theory of Protein Structure Prediction	18
3.1.1.1. Experimental Methods	18
3.1.1.2. Computational Methods	19
3.1.2. HolPhage-D29 Structure Prediction with AI Based Approach	23
3.1.3. HolPhage-K Structure Prediction with Homology Modelling.	24
3.2. Molecular Dynamics Simulations	25
3.2.1. Theory of Molecular Dynamics Simulations	25
3.2.2. *E. coli* Cell Membrane Modeling and MD Simulations	31
3.2.3. HolPhage-D29 Protein- Membrane System Modeling and MD Simulations	33
3.2.4. HolPhage-D29 C-terminal Domain & Membrane System Modeling and MD Simulations	34
3.2.5. *S. aureus* Cell Membrane Modeling and MD Simulations	36
3.2.6. HolPhage-K Protein Membrane System Modeling and MD Simulations	37

4. RESULT 40
4.1. AI Based Protein Modelling of HolPhage-D29 40
4.2. Homology Modelling of HolPhage-K 43
4.3. Molecular Dynamics Simulations 44
4.3.1. *E. coli* Cell Membrane Modeling and MD Simulations 44
4.3.2. *E. coli* Cell Membrane & HolPhage-D29 MD Simulations 46
4.3.3. *E. coli* Cell Membrane & HolPhage-D29 Dimer MD Simulations 52
4.3.3.1. *E. coli* Cell Membrane & HolPhage-D29 (Alongside) Dimer MD Simulations 52
4.3.3.2. *E. coli* Cell Membrane & HolPhage-D29 (Cross) Dimer MD Simulations 57
4.3.4. *E. coli* Cell Membrane & HolPhage-D29 Dimer MD Simulations 63
4.3.5. *E. coli* Cell Membrane & HolPhage-D29 C-terminal Domain MD Simulations 68
4.3.6. *S. aureus* Cell Membrane Modeling and MD Simulation 72
4.3.7. *S. aureus* Cell Membrane & HolPhage-K MD Simulations 74
4.3.8. *S. aureus* Cell Membrane & HolPhage-K Dimer (Alonside) MD Simulations 79
4.3.9. *S. aureus* Cell Membrane & HolPhage-K Tetramer (Cross) MD Simulations 86
5. DISCUSSION & CONCULUSION 93
5.1. DISCUSSION 93
5.1.1. Evaluation of Structural Quality and Modeling Confidence of HolPhage-D29 and HolPhage-K 93
5.1.2. Effect of HolPhage-D29 on E. *coli* Membrane Structure 94
5.1.3. Effects of HolPhage-D29 Dimers on *E. coli* Membrane Structure and Holin Oligomerization Dynamics 95
5.1.4. Effects of HolPhage-D29 Tetramer on *E. coli* Membrane Structure and Holin Oligomerization Dynamics 95
5.1.5. Effects of HolPhage-D29 C-terminal on *E. coli* Membrane Structure 97
5.1.6. Effect of HolPhage-K on *S. aureus* Membrane Structure 98
5.1.7. Effects of HolPhage-K Dimer and Tetramer on *S.aureus* Membrane Structure and Holin Oligomerization Dynamics 98
5.1.8. Importance of Cell Membrane Thickness Changes 100
5.2. CONCULUSION 100

REFERENCES 103
BIOGRPHY 118
PUBLICATIONS AND PRESENTATIONS FROM THE THESIS 119

LIST OF SYMBOLS AND ABBREVIATIONS

π	:	Pi number
Φ	:	Phi angle
Ψ	:	Psi angle
Å	:	Angstrom
AI	:	Artificial Intelligance
AMBER	:	Assisted Model Building with Energy Refinement
AR	:	Antibiotic resistance
APH	:	Amphipathic Helix
bp	:	Base Pairs
CASP14	:	Critical Assessment Of Protein Structure Prediction Competition
CHARMM	:	Harvard Macromolecular Mechanics
CL	:	Cardiolipin
DNA	:	Deoxsyribo Nucleic Acid
dsDNA	:	Double Stranded Deoxsyribo Nucleic Acid
E. coli	:	*Escherichia coli*
EHEC	:	*Enterohemorrhagic E. coli*
EPEC	:	*Enteropathogenic E. coli*
ESBL	:	*Extended Spectrum Beta-Lactamases*
ETEC	:	*Enterotoxigenic E. coli*
F	:	Force
fs	:	Femtosecond
FCOL	:	Fraction Of Contact With The Opposite Leaflet
FMO	:	Fraction Of Mass Overlap
GROMOS	:	Groningen Molecular Simulation
GTU	:	Gebze Technical University
HUS	:	Hemolytic Uremic Syndrome
HolPhage-K	:	Phage K Holin Protein
HolPhage-D29	:	Mycobacteriophage D29 Holin Protein
IBMV	:	Institute of Bacteriophage Microbiology and Virology
K	:	Celvin
kDa	:	Kilodalton
LINCS	:	Linear Constraint Solver
LPS	:	Lipopolysaccharide
LPG	:	Lysin-phosphatidylglycerol
MD	:	Molecular Dynamics
MDR	:	Multidrug resistance
MM	:	Molecular Mechanic
MRSA	:	Methicillin- Resistant *S. aureus*
MSA	:	Multiple Sequence Alignment
N	:	Nuber of Mole
NAG	:	N-acetylglucosamine
NAM	:	N-acetylmuramic acid
NCBI	:	National Center for Biotechnology Information
Nm	:	Nanometer
NMR	:	Nuclear Magnetic Resonance
NVT	:	Canonical Ensemble
NPT	:	Isobaric-Isothermal Community

OPLS	:	Optimized Potentials for Liquid Simulations
ORF	:	Open Reading Frame
P	:	Pressure
PBC	:	Periodic Boundary Conditions
PDB	:	Protein Data Base
PE	:	Phosphatidylethanolamine
PhageD29	:	Mycobacteriophage D29
Phage-K	:	Bacteriophage K
PG	:	Phosphatidylglycerol
PFE	:	Pore-Forming Toxins
PME	:	Particle-Mesh Ewald
pLDDT	:	Predicted Local Distance Difference Test
ps	:	Picosecond
Rg	:	Radius of Gyration
RMD	:	Root Mean Standar Deviation
RNA	:	Ribo Nucleic Acid
S. aureus	:	*Staphylococcus aureus*
SASA	:	Solvent Accessible Surface Area
SEM	:	Screening Electron Microscopy
SPC	:	Single Point Charge
T	:	Temperature
TA	:	Teioic Acid
TIP3P	:	Three Point Model
TIP4P	:	Four Point Model
TIP5P	:	Five Point Model
TEM	:	Transmission Electron Microscopy
TMD	:	Transmembrane Domains
TSST-1	:	Toxic shock syndrome toxin-1
V	:	Volume
VRSA	:	Vancomycin- Resistant S. aureus
WOR	:	Width Of The Overlap Region

LIST OF FIGURES

	Page
Figure 1.1: General structure of bacteral cell membrane	3
Figure 1.2: Peptidoglycan structure	4
Figure 1.3: Gram positive and negative bacterial cell wall structure	4
Figure 1.4: Comparision of gram positive and negative cell wall systems	6
Figure 1.5: SEM Structure of *E. coli*	9
Figure 1.6: TEM Structure of S. aureus	10
Figure 1.7: Phage infection strategy on gram positive cell membrane	12
Figure 2.1: Workflow of this thesis study	17
Figure 3.1: Basic working prenciple of Alphafold	20
Figure 3.2: Steps of Homology Modelling technique	23
Figure 3.3: Sytem models subjected to MD simulations	34
Figure 3.4: Sytem models prepared to MD simulations	37
Figure 4.1: TMD sequence coverage graph obtained as a result of MSA	40
Figure 4.2: pLDDT values for five different TMD models	41
Figure 4.3: PAE maps of five different TMD models	42
Figure 4.4: C-terminal coverage graph obtained as a result of MSA	42
Figure 4.5: pLDDT values for five different C-terminal models	43
Figure 4.6: PAE maps of five different C-terminal models	43
Figure 4.7: Ramachandran plot analysis for HolPhage-K 3D model.	44
Figure 4.8: RMSD, SASA, Rg analyses for *E. coli* Cell membrane MD simulations.	45
Figure 4.9: Snapshots from MD simulation of *E. coli* cell membrane	46
Figure 4.10: RMSD, SASA, Rg analyses for *E. coli* Cell membrane MD simulations.	47
Figure 4.11: Comperative results of RMSD, SASA, Rg analyses for *E. coli* Cell Membrane and HolPhage-D29 Simulation	47
Figure 4.12: Snapshots from MD simulation of HolPhage-D29	48
Figure 4.13: Bendix analysis for HolPhage-D29.	49
Figure 4.14: Curvature analysis of HolPhage-D29 C-terminal segment	50
Figure 4.15: Correlation based leaflet overlap, FMO and WOR analysis for HolPhage-D29.	51
Figure 4.16: Thickness map and avarage thickness analysis for HolPhage-D29	52
Figure 4.17: RMSD, SASA, Rg analyses for HolPhage-D29 dimer – alongside MD simulations	53
Figure 4.18: Comperative results of RMSD, SASA, Rg analyses for *E. coli* Cell Membrane and HolPhage-D29 dimer Simulation	53
Figure 4.19: Snapshots from MD simulation of HolPhage-D29 dimer	54
Figure 4.20: Location of HolPhage-D29 dimer – alongside in *E. coli* cell membrane and its relationship with various lipid species	55
Figure 4.21: Comparison of the time-varying distances between the Ala105 residue on chain A and B	55
Figure 4.22: Thickness map and avarage thickness analysis for HolPhage-D29 dimer – alongside	56
Figure 4.23: Correlation based leaflet overlap, FMO and WOR analysis for HolPhage-D29 dimer – alongside.	57

Figure 4.24: RMSD, SASA, Rg analyses for HolPhage-D29 dimer – cross MD simulations 57
Figure 4.25: Comperative results of RMSD, SASA, Rg analyses for *E. coli* Cell Membrane and HolPhage-D29 dimer (cross) Simulation 58
Figure 4.26: Snapshots from MD simulation of HolPhage-D29 dimer cross 58
Figure 4.27: Bendix analysis of the TMD regions of HolPhage-D29 cross dimer. 59
Figure 4.28: Distance analysis of selected residues in the HolPhage-D29 dimer 60
Figure 4.29: Time-lapse snapshots of HolPhage-D29 dimer cross
Figure 4.30: Thickness map and avarage thickness analysis for HolPhage-D29 dimer – cross 61 62
Figure 4.31: Correlation based leaflet overlap, FMO and WOR analysis for HolPhage-D29 dimer – cross 63
Figure 4.32: RMSD, SASA, Rg analyses for HolPhage-D29 teramer MD simulations 64
Figure 4.33: Comperative results of RMSD, SASA, Rg analyses for *E. coli* Cell Membrane and HolPhage-D29 tetramer Simulation 64
Figure 4.34: Snapshots from MD simulation of HolPhage-D29 tetramer
Figure 4.35: Curvature analysis of three distinct regions of HolPhage-D29 tetramer 65 66
Figure 4.36: Thickness map and avarage thickness analysis for HolPhage-D29 tetramer 67
Figure 4.37: Correlation based leaflet overlap, FMO and WOR analysis for HolPhage-D29 tetramer 68
Figure 4.38: RMSD, SASA, Rg analyses for HolPhage-D29 C-terminal
Figure 4.39: Comperative results of RMSD, SASA, Rg analyses for *E. coli* Cell Membrane and HolPhage-D29 C-terminal 69 69
Figure 4.40: Snapshots from MD simulation of HolPhage-D29 C-terminal 70
Figure 4.41: Thickness map and avarage thickness analysis for HolPhage-D29 C-terminal 72
Figure 4.42: Correlation based leaflet overlap, FMO and WOR analysis for HolPhage-D29 C-terminal 72
Figure 4.43: RMSD, SASA, Rg analyses for *S.aureus* Cell Membrane MD simulations 73
Figure 4.44: Snapshots from MD simulation of *S.aureus* Cell Membrane
Figure 4.45: RMSD, SASA, Rg analyses for HolPhage-K MD simulations 73 74
Figure 4.46: Snapshots from MD simulation of HolPhage-K
Figure 4.47: Bendix analysis of HolPhage-K MD simulations 75
Figure 4.48: Comperative results of RMSD, SASA, Rg analyses for *S.aureus* Cell Membrane and HolPhage-K 76 77
Figure 4.49: Thickness map and avarage thickness analysis for HolPhage-K 78
Figure 4.50: Correlation based leaflet overlap, FMO and WOR analysis for HolPhage-K

Figure 4.51: RMSD, SASA, Rg analyses for HolPhage-K dimer MD Simulations 79
Figure 4.52: Comperative results of RMSD, SASA, Rg analyses for *S.aureus* Cell Membrane and HolPhage-K dimer 80
Figure 4.53: Snapshots from MD simulation of HolPhage-K dimer
Figure 4.54: Relative positions of the monomers forming the HolPhage-K dimer 80
Figure 4.55: Secondary structure evolution of HolPhage-K dimer chains 81
Figure 4.56: Thickness map and avarage thickness analysis for HolPhage-K dimer 82
Figure 4.57: Representative structure of interactions the Met-1 residue located in the N-terminal region of HolPhage-K dimer. 83 84
Figure 4.58: Correlation based leaflet overlap, FMO and WOR analysis for HolPhage-K dimer 85
Figure 4.59: RMSD, SASA, Rg analyses for HolPhage-K teramer MD Simulations 86
Figure 4.60: Snapshots from MD simulation of HolPhage-K tetramer
Figure 4.61: Position change of HolPhage-K tetramer during MD simulations 87
Figure 4.62: Comperative results of RMSD, SASA, Rg analyses for *S.aureus* Cell Membrane and HolPhage-K tetramer 88 89
Figure 4.63: Thickness map and avarage thickness analysis for HolPhage-K tetramer 90
Figure 4.64: Correlation based leaflet overlap, FMO and WOR analysis for HolPhage-K tetramer 91

92

LIST OF TABLES

	Page
Table 3.1: Sytem models prepared to MD simulations.	35
Table 3.2: Sytem models prepared to MD simulations	39

1. INTRODUCTION

1.1 Bacteria

Bacteria are unicellular, prokaryotic microorganisms that can thrive in a wide variety of environments, including water, air, soil, and extreme habitats such as hot springs or deep oceans. It is estimated that there are approximately 40 million bacteria in a single gram of soil, and around one million bacteria in a milliliter of freshwater **[1]**.

1.1.1. History of Bacteria Discovery

Antonie van Leeuwenhoek first mentioned the existence of bacteria in 1676 **[2]**. Initially, Leeuwenhoek referred to them as “animalcules.” Term "bacterium" is derived from Greek words "bakterion" (meaning small rod) and "baktros" (meaning staff or stick) **[3]**. Term was first used by the German scientist Christian Gottfried Ehrenberg in 1838. Following Leeuwenhoek, French chemist and microbiologist Louis Pasteur identified the role of microorganisms in fermentation and decay processes **[4], [5]**. Another significant figure in the discovery of bacteria was the German physician Robert Koch, known for his work on pathogenic bacteria and demonstrating their link to diseases **[6]**. In 1876, Koch isolated and observed *Bacillus anthracis* under the microscope, marking the first example supporting the notion that specific pathogens can cause bacterial diseases **[7]**. The bacteria that Koch isolated was *Mycobacterium tuberculosis*. Thus, it was experimentally proven that these bacteria caused tuberculosis **[8]**. This led to development of the idea that a bacteria could be the cause of a specific illness. Koch formulated “Postulates”, which were used to prove that bacteria lead to diseases **[9]**. The work of Robert Koch demonstrated that microorganisms are the primary cause of diseases and established fundamental principles regarding bacteria **[10]**. Following the revelation that bacteria could cause diseases, efforts shifted towards the treatment of these conditions. Bacteriologist Alexander Fleming discovered that the mold *Penicillium notatum* produced a natural antibiotic effective against bacteria in 1928 **[11]**. Discovery of penicillin marked the

beginning of the antibiotic era. Research on bacteria gained significant momentum in the 1940s and 1950s, leading to important discoveries and advancements. Shortly after Fleming's discovery of penicillin, streptomycin was discovered in 1944 and tetracycline in 1948, both of which were utilized in the treatment of diseases **[12], [13]**.

1.1.2. Cellular Structure of Bacteria

Bacteria are prokaryotic microorganisms. They can be found in various physical forms in nature. There are:

i. Cocci: They have a circular structure, spherical or round shape. These bacteria can multiply from a single point. For example, *Streptococcus* bacteria are examples of cocci-shaped bacteria.

ii. Bacillus: They are known for their rod or cylindrical shapes. *Bacillus anthracis* (anthrax bacteria) is a bacillus bacterium. They are usually observed in rod form.

iii. Spiril (Spirillum): They have a morphologically spiral-like shape. These types of bacteria have more than one bend and are not straight. They can be larger than other bacteria. *Treponema pallidum* (the microbe that causes syphilis) is in this group **[14]**.

iv. Vibrio: Their shape is half-moon-shaped. *Vibrio cholerae* (cholera microbe) is in this group. They often move with a single flagellum (tail that facilitates movement in liquid media).

v. Spirochete: They are similar to spiral bacteria but their coils are thinner. *Borrelia burgdorferi* (bacteria that causes Lyme disease) is a type of spirochete. Some spirochete species are pathogenic. *Treponema pallidum* is a type of spirochete that causes syphilis **[14], [15]**.

Bacterial cells consist of multiple structural layers to protect themselves fromenvironmental stress and to maintain their structural integrity. Generally, these layers are arranged from the outside to the inside as follows: glycocalyx (or its more organized form, the capsule), cell wall and the cytoplasmic membrane. The outermost component is the glycocalyx, a slippery layer composed mainly of sugars that coats the bacterial surface **[16]**. Glycocalyx covers the exterior of the cell and provides

protection against environmental threats. When it adopts a distinct, gelatinous structure, it is referred to as a capsule. While the glycocalyx represents the general structure surrounding the bacterial cell wall, capsule is a more specific, well-organized, and tightly bound form of this structure **[17]**.

Beneath the glycocalyx lies the cell wall, another critical structural component. Cell wall is a membrane layer located between the cytoplasmic membrane and the capsule **(Figure 1.1).** It surrounds bacteria from the outside, gives shape to the cell, and protects it from external effects **[18]**. Structure of the cell wall may vary depending on the bacterial species and cell type. It protects the bacterial cell from osmotic pressure. It also functions in the exchange of substances between the inside and outside of the cell.

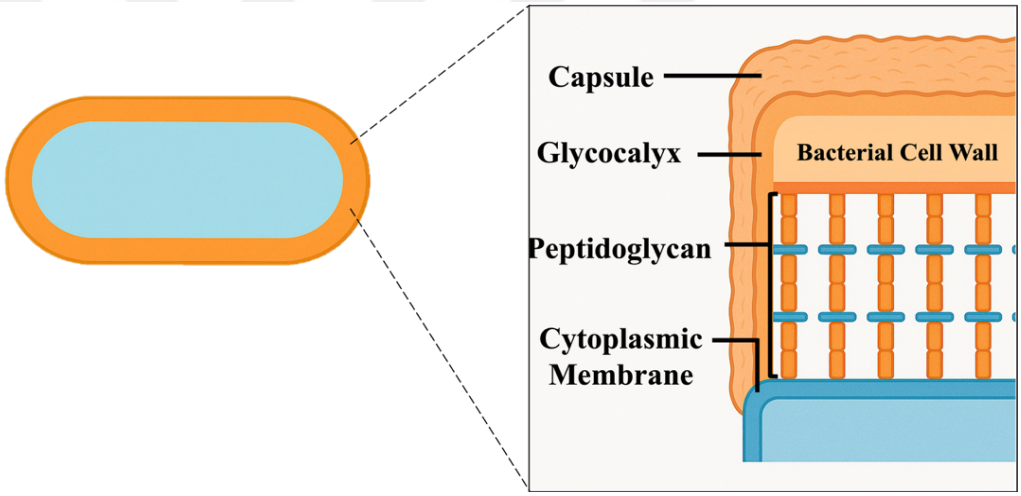


Figure 1.1: General structure of bacterial cell membrane, cell wall, peptidoglycan, capsule and glycocalyx.

Primary structural component of the cell wall is peptidoglycan (aka murein). This compound is composed of repeating disaccharide units linked by polypeptide chains. Within its structure, the monosaccharides *N*-acetylglucosamine (NAG) and *N*-acetylmuramic acid (NAM) are connected via β-1,4 glycosidic bonds to form the disaccharide backbone **(Figure 1.2) [19]**. Cross-links between peptidoglycan chains—typically formed between *L*-lysine and *D*-alanine residues—enhance the mechanical strength of the cell wall **[20]**. This structure enables bacteria to resist osmotic pressure and helps protect them against environmental threats and the effects of antibiotics **[21]**.

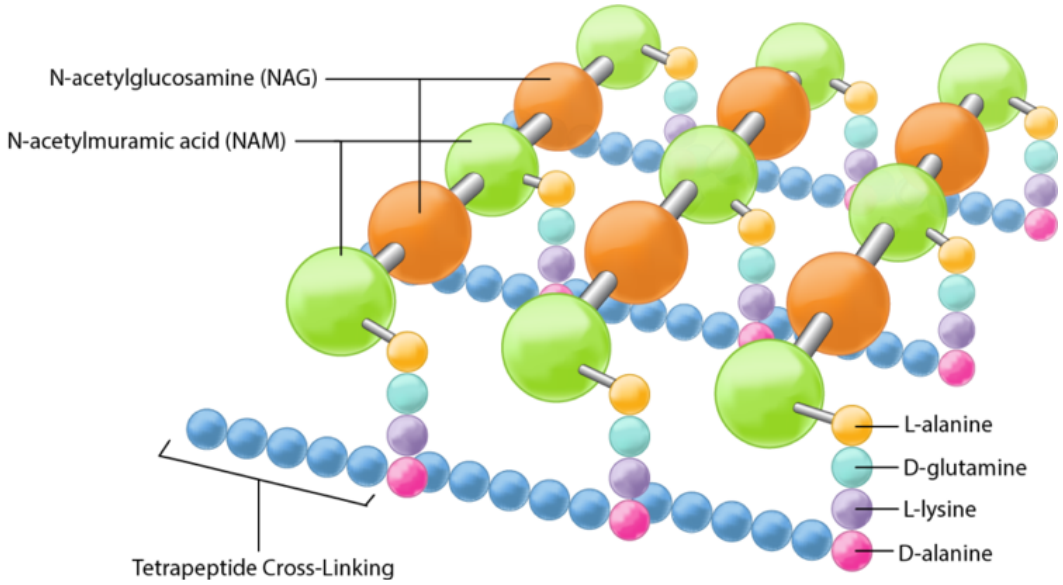


Figure 1.2: Peptidoglycan structure.

Bacteria are divided into two classes according to the thickness of the peptidoglycan layer: Gram positive and Gram negative bacteria. Gram positive bacteria have a thick peptidoglycan layer. This layer provides strength and shape to the bacterial cell. In addition, this type of bacteria is stained purple after the gram staining process. Gram-negative bacteria have a much thinner peptidoglycan layer and are pink-red after the gram staining proses **(Figure 1.3).**

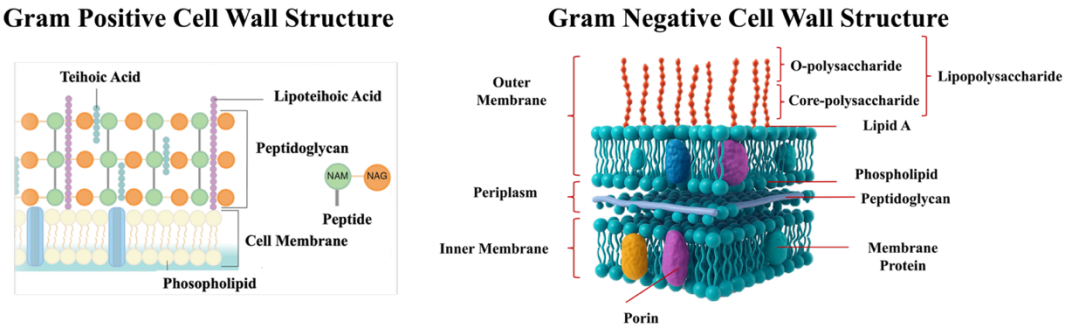


Figure 1.3: Gram positive and negative cell wall structure.

Periplasm is a space between the peptidoglycan and the cell membrane. Various enzymes and cellular components can be found in this area. This space is a transfer zone between the inside and outside of the cell. The periplasm is especially prominent in gram-negative bacteria. Periplasm space is also present in gram-positive bacteria, but this space is much smaller and not obvious.

a) Gram Positive Bacteria Cell Wall Structure: Like all bacteria, the main component of the cell wall in gram positive bacteria is peptidoglycan **(Figure 1.4)**. Gram positive bacteria have a peptidoglycan layer that can be between 30 and 100 nanometer (nm), sometimes even thicker. In contrast, the peptidoglycan thickness in gram negative bacteria is only a few nanometers. Gram positive bacteria take on a purple color after gram staining. This feature is due to the thick peptidoglycan layer that forms the cell wall. Peptidoglycan contains amino acid chains called tetrapeptides. Another compound located in the inner part of the cell wall and contributing to the structure of the cell wall is teichoic acid (TA) **[22], [23]** .There is currently ongoing debate about the existence of a periplasmic space in gram positive bacteria, as in gram negative bacteria. Studies have shown that there may be a very narrow space between the cytoplasmic membrane and the cell wall. The cell wall structure also contains a wide variety of proteins. It is known that surface proteins in Gram-positive bacteria help the bacteria to withstand harsh conditions and mediate escape from the immune system. In such bacteria, the cell wall also allows interaction with the environment, especially with the tissues of the infected host **[24]**.

b) Gram Negative Bacteria Cell Wall Structure: Gram negative bacteria have a very complex wall structure compared to gram positive bacteria **(Figure 1.4)**. Gram negative bacteria is consists of two different membranes, the inner cytoplasmic or plasma membrane and the outer membrane **[25], [26]**. Outermost layer of the cell wall is the outer membrane. It is characterized by the lipopolysaccharide (LPS) layer consisting of components such as lipid A, core oligosaccharide and O-antigen located between two phospholipid layers **[27]**. Lipid part of LPS is a type of phospholipid that forms the bacterial cell membrane. It is generally known as a lipid A compound and has toxic properties. Lipid A is recognized by the host immune system when released outside the cell and can cause a strong immune response **[28]**. Core oligosaccharide is located between lipid A and O-antigen. It helps O-antigen bind to lipid A. In addition to LPS, the outer membrane contains protein channels called porins. Outer membrane usually contains a small amount of protein structures. These channels regulate the bacterial cell's nutrient uptake

and waste release **[29]**. Bacterial outer membrane contains receptors for the attachment of bacteriophages and is involved in conjugation and cell division **[30]**. Peptidoglycan layer is located between two membranes (inner and outer membranes)in gram positive bacterias. The area between the inner and outer membranes is called the periplasmic region. Periplasm is a gelatinous substance that encloses molecules and ions in the space between the inner and outer membranes **[31]**. Periplasm helps the bacteria adapt to their environment, providing a medium for the perception and transmission of chemical signals from outside the cell. This region also mediates the transport of nutrients across the cell membrane **[32]**. Peptidoglycan layer is thinner and located between the outer membrane and the cytoplasmic membrane in gram positive bacteria.

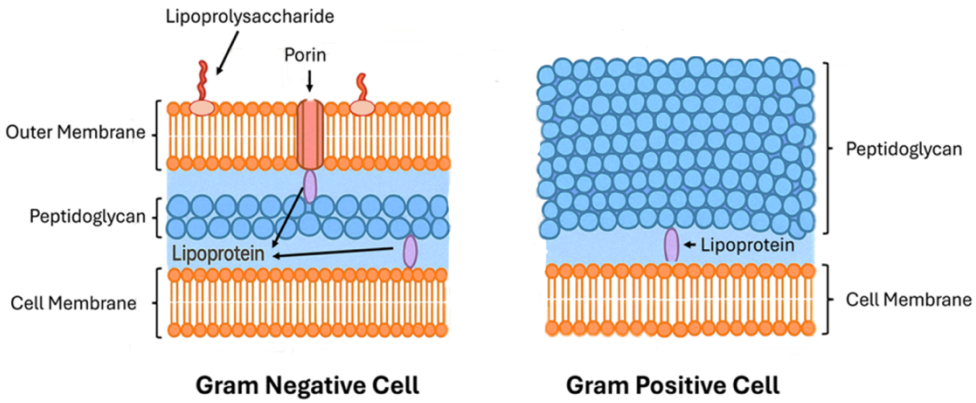


Figure 1.4: Comparison of gram positive and negative cell wall systems.

1.1.3. Pathogen Bacteria and Treatment Alternatives

Bacteria play significant roles in various fields. Nitrogen-fixing bacteria are utilized to enhance soil fertility and support plant growth in agriculture **[33], [34]**. Bacteria are also employed in the production of fermented products such as yogurt and cheese. However, some bacteria are pathogenic. For instance, bacteria like *Salmonella* and *Escherichia coli (E. coli)* can lead to foodborne illnesses, while *Mycobacterium tuberculosis* is the causative agent of tuberculosis **[35], [36]**.

Pathogenic bacteria employ various mechanisms to cause diseases. Some bacteria produce virulence factors and can adhere to host cells. For example, toxins produced by *Staphylococcus aureus (S. aureus)* suppress the immune system, facilitating the

development of infections. Certain bacteria can invade host cells and proliferate within them. Additionally, some bacterial species produce toxins that damage cells or enhance immune responses **[37]**. Example is the botulinum toxin produced by *Clostridium botulinum*, which affects the nervous system and can lead to paralysis. Bacterial infections can induce inflammation in the body, resulting in tissue damage, which exacerbates disease symptoms and disrupts bodily functions.

Treatment of bacterial diseases vary based on the type of bacteria and severity of the infection. The most well-known treatment method is the use of antibiotics. Antibiotics halt bacterial growth or kill the bacteria, thereby preventing the spread of the infection. Antibiotic therapy must be administered correctly; otherwise, there is a risk that bacteria may develop resistance to antibiotics. Some bacterial infections may also be unresponsive to antibiotic treatment.

1.1.4. Antibiotic Resistance

Antibiotics are agents utilized to inhibit the growth of bacteria. Since the early 20th century, antibiotics have offered a revolutionary solution in the fight against infectious diseases **[38]**. However, the excessive and inappropriate use of antibiotics has led to the emergence of antimicrobial resistance, making antibiotic resistance (AR) one of the most significant public health threats today. AR refers to the ability of microorganisms (particularly bacteria) to develop resistance against antibiotics. The resistance significantly complicates treatment processes.

Several factors affet the development of antibiotic resistance is influenced by various factors. One of the primary causes is the unnecessary application of antibiotics. Additionally, incorrect dosing or the premature discontinuation of antibiotic treatments in cases where such therapy is necessary also contribute to the emergence of resistance **[38]**, **[39]** .

Bacteria that have developed antibiotic resistance can spread through various means among living organisms. The resistant bacteria can rapidly spread in hospital settings due to inadequate hygiene. Developing the resistance limits treatment options and necessitates longer and more complex therapeutic approaches for infectious diseases. This situation makes it more difficult to control the spread of such diseases. Furthermore, certain resistant bacteria may even lead to outbreaks **[38]**. The condition

in which a microorganism is resistant to multiple antibiotics is referred to as multidrug resistance (MDR) **[40]** . In cases of MDR, treatment becomes even more challenging, and identifying alternative therapeutic options becomes more difficult. Bacteria exhibiting multidrug resistance can cause severe infections, especially in hospital environments. *E. coli* and *S. aureus* are examples of bacteria that may acquire multidrug resistance. Both species have the potential to develop resistance to multiple antibiotics.

1.1.5. *Escherichia coli (E. coli)*

E. coli is commonly found in the intestines and can be considered harmless. *E. coli* is 1-3 micrometer (µm) long and 0.5 µm wide, and has a thin peptidoglycan layer and outer membrane due to its gram-negative properties **(Figure 1.5)**. Strain that causes food poisoning and often causes diarrhea is known as enterotoxigenic *E. coli* (ETEC) **[41]**. Enterohemorrhagic *E. coli* (EHEC) is associated with severe diarrhea and hemolytic uremic syndrome (HUS) **[42]**. Enteropathogenic *E. coli* (EPEC) is the main cause of diarrhea epidemics in children **[43]**.

Some *E. coli* strains have posed serious health problems in the recent years, especially in developing resistance to multiple antibiotics **[44]**. Resistance to broad-spectrum beta-lactam antibiotics can be fostered, especially by strains producing Extended Spectrum Beta-Lactamases (ESBL). Carbapenem-resistant *E. coli* is one of the most resistant species and these bacteria are very difficult to treat **[45]**. In the process of developing resistance to antibiotics, *E. coli* can use active efflux pumps that prevent antibiotics from diffusing into the cell. Thus, the bacteria can avoid antibiotics. *E. coli* can transfer genes leading to resistance to others through genetic tools such as plasmids or transposons.

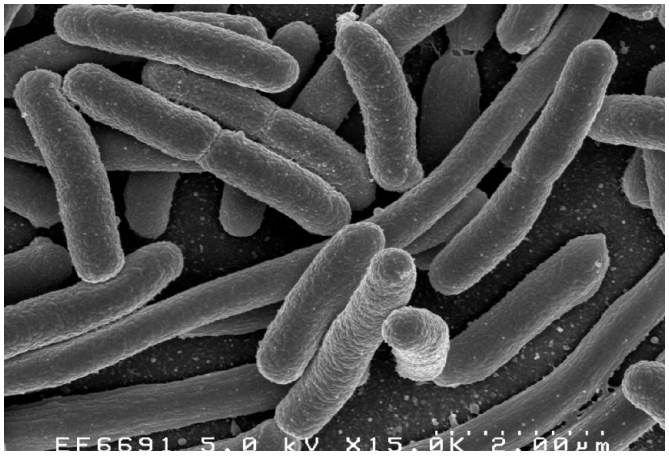


Figure 1.5: Screening Electron Microscopy (SEM) structure of *E. coli* **[46]**.

1.1.6. *Staphylococcus aureus (S. aureus*)

S. aureus is a gram-positive bacterium belonging to the genus Staphylococcus. Its morphology is spherical (coccal) **(Figure 1.6)**. *S. aureus* is a bacteria commonly found on the skin and mucosal surfaces of the nose in approximately 30% of people **[47]**. There are several factors that enhance the virulence of *S. aureus*. *S. aureus* produces enterotoxins. Enterotoxins are among the most important virulence factors and are considered the main causes of food poisoning **[47]**. *S. aureus* enterotoxins are heat-stable exotoxins. They are one of the most common causes of food poisoning. There are more than 20 types (SEA, SEB, SEC1-3, SED, SEE, etc.). They exhibit superantigen properties and nonspecifically activate numerous T-cells, leading to the release of large amounts of cytokines.

Toxic shock syndrome toxin-1 (TSST-1), produced by certain *S. aureus* strains, functions as a potent superantigen. TSST-1 can overstimulate the immune system, leading to severe systemic infections **[48]**. *S. aureus* also produces various enzymes that facilitate the spread and transmission of infection. Among these, hyaluronidase and lipase are particularly significant. Hyaluronidase enhances the bacterium's ability to penetrate tissues, while lipase degrades lipids and contributes to the dissemination of the infection to surrounding tissues **[48]**. With these features, *S. aureus* is recognized as a major pathogen responsible for a wide range of diseases, from skin infections to life-threatening systemic conditions **[49]** .

Antibiotic resistance is one of the primary factors that further increases the clinical significance of *S. aureus*. The bacteria can develop resistance to methicillin, penicillin, and many other antibiotics. In particular, methicillin-resistant *S. aureus* (MRSA) strains are major causes of hospital-acquired infections. MRSA strains have also developed resistance to several other antibiotics, making them more difficult to treat **[50]**. MRSA carries the mecA gene, which confers resistance to methicillin by enabling the bacterium to inactivate antibiotics. Moreover, *S. aureus* can rapidly spread antibiotic resistance genes through horizontal gene transfer. Furthermore, the emergence of strains resistant to last-resort antibiotics such as vancomycin has made the situation even more complex. Vancomycin-resistant *S. aureus* (VRSA) isolates have now been reported **[51]**.

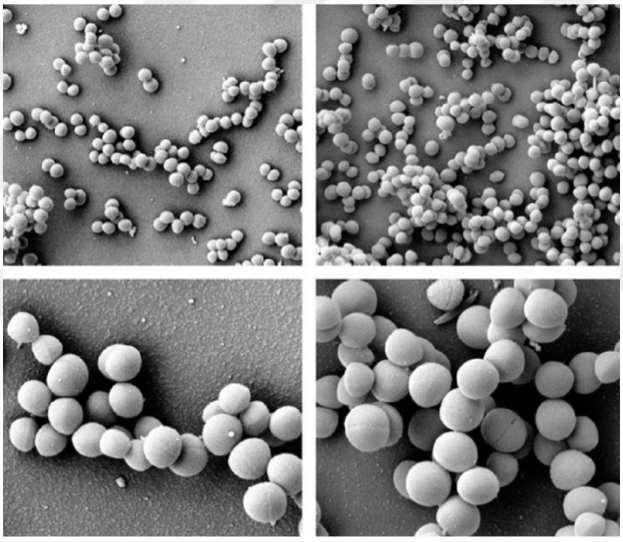


Figure 1.6: Transmission Electron Microscopy (TEM) structure of *S.aureus* **[52]**.

1.1.7 Alternative Treatment

There are many different areas of study and research to counteract antibiotic resistance and develop alternative treatment strategies. One of the most classic ways to overcome antibiotic resistance is to discover new antibiotics. However, this process is quite long, expensive and difficult. Antibiotic research and development programs continue today to treat more resistant bacteria. Nanotechnology develops new ways to treat bacterial diseases. Novel antimicrobial nanoparticles can target bacteria and effectively destroy the. This type of treatment can provide an alternative approach to resistant bacteria

[53]. Today, utilization og antimicrobial peptides for infectious disease treatment is emerging treatment approach. These peptides are natural defense molecules that are effective against various microorganisms. There are various studies on the therapeutic effect of antimicrobial peptides against resistant bacteria. Studies show that these peptides can kill bacteria by damaging their cell walls **[54]**, **[55]**.

Various treatment strategies are being developed to treat bacterial infectious diseases. CRISPR technology is one of the most important methods used in this field. This method and similar genetic engineering techniques can target bacterial DNA to disable resistance genes **[56]**. Molecular therapies can alter the genetic factors that cause bacteria to become resistant, thus restoring the effectiveness of antibiotics. Additionally, antibiotic therapy is widely used to treat resistant bacteria **[57]**.

1.2. Bacteriophages

1.2.1 General Structure and Infection Mechanism

Another alternative treatment strategy to antibiotic therapy is bacteriophage-based therapies. Bacteriophages are viruses that target and kill bacteria. Bacteriophages are simple bacterial parasites.

Phages generally consist of a head that contains the genome (DNA or RNA) followed by a tail. Known phages are generally examined under thirteen families according to their morphology, nucleic acid type, envelope or lipid presence. Although bacteriophages differ morphologically, most of them are lytic phages that carry doublestranded DNA (dsDNA) genome in their head section. The tail section ensures that the phage genome is transferred to the target by attaching to the receptors located on the cell membrane of the targeted bacteria. Phages are divided into three families morphologically; i) Myoviridae, with a long and shortenable tail structure; ii) Siphoviridae, with a long, flexible and non-shortenable tail structure; iii) Podoviridae with a short and non-shortenable tail **[58], [59], [60]**. Two bacterophages that will be exploited in the thesis study, Mycobacteriophage D29 (PhageD29), and Bacteriophage K (PhageK) belong to the Siphoviridae family and Myoviridae family, respectively **[58], [59], [60]** .Phages use two different mechanisms to infect bacteria: the lytic and lysogenic cycles. Lysogenic cycle involves a process in which the phage genome is

transferred to the host cell and integrated into the target bacterial DNA. Here, genome undergoes replication with bacterial DNA during division of host, allowing it to be transferred to new bacterial cells **[61]**. Lytic cycle involves a four-step life cycle of adsorption, penetration, biosynthesis, and lysis **[62] (Figure 1.7)**. First, phage binds to receptors on the host cell membrane, which transfers the phage genome to the bacteria. Replication and protein synthesis occur in bacterial cytoplasm. Therefore, new phage particles are produced in bacteria. After bacteriophage genome is transferred to bacterial cytoplasm and expressed there, endolysin enzymes and holin proteins are produced, which will break down peptidoglycan layer of the host cell and thus allow release of new phages to the environment **[63]**.

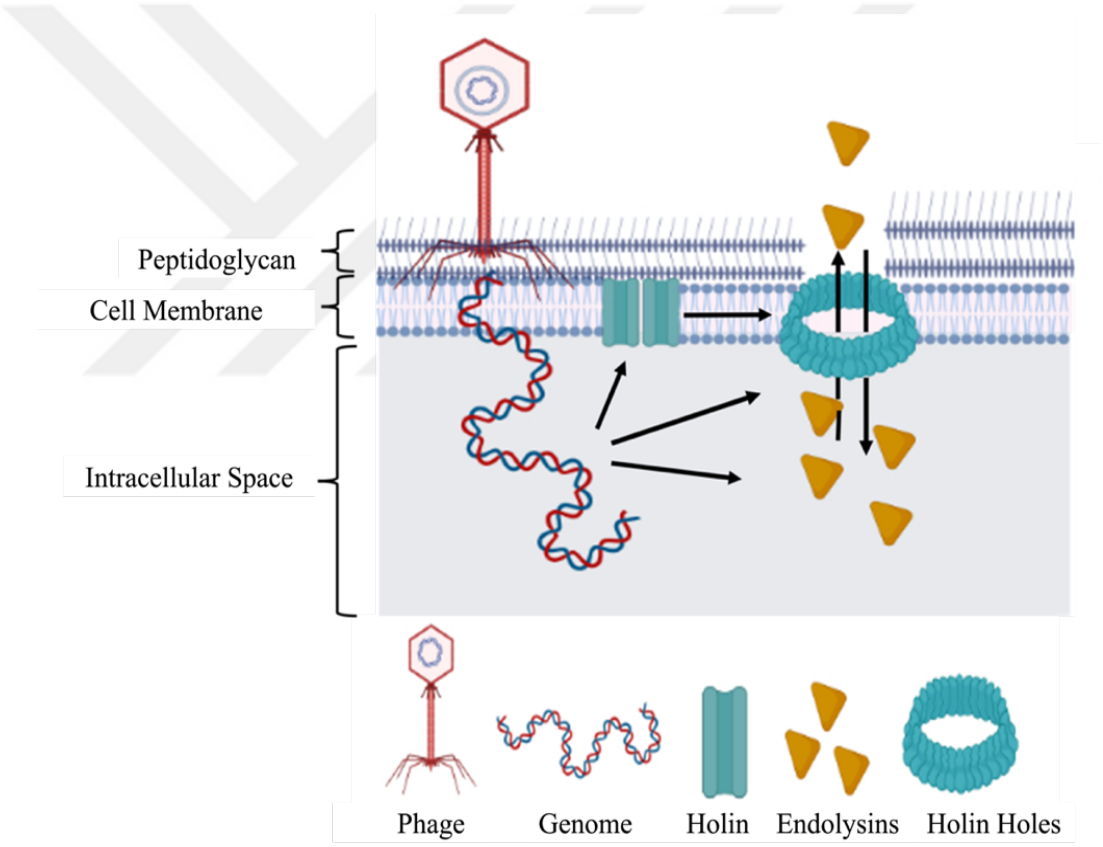


Figure 1.7: Phage infection strategy on gram positive bacterial cell.

Endolysin is a type of enzyme that can hydrolyze peptidoglycan bonds. For endolysins to exert their lytic effects, they must pass through the bacterial inner membrane **[63]**. Holins are small hydrophobic cell membrane proteins that are encoded by the host genome after the phage infects the host. Holin proteins are classified based on the number of transmembrane domains (TMDs). According to this classification, the holin

proteins of PhageK and PhageD29 belong to the class II holin group **[64], [65]**. Holins accumulate in the cell membrane to allow endolysins to reach the cell wall and accelerate lysis, causing formation of holes **[66], [67]**. When holins reach the appropriate concentration in the bacterial inner membrane, they create holes on the membrane surface, making the membrane permeable to endolysins. In this sense, they control the access of endolysins to the cell wall. Holin proteins and endolysin-encoding genes have been identified in different groups of gram-positive and gram-negative bacteria infected by various phages.

1.2.2. Phage Based Infection Treatment Strategies

First fundamental step in the history of phage therapy was taken by the British bacteriologist Ernest Hanbury Hankin in 1896. Hankin showed that cholera-causing bacteria obtained from the Ganges and Yamuna rivers in India were destroyed by a biological entity **[68]**. In 1917, Felix d'He'relle introduced the term 'bacteriophage', from the Greek word 'phage', meaning 'bacteria eater'. In the same year, phage therapy was first used to treat chickens infected with *Salmonella gallinarum*. Institute of Bacteriophage Microbiology and Virology (IBMV) was founded in Tbilisi by D'Hérelle and Georgi Eliava in 1933. Subsequently, large quantities of bacteriophages were produced and used during World War II **[69]**.

In a clinical trial conducted in the 1950s and 1960s, 607 patients who did not respond to antibiotic therapy were treated with bacteriophage therapy, and 80% were reported to have recovered. In the 2000s, human trials of phages began **[70]**. Despite the successful and positive results of phage therapy, the nature of phages has always been controversia **[71], [72]**. Bacteriophage-based therapies are still available today in some Eastern European countries (Georgia, Russia, Poland) as conventional or prescription products. For example, six standard phage preparations from the Eliava Institute are commercially available.No phage therapies have been approved by the FDA in the USA. However, limited trials are underway through compassionate use or single patient access. Phage therapies faded from favor in the West in the 1940s and onward with the discovery of antibiotics, but their routine use continues in Eastern Europe.

Currently, many clinical trials (phases 1, 2, and 3) are ongoing, with phage cocktails being tested against various infections in the United States and Europe. Companies

such as Locus Biosciences have developed CRISPR-enabled phage therapies for diseases such as urinary tract infections and have advanced to phase 2 trials. Several commercial phage-based products were available in the mid-20th century. However, they were withdrawn from the market during the same period due to the rapid development, ease of use, and broad efficacy of antibiotics.

Phage therapy allows bacteriophages to target bacteria to treat infections. This method can be effective against bacteria that have developed resistance to antibiotics. Phages can be more effective than antibiotics in several situations. Bacteria can form biofilms, complicating their life cycle. Bacteriophages can penetrate biofilms better than antibiotics. They can reach bacteria by passing through biofilm layers thanks to their exopolysaccharide-degrading enzymes **[73]**. Bacteriophages target only specific bacteria, reducing the risk of harming healthy cells. In contrast, antibiotics can damage healthy tissue along with the bacteria **[74]**.

Bacteriophages work specifically for bacteria. This prevents the development of side effects when used in treatment. The risk of secondary infection is also reduced. Bacteriophages only multiply of infection. They destroy microorganisms within the boundaries of this area. At the side of antibiotic treatment, the drug enters the circulation and spreads, which can cause the effect of the drug to be felt less in the infected area **[75]**.

Antibiotic treatment can lead to various allergic reactions and infections. No side effects have been recorded during or after bacteriophage-based treatments. Bacterial resistance to bacteriophage is possible. However, in this case, the bacteriophage can also mutate and thus stand against resistant bacteria.

1.2.3. Computer-Aided Phage Therapy Strategies

Computer-based techniques are becoming increasingly widespread to examine bacteriophage-bacteria interactions more closely. Various studies have been conducted in the literature to increase the effectiveness of phage therapy and to develop new treatment strategies. Molecular Dynamics (MD) simulations were used in a study on the dynamics of the Holin S105 protein and its dimerization in the cell membrane **[76]**. Dynamics of Holin S105 in the cell membrane were examined in detail. Different mathematical modeling methods have been designed to improve bacteriophage

production processes. In one study, a two-stage phage production process was modeled. The effects of the parameters used in the modeling process on phage production efficiency were evaluated **[77]**.

As a result, it was revealed that mathematical models are an important tool in terms of optimizing phage production processes. Computer program called "Cocktail" was designed to model the kinetic effects of bacteriophage-induced diseases. It is used to simulate the effects of phages on bacteria. Cocktail allows predicting how phage therapy may develop under different conditions **[78]**.

Today, computer-based techniques are widely used in the development and optimization of phage treatment strategies. Molecular dynamics simulations, mathematical modeling and special software contribute to a better understanding of phages.

2. AIM OF STUDY

The aim of this thesis is to understand the behavior of holin proteins—key components in the bacteriophage-induced bacterial lysis mechanism—within the cell membranes of both Gram-positive and Gram-negative bacteria. In this context, computational approaches and MD simulations were employed to investigate the clustering patterns of holin proteins on the membrane and to evaluate their membrane-disruptive potential.

In the first phase of the study, the holin protein derived from HolPhage-D29, whose experimental effects have been extensively reported in the literature, was selected. The lytic capacity of HolPhage-D29 has been demonstrated in both in vitro and in vivo systems, and its activity against *E. coli* has been supported by several studies **[79], [80]**. Accordingly, the initial analyses focused on assessing the effects of HolFaj-D29 on the *E. coli* membrane. Structural impacts of different homo-oligomeric states (such as homo-dimers and homo-tetramers) were evaluated. This phase of the thesis serves as a positive control, aiming to determine the pore-forming capacity and functional roles of various HolPhage-D29 oligomers on the membrane structure.

In the second phase of the study, focus shifted to *Staphylococcus aureus* (*S.aureus*) (Gram-positive bacteria), which exhibits antibiotic resistance levels comparable to *E. coli*. The effects of a holin protein derived from phage K - HolPhage-K - on the *S. aureus* membrane model were investigated. Phage K is known to naturally infect *S. aureus* **[81]**. However, there is currently no direct evidence in the literature confirming the lytic efficacy of HolPhage-K specifically on *S. aureus*. Therefore, this part of the study aims to determine whether HolPhage-K alone can exert a disruptive effect on the *S. aureus* inner cell membrane. Additionally, by modeling various oligomeric states of HolPhage-K, its potential as an antimicrobial peptide or therapeutic agent was also evaluated.

According to the literature, the C-terminal domains of holin proteins are reported to play critical roles in membrane interaction, regulation of lysis timing, and structural organization **[82]**. Based on this information, the analyses in this study also aim to evaluate the potential interactions of the C-terminal domain with the cell membrane

and its effects on membrane deformation. The overall workflow of the thesis is illustrated in **Figure 2.1**.

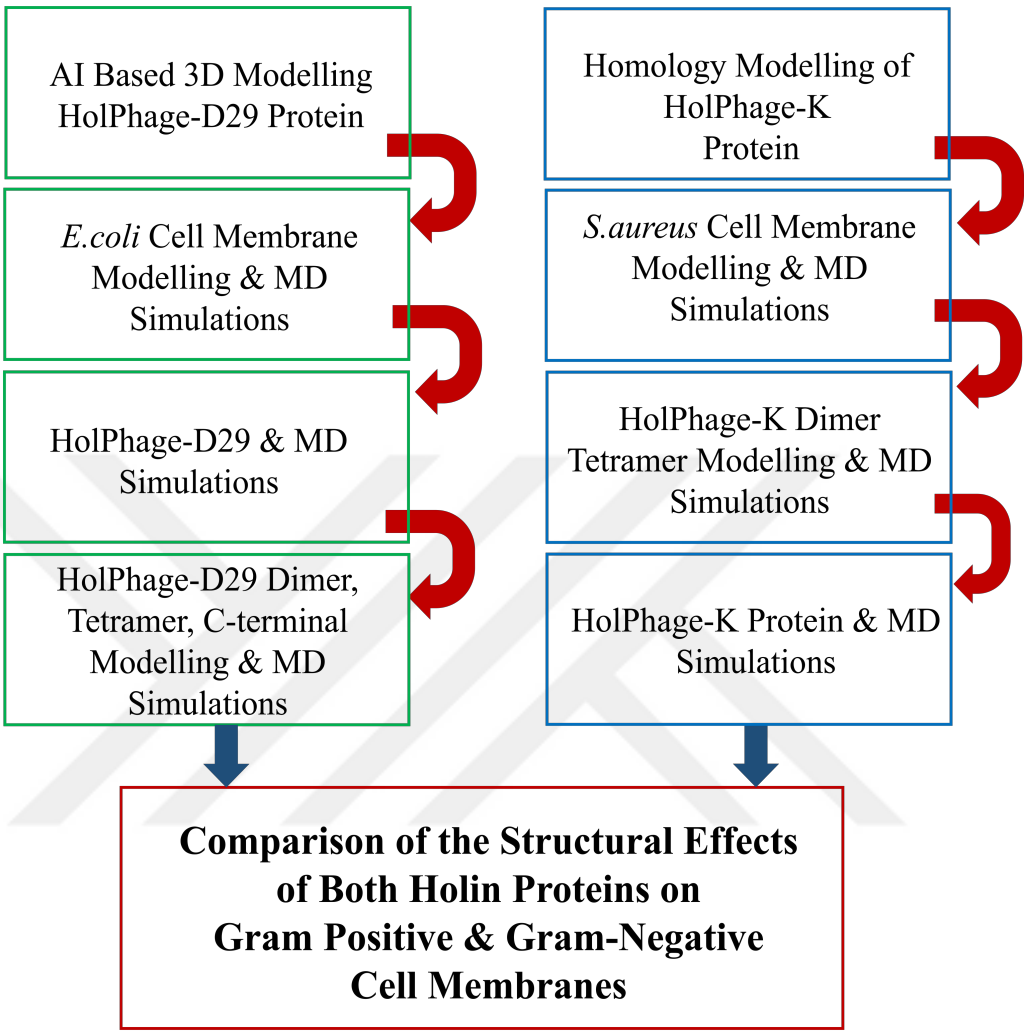


Figure 2.1. Workflow of this thesis study.

3. METHODS

Understanding the mechanisms of holin proteins in cell membrane disruption is critically important for developing effective therapeutic applications against antibiotic resistance in bacteriophages. The functioning of these proteins allows for the development of targeted treatment strategies. This thesis, which provides a detailed analysis of the effects on cell membranes, will contribute to a better understanding of the structural and functional properties of holins.

3.1. Holin Structure Prediction

Holin protein associated with Bacteriophage D29, identified in National Center for Biotechnology Information (NCBI) AAC18451.1 holin [Mycobacterium phage D29], consists of 141 amino acids (NCBI) **[83]**. The amino acid sequence of the holin protein associated with Bacteriophage K, identified in NCBI protein database YP_009041295.1holin [Staphylococcus phage K holin], consists of 167 amino acids (NCBI) **[84]**.The three-dimensional structure of the holin proteins was modeled from the obtained amino acid sequence utilizing protein structure prediction techniques **[85], [86]**.

3.1.1. Theory of Protein Structure Prediction

Protein structure prediction is the process of determining the three dimensional (3D) conformation of a protein. This process is a critical area of research within the field of molecular biology and bioinformatics. The accurate determination of protein structures is essential for understanding their functions and interactions in biological systems. There are two types of prediction methods of protein structures: experimental and computational methods **[87]**.

3.1.1.1. Experimental Methods

Different experimental methods exist to obtain the 3D structure of macromolecules. The methods used for this purpose are as follows; Nuclear Magnetic Resonance

(NMR) analysis, X-ray diffraction and electron microscopy. X-ray diffraction is a method that uses the resulting spread and dispersion of X-rays as they pass through a crystal. This method is widely used to study molecular structures. The process of sample preparation for X-ray diffraction is quite challenging, and many cell membrane proteins cannot be crystallized by this method. In addition, this method may cause radiation damage to the sample being examined, and the resulting data resolution may be limited **[88]**, **[89]**.

NMR is a spectroscopy method based on the principle of changing the energy levels of atomic nuclei in a magnetic field. NMR is often utilized to study molecular structures, dynamics, and interactions. In order to obtain a three-dimensional structure by NMR analysis, samples must be well selected. Typically, proteins larger than 25 kilodalton (kDa) are not suitable for NMR analysis. Such constraints have necessitated the development of a novel approach for predicting the 3D structure of proteins **[90]**, **[91]**. Electron microscopy, particularly cryo-EM, has emerged as a revolutionary technique for visualizing large protein complexes and assemblies. Cryo-EM is advantageous for studying large macromolecular complexes, but it generally provides lower resolution compared to X-ray crystallography **[92]** .

3.1.1.2 Computational Methods

Computational methods for protein structure prediction involve various approaches and algorithms to determine the 3D structure of proteins from their amino acid sequences. Computational methods for protein structure prediction encompass several key approaches that leverage different principles and technologies. These include homology modeling, artificial intelligances (AI) based methods, threading, machine learning approaches. Each method has its unique strengths and is often used in combination to enhance prediction accuracy and reliability. 3D structures of HolPhage-K and HolPhage-D29 proteins were modeled using the classical homology modeling method with the artificial intelligence-based AlphaFold protein structure prediction system in the presented thesis study. Technical details regarding these approaches are presented below:

i. AlphaFold is an artificial intelligence system and is one of the important tools preferred today for predicting the 3D structure of proteins **[83]**, **[93]**. AlphaFold

analyzes protein sequences and predicts the 3D structures of these sequences using deep learning techniques **(Figure 3.1)**. AlphaFold is a highly advanced artificial intelligence model developed by DeepMind, designed to model the three-dimensional structures of proteins using amino acid sequences **[94]**, **[95]**. It employs a transformer-based architecture, enabling it to effectively model the folding processes and structural characteristics of proteins **[96]**. AI model utilized by AlphaFold exhibits exceptional performance in predicting the natural structures of proteins. One of its remarkable achievements includes winning the Critical Assessment of protein Structure Prediction competition (CASP14) **[96]** , recognized as one of the most prestigious contests in the field of protein structure prediction globally.

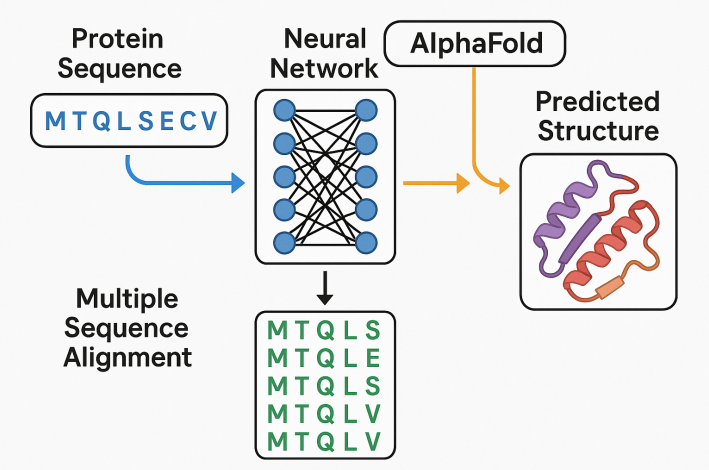


Figure 3.1: Basic working prenciple of Alpha Fold

ii. Homology modeling is a method used in the fields of bioinformatics and structural biology. The aim of the method is to predict the three-dimensional structure of a protein in the most accurate way based on the amino acid sequence of protein. The resulting structure must be correct enough to be comparable to experimentally discovered results. The homology modeling process can be summarized in seven steps **[97] (Figure 3.2)**:

   a. Template Identification: Each protein has a unique amino acid sequence. The first step in the homology modeling technique is to define the existing sequence (template). Subsequently, the sequence of

a homologous protein exhibiting high similarity to the existing template is identified and the initial alignment is performed.

b. Correction of Alignment: After detecting protein structures that are like the target sequence, different methods are applied to achieve a better alignment using these templates.

c. Backbone Generation: Alignment of the target protein sequence with homologous proteins with similar properties is completed. Once the sequence alignment step is completed, the process moves on to the construction of the 3D model. For this purpose, first protein backbone must be created based on the atomic coordinates of previously aligned templates.

d. Loop Modeling: Gaps are found in the alignment between the designed protein structure and the template. These gaps occur in the form of deletions on the model or additions on the template. Deletions create holes in the creation of the 3D structure, while additions in the template lead to conformational changes. These changes generally arise in loops and are difficult to detect. At this stage, two different approaches, Knowledge-Based Method **[98]** and Energy Based Method **[99]**, **[100]** are applied to model the loops.

e. Sidechain Modeling: In proteins with similar structures, the side-chain conformations of conserved residues (rotamers) typically exhibit similar $\chi 1$ angles (the torsion angle around the Cα-Cβ bond). This allows for direct transfer from the template to the model when sequence similarity is high (≥35%). Techniques for side-chain modelling include the use of rotamer libraries derived from highly-resolution structures and energy-based structure alignment and scoring.

f. Model Optimization: Model optimization is a critical process for validation of sidechain rotamers. An iterative approach can be followed in model optimization. First side chain rotamers are estimated and the shifts in query backbone are calculated. Rotamers are re-estimated for new backbone structure and energy minimized. Energy minimization is a technique used to ensure that protein structures reach their lowest

energy level. This process is critical for improving the stability of protein structures and eliminating errors **[101]**.

g. Model Validation: There are two basic methods for evaluating the accuracy of the model formed because of the modeling process. First one is forcefield-based energy calculation that utilizes MD simulations. The caveat of this method of that protein may have misfolded but still may provide low energy. Thus, the correct folding state must be checked. Second method determination of normality indices. Examples: General checks for bond lengths and angles **[102]**. The internal/external distributions of polar and nonpolar residues can be used to detect completely misfolded patterns **[103]**.

Homology modeling is a powerful method for predicting protein structures, but its accuracy and reliability depend on the similarity between the template and the target. It provides accuracy comparable to crystal structures with high sequence chemistry similarity (>90%). However, in the case of low queue chemical similarity (<50%), large errors can occur. It offers a faster and more cost-effective alternative to experimental methods **[104]**.

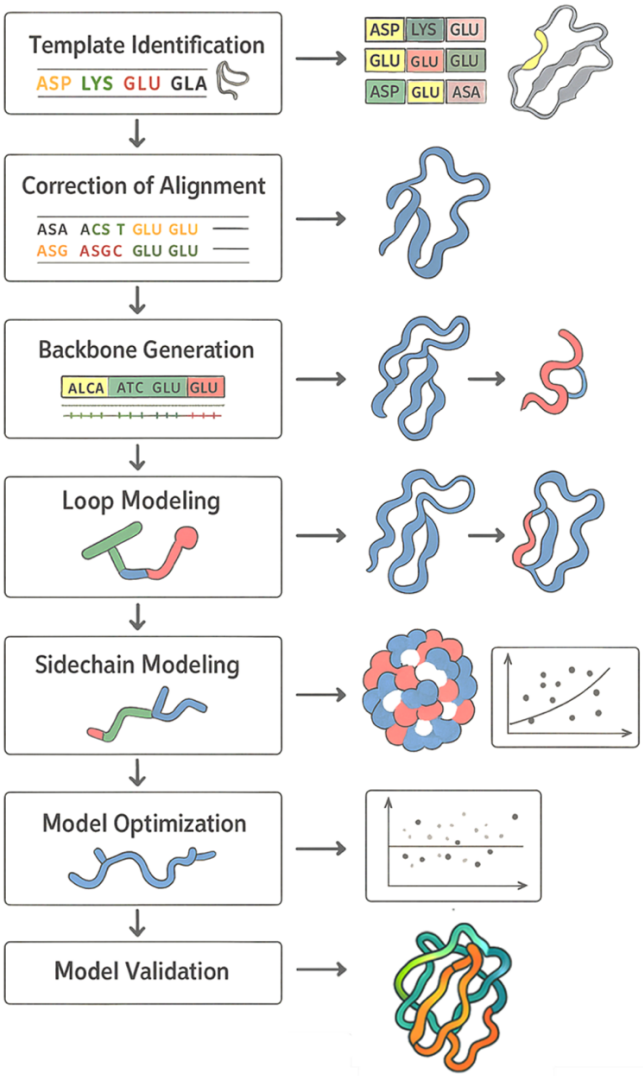


Figure 3.2: Steps of Homology Modelling technique.

3.1.2. HolPhage-D29 Structure Prediction with AI Based Approaches: AlphaFold

HolPhage-D29 was modeled in 3D by machine learning approaches using the Alphafold server. HolPhage-D29 consists of two TMDs and a highly hydrophobic intracellular tail extending from the C-terminus. C-terminal domain was observed to fold alongside TMDs in 3D structure prediction attempts using AlphaFold. This is likely due to AlphaFold's inherent tendency to generate compact structures. Additionally, hydrophobic regions are often interpreted by AlphaFold as membrane-embedded. Therefore, when the full-length protein sequence was submitted to AlphaFold, an incorrect structure was predicted. TMDs and C-terminal region were

modeled separately to prevent this misfolding. Similar methodologies have been reported in the literature **[105]**. In one study, it was shown that highly hydrophobic but non-membrane-embedded protein regions were mispredicted by AlphaFold, and these protein segments were modeled independently to overcome this issue **[106], [107]**.

Amino acid sequence of the protein was obtained from the NCBI database in the modeling process of HolPhage-D29. Initially, the amino acid sequence containing the transmembrane domain of the protein (residues 1-69) was modeled using AlphaFold. Subsequently, the modeling process for the C-terminal domain of the protein, which extends into the intracellular area (residues 70-141), was carried out. Those with the highest accuracy scores were preferred for the protein domains among the protein models obtained from AlphaFold. This stage is a critical step to enhance the biological functionality and stability of the model.

The modeled transmembrane domain and C-terminal domain were combined using the YASARA Structure program **[108]**. During this process, the integration of the structures was ensured by considering the residue angles and bonds. Finally, energy minimization was applied to the model. This step is essential to increase the stability of the model and maintain its structural integrity.

3.1.3. HolPhage-K Structure Prediction with Homology Modelling

The open reading frame (ORF) region of the holin protein from Bacteriophage-K has been found to have a gene sequence of >YP_009041295.1 holin [Staphylococcus virus K], consisting of 504 base pairs (bp) (NCBI) **[83], [109]**. 167-amino-acid sequence of HolPhage-K was modeled using a hybrid modeling approach. Initially, the segment corresponding to residues 24–167 was modeled using homology modeling via the SWISS-MODEL platform **[110]**. During this process, the crystal structure of the light-driven chloride pump ClR (Protein Data Base (PDB) ID: 5FJG) was used as a structural template **[111]**.

N-terminal region, comprising the first 24 amino acids (Met1–Thr24), was also modeled using SWISS-MODEL by referencing the cryo-EM structure of the photosynthetic alternative complex from *Roseiflexus castenholzii* (PDB ID: 6LOD)

[112]. The modeled N-terminal fragment was then joined to the previously constructed 24–167 segment using the YASARA Structure software **[108]**.

According to the literature, it is a valid and commonly applied strategy to use different tools for modeling N- or C-terminal segments—particularly in proteins where full-length structural templates are lacking or where disordered regions are present **[113]**. In this context, the implemented hybrid modeling approach ensures structural accuracy and facilitates the construction of a complete three-dimensional protein model.

3.2. Molecular Dynamics Simulations

3.2.1. Theory of Molecular Dynamics Simulations

MD simulations is a type of computerized simulation technique developed to study the physical motions and interactions of atoms and molecules. MD simulations offer insights into the temporal evolution of macromolecular conformations, as well as their kinetic and thermodynamic properties. Simulations offer the chance to examine the individual motions of all atoms in a specific time interval, at the atomic scale. The kinetic behavior and thermodynamic properties of atoms and molecules can be studied using MD simulations, thus obtaining results comparable to biological data **[114]**.

The idea of MD was first proposed in the 1950s by Pasta, Fermi, Tsingou and Ulam **[115]**. The first MD simulation was carried out by Wainwright and Alder in 1957 using the rigid sphere model. In this model, atoms could only interact in perfectly elastic collisions **[116]**. In 1964, Rahman performed an MD simulation in which interactions between atoms were modeled using the Lennard-Jones potential. With this work carried out by Rahman, the dynamical properties of the liquid argon system were examined and the technical power of molecular dynamics simulations was revealed **[117]**. With the advances in computer systems in the 1970s, there were new developments in MD. In 1970, a new MD algorithm was designed by Berendsen et al. This algorithm used a new method to control the temperature of the system **[118]**. In 1976, the first protein MD simulations were carried out by Karplus et al **[119]**. This work is considered an important milestone in terms of MD simulations into biomolecules. After 1980s, various programs such as NAMD, GROMACS, Chemistry at Harvard Macromolecular Mechanics (CHARMM) were developed and MD

simulations became very easy to apply, **[120]**, **[121]**, **[122]**. New algorithms and software have improved the accuracy and efficiency of simulations. Today, it is widely used in many fields such as molecular dynamics, materials science, molecular biology, and drug design.

MD simulations are based on classical Newtonian mechanics. Newton's second law of motion ("the acceleration of any body is inversely proportional to its mass, directly proportional to the net force acting on it (F = m * a) forms the basis of MD simulations. According to the simulation model:

I. the force on each atom simulations (classical MD using all-atom force fields)
II. force on certain coarse spheres (Coarse-Grained MD simulations),
III. the potential energies and energy changes of the molecules can be calculated **[123]**.

In MD simulations, potential energy calculations are performed using force fields **[124]**. The force field describes the potential energy of a system. It represents various atomic interactions and bonds. These interactions can be listed as follows:

a) Define the covalent bond energies between atoms.
b) Focuses on bond angles (between three atoms). Calculates angle energy. This calculation is important in terms of the stability of the bond angles.
c) Defines dihedral energy (The angle between four atoms is called the dihedral angle). This angle influences the conformation of the molecule.
d) Identify nonbonded interactions. It describes the Coulombic (electrical) and Lennard-Jones (van der Waals) interactions between non-bonding atoms.

$$E = \sum_{i} \sum_{j \neq i} \left[\frac{q_i q_j}{4\pi\varepsilon_0 r_{ij}} - \frac{A_{ij}}{r_{ij}^{12}} + \frac{B_{ij}}{r_{ij}^{6}} \right] \tag{3.1}$$

In MD, important to identify and calculate various interactions to make accurate calculations. These interactions are two types:

a) Short Range Interactions: Defines the forces that are effective at short distance. such as van der Waals interactions and bond forces.
    i. Van der Waals Interactions: Mostly calculated with the Lennard-Jones potential. **[125], [126].** Its formula ($V(r)$: Potential energy, ε: Depth

(strength of gravitational force), σ: Characteristic size of atoms, r: Distance between atoms) is as follows:

$$V(r) = 4\,\varepsilon \left[\left(\frac{\sigma}{r}\right)^{12} - \left(\frac{\sigma}{r}\right)^{6}\right] \tag{3.2}$$

ii. Harmonic Potential: Bond forces (covalent bonding) are often calculated with harmonic potential (k: Bond constant (stiffness of the bond), r: Distance between atoms, r 0: Balance distance) in MD simulations **[127]**:

$$V(r) = \frac{1}{2} k_b (r - r_0)^2 \tag{3.3}$$

b) Long Range Interactions: These forces are effective over long distances. Such as electrostatic forces of attraction and repulsion. Electrostatic Interactions: It is calculated by Coulomb's Law. It is used to describe electrostatic interactions between charged particles (*F is* the force, *k* is the Coulomb constant, *q1* and *q2* are charges, *and r* is the distance between charges). Coulomb's law is especially important for modeling hydrogen bonds and all electrostatic interactions between water molecules **[128]**.

$$F = \frac{1}{4\pi\varepsilon_0} \cdot \frac{q_1 q_2}{r^2} \tag{3.4}$$

ii. Ewald Sum Method: It is one of the classical methods used to calculate long-range electrostatic interactions. It uses a two-step approach:

iii. Particle-Mesh Ewald (PME) Method: It is a derivative of the Ewald method. It is often more efficient in large systems. The electrostatic potential is represented on a grid. The charges of the molecules are distributed across these grid points **[129]**.

2. In the simulations, all interactions between molecules are calculated in accordance with their "cut-off" radii. The maximum distance at which an atom or molecule acts is called the "cut-off radius". This term determines the

maximum distance at which an atom or molecule is effective. Interactions beyond this distance are ignored. In this way, the computational load is reduced, and the simulation speed is increased **[130]**.

In MD simulations, the time-dependent changes of molecules are modeled. Therefore, atomic energies and velocities are calculated dynamically. Weak intermolecular interactions cannot be calculated in classical molecular mechanical (MM) approaches. For this reason, weak interactions are often ignored or limited to the inclusion of additional parameters in the simulations.

MD simulations use different algorithmic optimizations to make the calculations in the simulation more stable and efficient. The algorithms that are usually preferred are known as SHAKE, Linear Constraint Solver (LINCS), and RATTLE.

The SHAKE is an algorithm developed to keep bond lengths constant at a certain value. It is preferred to control the bond lengths of light atoms such as hydrogen atoms in MD. The SHAKE algorithm ensures that the dynamics of the system are maintained **[131]**.

The RATTLE algorithm is often used to keep angular bonds constant. This algorithm is expressed as an extension of the SHAKE algorithm. It is used for fixing interatomic bond lengths as well as controlling angles. The RATTLE algorithm is designed to be used in MD simulations applied to complex structures to increase simulation stability **[132]**.

LINCS algorithm, similar to the RATTLE Algorithm, is used as an effective method to solve constraints by keeping bond lengths and angles constant during simulation. The LINCS algorithm is mostly preferred for maintaining the dynamics of large systems. By using a fast analysis method, it requires less computational power to solve constraints **[133]**.

3. MD simulations can be designed to proper varying experimental conditions. During the simulation, periodic boundary conditions are applied (PBC). PBC assumes that an infinite system has been created. Around a central cubic box, this box is copied repeatedly. Thus, all atoms involved in the simulation are surrounded by neighboring atoms. Like so, the features of the system are intended closer to reality. PBC isn't just limited to cubic boxes. Rhombus,

dodecahedron and octahedron geometric shapes can also be utilized **[134]**, **[135], [136]** .

In the MD simulation, the mathematical expressions required to calculate the potential energy of the system are located in the force field. There are distinct force fields for various biomolecules (proteins, DNA, lipids). The force fields used in MD simulations are grouped according to two different approaches. Each type of force field provides different levels of atomic detail to simulate the interactions of molecules **[137]**.

I. All-Atom Force Fields: Each atom is represented individually in such force fields. These allow detailed study of the individual dynamics of each atom. For each atom in the system, separate parameters of charge, potential energy and interaction are used. CHARMM, Assisted Model Building with Energy Refinement (AMBER) Optimized Potentials for Liquid Simulations (OPLS) are all-atom force field types **[138]**, **[139]**, **[140]**, **[141]**.

II. United-Atom Force Field: Some atoms are grouped and represented as such in these force fields. Generally, hydrogen atoms are combined, and only the main atoms (for example, carbon or oxygen) are considered. This reduces the number of atoms and decreases the computational burden. It provides faster results from simulations to be applied to large systems **[142]**. Groningen Molecular Simulation (GROMOS) is a type of united-atom force field. In this force field, hydrogen atoms are combined with carbon atoms. MARTINI **[143]** is a united-atom force field in which molecules are modeled as larger particles.

An important notion in balancing of molecules in MD is the concept of "ensemble". The combination of systems in different physical states but with the same thermodynamic state is called an "ensemble". Ensembles encompass collections of various systems with different characteristics. Two different ensembles were applied in the MD simulations made in the thesis study.

a) Canonical Ensemble (NVT): NVT ensemble ensures that the thermodynamic equilibrium of the system is maintained. It is the sum of systems defined by a constant number of atoms (N), constant volume (V), and constant temperature (T). It is utilized to monitor the actions of atoms within the system at a specified volume and temperature. The total energy of the system, under constant

volume and temperature, is distributed between the kinetic and potential energy components. NVT simulations employ various thermostat methods to maintain a constant temperature throughout the simulation **[144]**.

b) Isobaric-Isothermal Community (NPT): It is the ensemble with a constant number of atoms (N), constant pressure (P) and constant temperature (T). In the NPT, temperature and pressure are kept constant. It is applied to analyze the behavior of the system under constant pressure, atomic number and temperature. Under a certain pressure and temperature, the system volume may change. In biological systems, many processes take place under constant pressure and temperature. The NPT community is important for modeling simulations in accordance with real conditions **[145]**.

In MD simulations, biomolecules are placed in a simulation box of certain dimensions. The contents of this box must be modeled in accordance with the biological environment conditions. Water is usually added to the system as a solvent to provide suitable conditions. There are two different water models commonly used in MD simulations.

a) Implicit Water Model: Implicit models represent solvent behavior in a simple way. In this way, it reduces the calculation time. It is useful for MD simulations of large systems.

b) Explicit (Open) Water Models: Open water models are models that directly reflect the individual interactions of water molecules. In explicit models, the bonding and electrostatic interactions between molecules are clearly defined. For each of the water molecules, atoms representing hydrogen (H) and oxygen (O) have been identified. Commonly preferred open water models are as follows:

i)TIP3P (Three Point Model): In this model, the water molecule is represented by three dots. It contains two hydrogen and one oxygen atom. Atomic charges are defined in a specific order **[146]**.

ii) TIP4P (Four Point Model): The water molecule is represented by four points. It contains one oxygen and three hydrogen atoms. By adding one more charge to the oxygen atom, it is aimed to ensure the

polarization correctly. It provides a better understanding of water properties (e.g., freezing and boiling point) **[147]**.

iii) SPC (Simple Point Charge): Water molecules are represented by three points. It consists of two hydrogen and one oxygen atom. The molecule is defined by partial charges; hydrogen atoms carry a positive charge, while oxygen atoms carry a negative charge. It is suitable for simulating the dynamic properties of water molecules. It is often used in simple macromolecule simulations and in the study of basic water properties **[148]**.

iv) SPC/E (Extended Simple Point Charge): It is a more advanced version of the SPC model. It is often used to obtain more realistic results. It better models the charge distribution of the oxygen atom and the molecular interactions.

v) TIP5P (Five Point Model): The water molecule is represented by five points. It is used to model various phases of water, such as solids, liquids, etc **[149]**.

MD simulations have a wide range of applications in various branches of science and engineering. It can be used in protein three-dimensional structure modeling, study of enzyme reaction mechanisms, and nucleic acid studies when conducting biomolecular research **[150], [151]**. In materials science, MD technique is widely used especially in modeling and structural analysis studies related to polymers and nanomaterials **[152]**. MD simulations are also widely applied in areas such as drug design and modeling, evaluation of the distribution of pollutants in water and air environment, and substance transport through the cell membrane. **[153]**, **[154], [155]**.

3.2.2. *E.Coli* Cell Membrane Modeling and MD Simulations

The cell membrane structures of *E.Coli* bacteria were designed through the CHARMM-GUI server **[156], [157]** in accordance with the membrane compositions obtained from the literature. As stated in the literature, *E.Coli* membrane composition is 75% phosphatidylethanolamine (PE), phosphatidylglycerol 20% (PG) and 5% cardiolipin (CL) **[158]**. 3D structure of the cell membrane to be utilized in the study

was modeled using the simulation parameters CHARMM-GUI. 690 DLPE, 184 DPPG and 46 TMCL molecules were assembled in accordance with the *E. coli* cell membrane composition.

HolPhage-D29 is one of the phage proteins that plays a key role in the mechanism of bacterial lysis. In phage lytic cycles, the bacteriophage first binds to receptors on the target cell membrane and the phage genome is transferred to the bacterium. New phage particles are produced from the phage genome by performing replication and protein synthesis in the bacterial cytoplasm. After the phage genome enters the host bacterial cell and is expressed there, endolysin enzymes and holin proteins are produced that disrupt the peptidoglycan layer of the host, allow the release of newly formed bacteriophages around, and play a critical role in bacterial lysis **[159], [160]**. Holins are small hydrophobic cell membrane proteins that are encoded by the host genome after the phage infects the host. Only when the phage infects the bacterium can the bacterium encode the holin protein. Therefore, it was decided to use the lipid model, which does not contain holin but has the same lipid composition and size, as the control group for the experiments.

The cell membrane model is created by CHARMM-GUI server. The simulation box was filled with water molecules with a TIP3P. Sodium (Na^+) and chloride (Cl^-) ions were added to the box to simulate it under physiological conditions and neutralize the simulation box. First, energy minimization was performed on the initial structure for 5000 steps. After the minimization was completed, the initial structure for the MD simulation was created. Initially, three consecutive NVT simulations were performed at 303.15 Celvin (K) and 1.0 bar for 250 picoseconds (ps) each, under conditions of constant number of particles (N), volume (V), and temperature (T). Subsequently, three NPT simulations were conducted for 500 ps each, maintaining constant number of particles (N), pressure (P), and temperature (T). The SETTLE algorithm was used to constrain the bond length and angle of water molecules. The LINCS algorithm was applied limit the bond length of peptide-forming atoms long-range electrostatic interactions were calculated by the PME method. A constant pressure of 1 bar was utilized with a coupling constant of 1.0 ps, and the water molecules/ions were individually placed in the bath at the specified temperature with a coupling constant of 0.1 ps. Using the Leap-frog algorithm, Newton's law of motion was solved in time

intervals of 2 femtoseconds (fs) **[161]**, **[162]**, **[163]**. All MD simulations performed in the thesis were performed using these parameters.

3.2.3. HolPhage-D29 Protein - Membrane System Modeling and MD Simulations

In the thesis, the behavior of the HolPhage-D29 protein within the *E. coli* cell membrane has been analyzed. Initially, HolPhage-D29 protein was directly incorporated into the *E. coli* cell membrane. A review of the literature indicates that in previous studies, it has been stated that the dimerization process of at least two holin proteins coded by bacteriophages binding to the membrane surface is a necessary step for lesion formation in bacterial cell membranes. However, the mechanism of membrane disruption by holins is still not fully understood. In this thesis, various simulations of HolPhage-D29 have been conducted to understand its membrane disruption mechanism and the behavior of the cell membrane in the presence of HolPhage-D29. System models **(Figure 3.3)** can be listed as follows:

a. HolPhage-D29
b. HolPhage-D29 dimer (monomers combined side by side)
c. HolPhage-D29 dimer (monomers combined in a crossconformation)
d. HolPhage-D29 tetramer (monomers combined side by side)

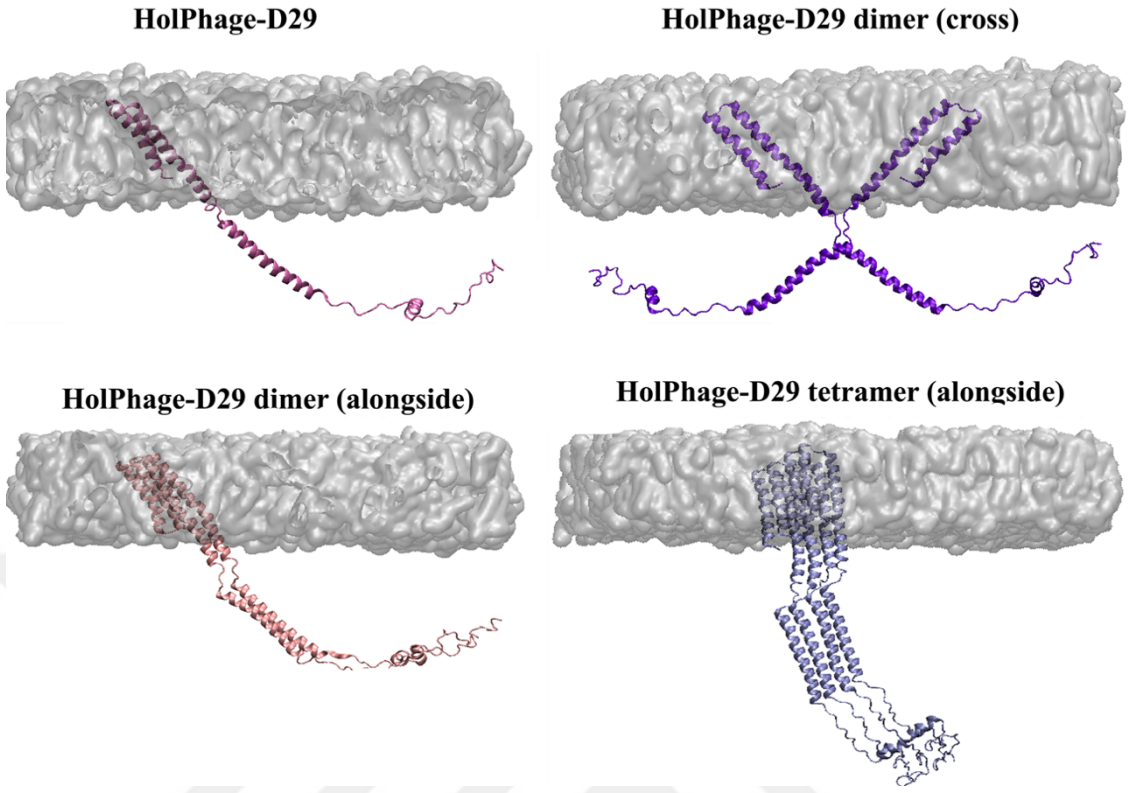


Figure 3.3: System models to be subjected to MD simulation.

All simulations used the same composition of the *E. coli* cell membrane, consisting of DLPE, DPPG, and TMCL molecules in equal proportions. The same conditions were maintained throughout the simulations. Details regarding the composition of the cell membrane model used in each simulation, the number of sodium and potassium atoms used, and the simulation durations are provided in **Table 3.1**.

3.2.4. HolPhage-D29 C-terminal Domain - Membrane System Modeling and MD Simulations

HolPhage-D29 creates holes in the *E. coli* inner cell membrane, thus allowing endolysin enzymes to break down the bacterial cell wall system. Role of the C-terminal domain has been investigated in the studies examining the cell membrane disruption mediated by Phage-D29 **[164], [165]**. In these studies, the C-terminal domain of HolPhage-D29 was fragmented into various lengths, and new peptides were designed.

Results obtained from this research, underscore the significance of the C-terminal domain in the toxic effects on bacterial growth. In another study, it was demonstrated

that the C-terminal domain is indispensable for holin-mediated bacterial cell lysis **[166]**.

Table 3.1. System models prepared for MD simulations.

Simülation	Cell Membrane Composition	Time (ns)	Na^+	Cl^-	Box Size (Å)
HolPhage-D29	DLPE: 690 DPPG: 184 TMCL: 46	400	487	256	17.343 17.343 13.473
HolPhage-D29 dimer (alongside)	DLPE: 630 DPPG: 168 TMCL: 42	300	533	321	19.476 19.476 12.811
HolPhage-D29 dimer (cross)	DLPE: 936 DPPG: 248 TMCL: 62	300	652	340	19.476 19.476 12.811
HolPhage-D29 tetramer (alongside)	DLPE: 911 DPPG: 240 TMCL: 60	300	893	586	19.012 19.012 15.053

In this thesis, the C-terminal domain of HolPhage-D29, which has previously been shown to exert toxic effects in *E. coli* through experimental methods, was modeled (specifically, the protein segment between Leu 69 and Arg 141). The region corresponding to the residues between Leucine 69 and Arginine 141 of HolPhage-D29, previously modeled using AlphaFold **[86]**, was separated by YASARA Structure program **[108]**.

Newly created peptide was subjected to an energy minimization. *E. coli* cell membrane was modeled similarly to other simulations. HolPhage-D29 C-terminal peptide was

positioned close to the cytoplasmic side of the cell membrane. Established system was subjected to a 300 ns MD simulation. Simulation parameters were consistent with those used in previous simulations. System information is provided in **Table 3.1**.

3.2.5. *S.aureus* Cell Membrane Modeling and MD Simulation

The cell membrane of *S. aureus* is primarily composed of phosphatidylglycerol molecules. The lipid composition of the cell membrane is as follows: 57% phosphatidylglycerol (PG), 38% lysin-phosphatidylglycerol (LPG), and 5% cardiolipin. 3D structure of the cell membrane was generated using the CHARMM-GUI server simulation parameters. 528 DPPG, 336 DLPG, and 48 TMCL1 molecules were assembled in accordance with the composition of the *S. aureus* cell membrane.

3D structure of the cell membrane was generated by CHARMM-GUI server. S. *aureus* cell membrane model was simulated using MD simulations with the CHARMM36 force field in the GROMACS 2021 program **[167]** . The simulation box was filled with TIP3P water molecules.1022 sodium and 110 chloride ions were added in the box for simulate under physiological conditions. Initially, energy minimization was applied to the starting structure in 5000 steps. After the minimization, the starting structure for the MD simulation was established. Subsequently, an NVT simulation was performed three times for 250 ps at a constant number of particles (N), volume (V), and temperature (T) of 303.15 K and 1.0 bar. Following this, NPT simulation was conducted three times for 500 ps at a constant number of particles (N), pressure (P), and temperature (T). The SETTLE algorithm was employed to constrain the bond lengths and angles of the water molecules. The LINCS algorithm was utilized to constrain the bond lengths of the atoms constituting the peptide. Long-range electrostatic interactions were calculated using the PME method. Coupling constant of 1.0 ps was applied with a constant pressure of 1 bar, and water molecules/ions were separately placed in the bath at a specified temperature with a coupling constant of 0.1 ps. Newton's equations of motion were solved using the leap-frog algorithm at time intervals of 2 fs. *S. aureus* cell membrane was subjected to a 400 ns MD simulation.

3.2.6. HolPhage-K Protein - Membrane System Modeling and MD Simulations

In this study, the behavior of HolPhage-K protein in the *S. aureus* cell membrane has been analyzed. Initially, HolPhage-K protein was directly integrated into the *S. aureus* cell membrane. Various simulations were conducted to understand the membrane disruption mechanism of HolPhage-K. System models **(Figure 3.3)** can be listed as follows:

a. HolPhage-K

b. HolPhage-K dimer (monomers combined side by side)

c. HolPhage-K dimer (monomers combined in a cross conformation)

d. HolPhage-K tetramer (monomers combined cross)

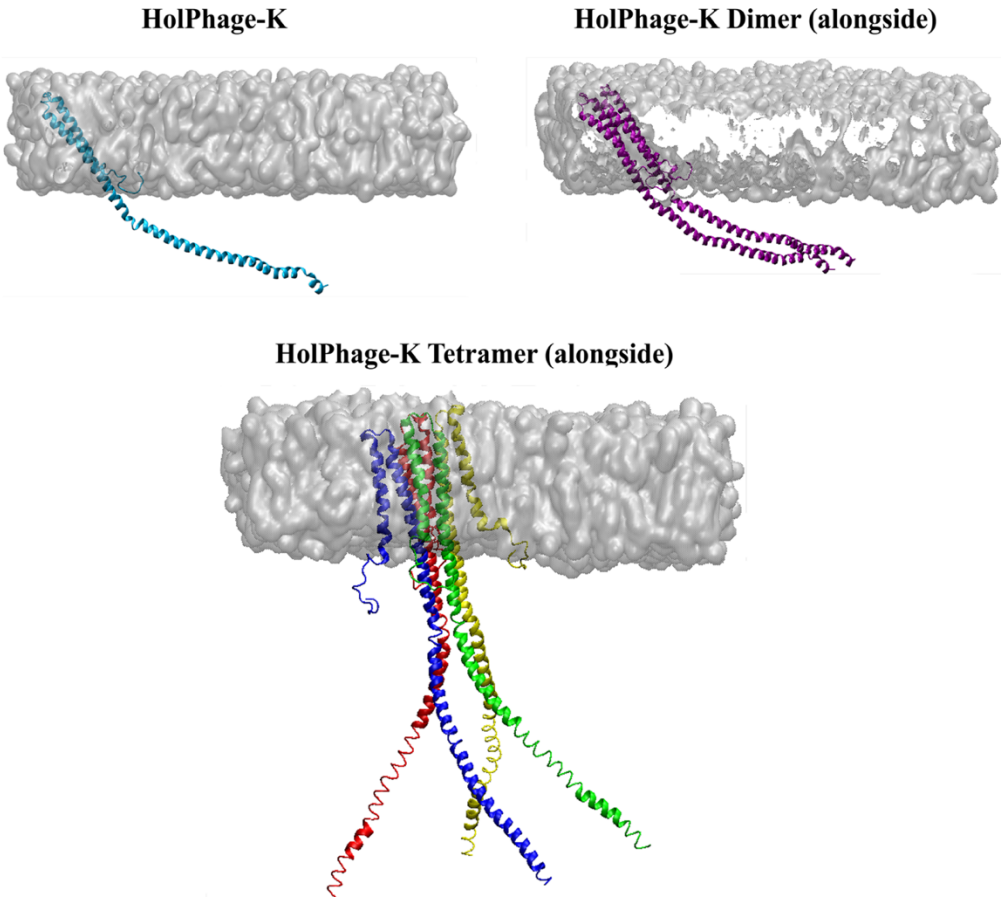


Figure 3.4: System models prepared for MD simulations.

All simulations used the same composition of the *S. aureus* cell membrane, consisting of DLPG, DPPG, and TMCL molecules in equal proportions. The same conditions were maintained throughout the simulations. The general parameters used in the simulations are as follows: All system was modeled with CHARMM-GUI server. The simulation box was filled with TIP3P water molecules. Sodium (Na^+) and chloride (Cl^-) ions were added in the box to simulate under physiological conditions. Initially, energy minimization was performed in 5000 steps. After minimization, the starting structure for the MD simulation was created. Subsequently, three NVT simulations of 250 ps each were conducted at 303.15 K and 1.0 bar, maintaining a constant number of particles (N), volume (V), and temperature (T); followed by three NPT simulations of 500 ps each, maintaining a constant number of particles (N), pressure (P), and temperature (T). The SETTLE algorithm was used to constrain the bond lengths and angles of water molecules. LINCS algorithm was applied to constrain the bond lengths of atoms forming peptides; long-range electrostatic interactions were calculated using the PME method. A constant pressure of 1 bar was used with a 1.0 ps coupling constant, and water molecules/ions were separately placed in the specified temperature bath with a 0.1 ps coupling constant. Using the leap-frog algorithm, Newton's laws of motion were solved at 2 femtosecond time intervals.

Details regarding the composition of the cell membrane model utilized in each simulation, the number of sodium and potassium atoms used, and the simulation durations are provided in **Table 3.2**.

Table 3.2. System models prepared for MD simulations.

Simülation	**Cell Membrane Composition**	**Time (ns)**	**Na^+**	**Cl^-**	**Box Size (Å)**
HolPhage-K	DLPG: 456 DPPG: 687 TMCL:60	400	487	256	16.745 16.745 14.756
HolPhage-K dimer (alongside)	DLPG: 532 DPPG:803 TMCL:70	300	1852	407	20.935 20.935 13.680
HolPhage-K tetramer (cross)	DLPG: 341 DPPG: 523 TMCL:46	300	1463	481	17.406 17.406 22.257

4. RESULTS

4.1. AI Based Protein Modeling of HolPhage-D29

In this study, TMD and C-terminal region of the bacteriophage D29 holin protein were predicted in 3D strucuture by AlphaFold. Structural stability and reliability of the modeled region were evaluated by various analysis modeling process. The obtained models were detailed with multiple sequence alignment (MSA), predicted alignment error (PAE) and predicted Local Distance Difference Test (pLDDT) analyses. Comprehensive analyses of the modeling results are presented below.

TMD of HolPhage-D29 was modeled by AlphaFold. Resulting structures were subjected to MSA analysis. This method aligns multiple homologous protein sequences to the target sequence, enabling the evaluation of both sequence coverage at each amino acid position and the sequence identity of each aligned sequence relative to the query. This analysis is essential for assessing the reliability of the homologous sequences selected for modeling. As shown in the **Figure 4.1**, the sequences used for modeling exhibit high similarity and strong coverage across the TMD region, indicating that reliable homologs were employed in the modeling process.

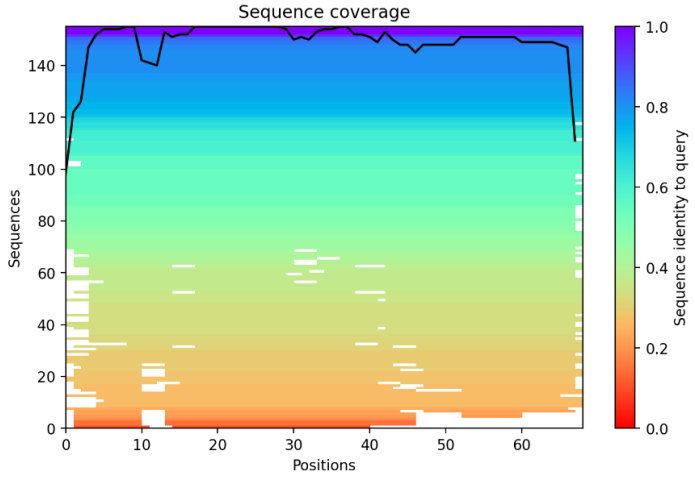


Figure 4.1: TMD sequence coverage graph obtained as a result of MSA. The color gradient shows the degree of similarity of the sequences at each positionto the target sequence. The upper black line represents the coverage ratio.

pLDDT scores per position for different AlphaFold models (rank_1–rank_5) of the HolPhage-D29 TMD region are presented in **Figure 4.2**. In all the modeled structures, the pLDDT values for the central regions of the TMD were observed to remain at approximately 90 and above. The analysis results indicate that these regions were modeled with high structural reliability. In contrast, the LDDT scores for the terminal regions of the protein were lower. Overall, the rank_1 model was identified as the one with the highest structural reliability among the models.

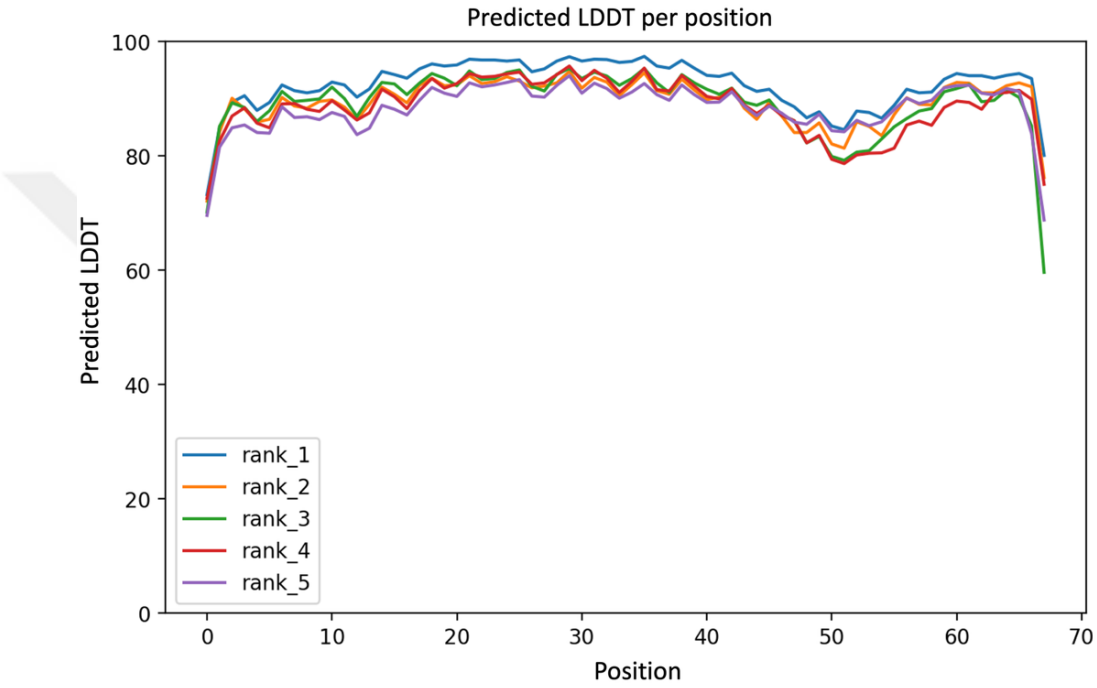


Figure 4.2: pLDDT values for each amino acid position of five different TMD models. Higher scores indicate greater reliability of structural prediction.

PAE maps of five different AlphaFold models (rank_1–rank_5) belonging to the HolPhage-D29 TMD region are given in **Figure 4.3**. Low error values (blue areas) were observed in all models. The majority of these blue areas indicate that the models consist of consistent alignments. Examination of the maps further supports that the central regions of the protein structures were modeled with high confidence. Among the five models, the rank_1 model displays the lowest alignment errors, clearly indicating its superior structural accuracy compared to the others.

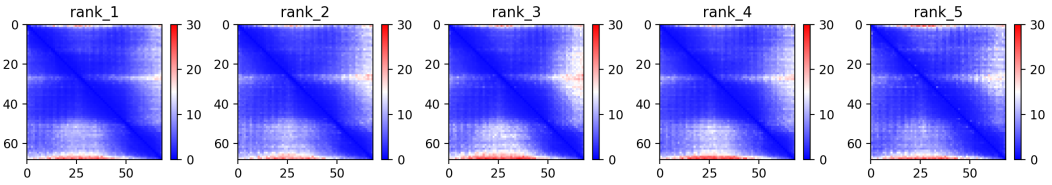


Figure 4.3: PAE maps of five different TMD models (rank_1–rank_5) generated by AlphaFold. Low PAE values (blue areas) indicate high cross-regional reliability.

MSA of the C-terminal region of HolPhage-D29 revealed high sequence coverage in the central regions. However, both sequence identity and coverage were markedly reduced in the terminal regions, suggesting that homologous sequences are less conserved at these positions **(Figure 4.4)**.

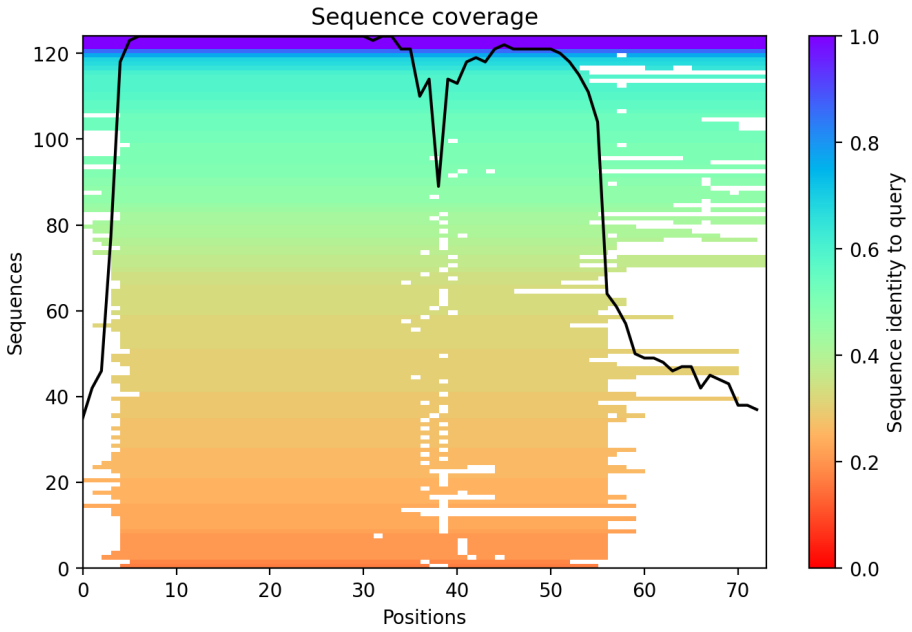


Figure 4.4: C-terminal sequence coverage graph obtained as a result of MSA. The color gradient shows the degree of similarity of the sequences at each position to the target sequence. The upper black line represents the coverage ratio.

Comparison of the predicted pLDDT scores across five different models indicated higher confidence values within the first 20 residues. In contrast, structural uncertainty increased in the central part of the C-terminal region.

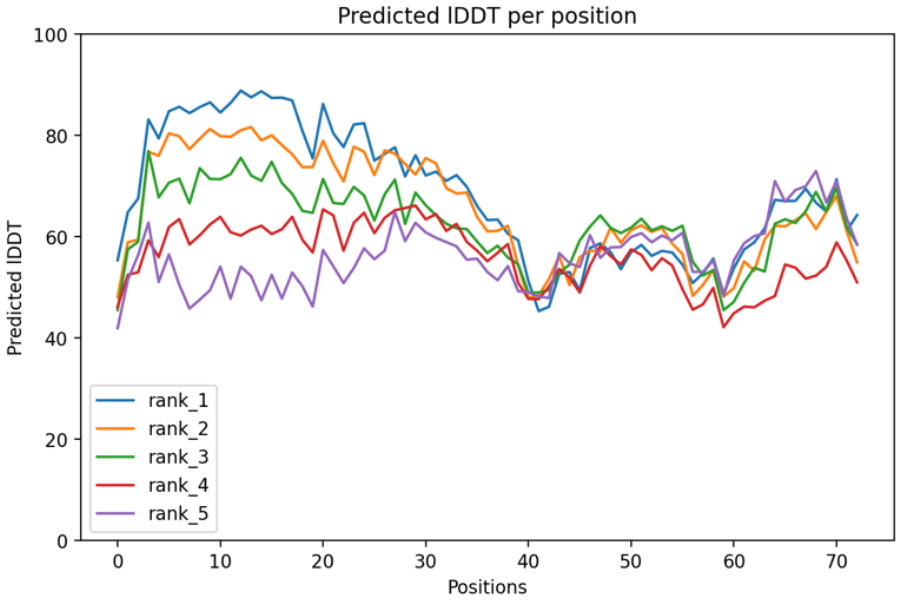


Figure 4.5: Predicted pLDDT values for each amino acid position of five different C-terminal models. Higher scores indicate greater reliability of structural prediction.

PAE maps for models rank_1 through rank_5 showed low alignment errors (blue regions) in the central domain, whereas error values increased significantly toward the termini. These results indicate that certain parts of the C-terminal region are structurally well-defined, while others remain poorly predicted.

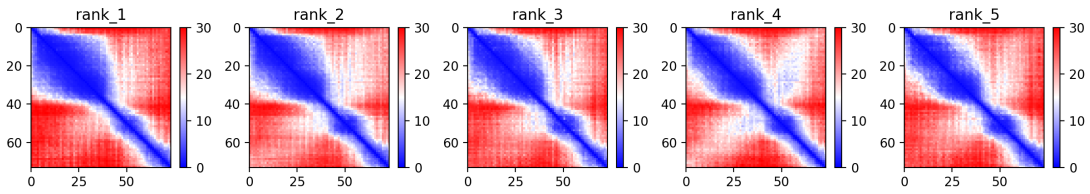


Figure 4.6: PAE maps of five different C-terminal models (rank_1–rank_5) generated by AlphaFold. Low PAE values (blue areas) indicate high cross-regional reliability.

4.1. Homology Modelling of HolPhage-K

167-amino-acid of HolPhage-K was modeled using a hybrid modeling approach. Amino acid residues between positions 1–24 and 24–167 were modeled separately using appropriate structural templates via SWISS-MODEL platform.

Ramachandran plot is a graphical representation that displays the backbone torsion angles φ (phi) and ψ (psi) of amino acid residues on a two-dimensional plane. It allows for the assessment of structural accuracy by evaluating the conformational space occupied by these angles. The plot categorizes regions as *most favored* (A, B, L), *additionally allowed*, *generously allowed*, and *disallowed* regions. In an energetically stable protein model, most residues are expected to fall within the most favored regions **[113]**. Ramachandran plot analysis was performed for the modeled HolPhage-K protein to evaluate its structural validity **(Figure 4.7)**. Upon examination of the plot, it was observed that 97.3% of the 167 amino acid residues were in the most favored regions, while 2.7% were found in the additionally allowed regions. The absence of any residues in the generously allowed or disallowed regions confirms that the model is structurally balanced. These findings supported that 3D structure of HolPhage-K was well modeled. The analysis results show that the modeled structure is quite like the experimentally reported protein structures.

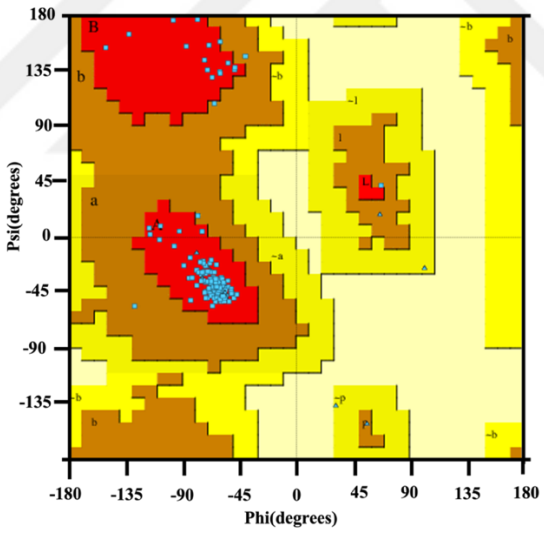


Figure 4.7: Ramachandran plot analysis for HolPhage-K 3D model.

4.3 Molecular Dynamics Simulations

4.3.1 *E. Coli* Cell Membrane Modeling And MD Simulations

E. coli cell membrane was modeled using an appropriate number of DPPE, TMCL, and DLPG molecules. System was subjected to 400 ns MD simulation. **Figure 4.8**

presents the data for three key structural parameters calculated throughout simulation: Root Mean Square Deviation (RMSD), Solvent Accessible Surface Area (SASA), and Radius of Gyration (Rg). RMSD measures the deviation of the protein backbone from its initial conformation over the course of simulation. It is commonly used to evaluate structural stability and conformational changes of macromolecules **[168]**. Analysis of the simulation data revealed that the RMSD value initially measured around 3 nm and gradually increased, stabilizing above 6 nm.This indicates that structure reached conformational equilibrium during the simulation **(Figure 4.8 – A).** SASA measures the surface area of the protein that is accessible to solvent. Decrease in SASA values is typically observed when the macromolecule undergoes folding. Upon examination of the graph, SASA values were initially around 1200 nm^2 but gradually decreased and stabilized within the range of 1100–1150 nm^2 **(Figure 4.8 – B)**. This suggests that structure became solvent-exposed regions were reduced .

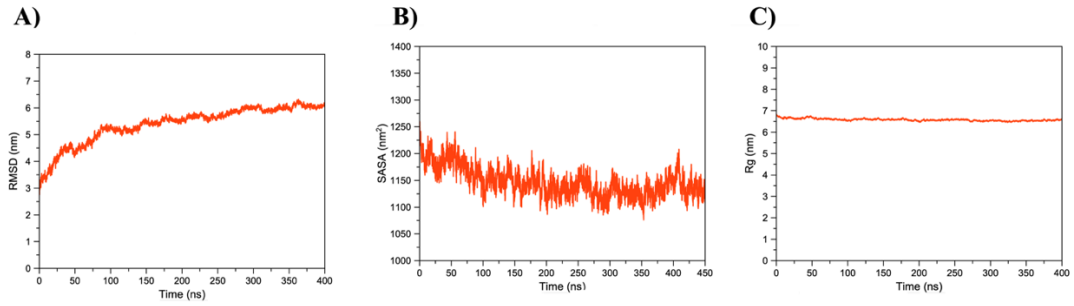


Figure 4.8: Results of A) RMSD, B) SASA, and C) Rg analyses throughout the 400 ns MD simulation.

Rg is a parameter that measures the compactness of a macromolecular structure. It represents the average distance of the atoms from the center of mass of the 3D structure **[169]**. Rg value was observed to remain around 6.8–7.0 nm during the MD simulations **(Figure 4.8 – C)**. These results indicate that overall mass distribution and level of compactness were largely maintained.

Figure 4.9 presents structural snapshots obtained from the 400 ns MD simulation of *E. coli* cell membrane system composed solely of phospholipids (DLPG, DPPG, and TMCL), taken at 1^{st}, 100^{th}, 200^{th}, 300^{th}, and 400^{th} ns. Initially, a smooth membrane surface is observed. As the simulation progresses, certain irregularities and localized undulations appear on surface. Simulation results indicate that membrane thickness, fluidity, and flexibility can vary over time. These changes are primarily attributed to

types of phospholipids that constitute the membrane. Previous studies have reported that in membranes containing TMCL, phospholipids tend to form clusters, which can influence membrane topology **[171], [172]**.

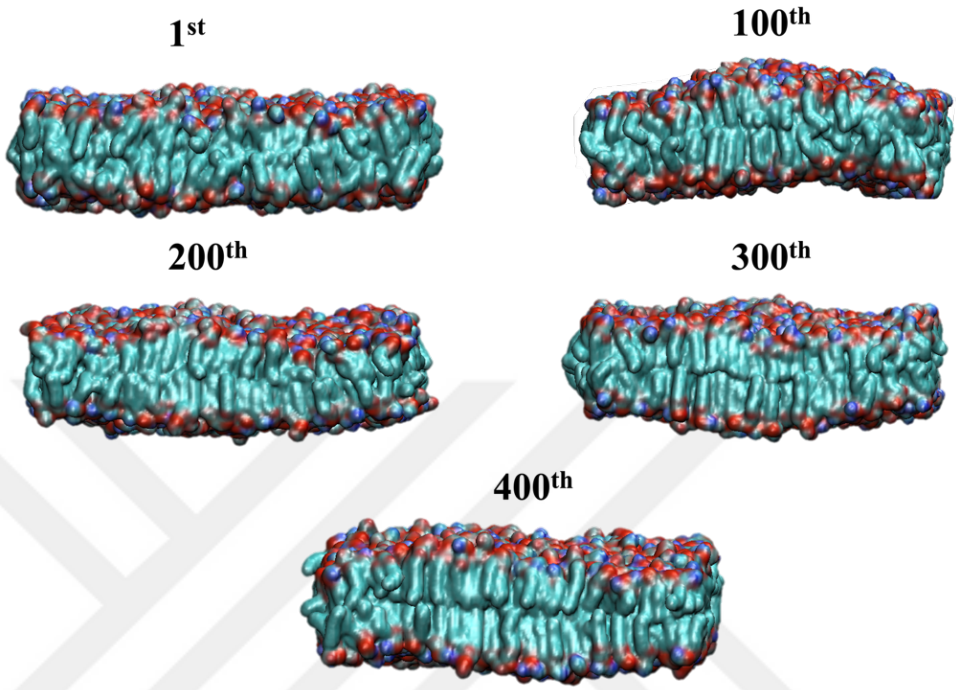


Figure 4.9: Snapshots from 400 ns MD simulation of *E. coli* cell membrane. Shown respectively at 1st, 100th, 200th, 300th, and 400th ns.

4.3.2. *E. coli* Cell Membrane & HolPhage-D29 MD Simulations

HolPhage-D29 was embedded into the *E. coli* cell membrane model and subjected to a 400 ns MD simulation. **Figure 4.10** presents the results of RMSD, SASA, and Rg analyses obtained from the simulation. RMSD values **(Figure 4.10 – A)** showed a gradual increase during the first half of the simulation, followed by pronounced fluctuations between 200–300 ns. These fluctuations in RMSD indicate a structural rearrangement within the protein–membrane system. Moreover, RMSD profile suggests that the system did not remain in a single stable conformation but instead exhibited transient intermediate states throughout the simulation. The increase and fluctuation observed in SASA values **(Figure 4.10 – B)** indicate an expansion in the solvent-accessible surface area of the protein over time. This could be a result of structural rearrangements on the protein surface induced by its interaction with the cell

membrane. Rg graph **(Figure 4.10 – C)** displays a gradual decrease in values over time, suggesting that the system transitioned into a more compact structure during the simulation. Taken together, these analyses prove that HolPhage-D29 exhibited a dynamic structure within the *E. coli* membrane. This dynamic behavior may have triggered the structural changes necessary for potential pore formation in the membrane.

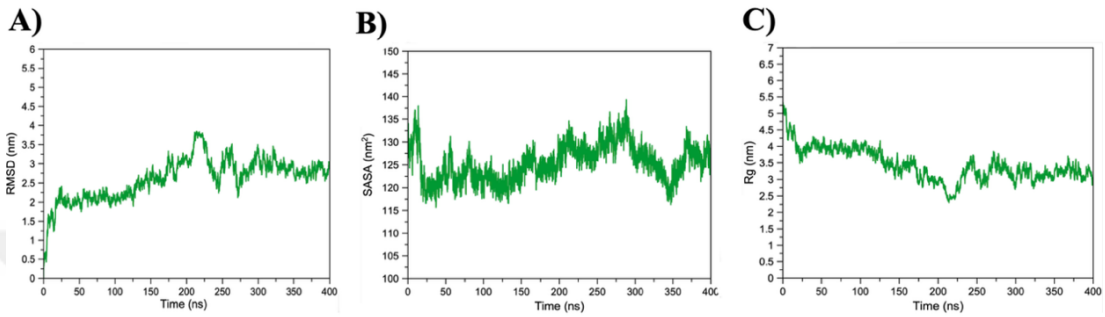


Figure 4.10: Results of A) RMSD, B) SASA, and C) Rg analyses throughout the 400 ns MD simulation.

Figure 4.11 presents a comparative analysis of RMSD, SASA, and Rg parameters for *E. coli* cell membrane obtained from MD simulations performed in presence and absence of the HolPhage-D29 holin protein. In RMSD analysis **(Figure 4.11–A)**, system containing HolPhage-D29 exhibited higher RMSD values compared to membrane-only control system, reaching approximately 6.5–7.0 nm. These results suggest that the presence of protein increases the flexibility of membrane structure.

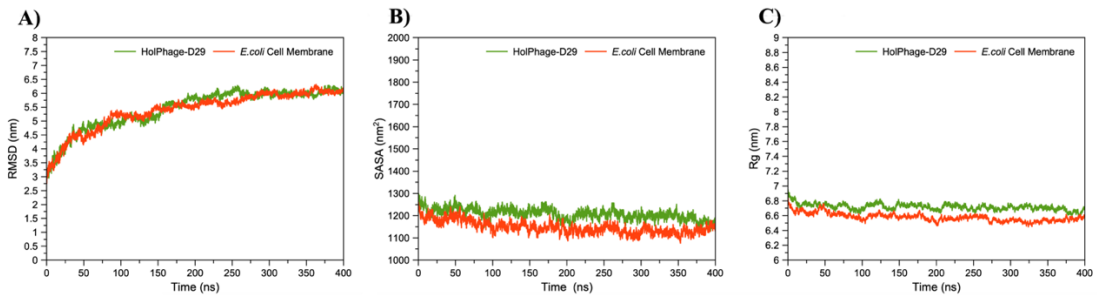


Figure 4.11: Comperative results of A) RMSD, B) SASA, and C) Rg analyses throughout the 400 ns *E.coli* Cell Membrane and HolPhage-D29 MD simulations.

According to SASA results **(Figure 4.11 - B)**, system interacting with HolPhage-D29 protein retained a larger solvent-accessible surface area (approximately 1250–1300

nm²). This indicates that protein may have partially disrupted membrane surface, thereby enhancing solvent accessibility. Rg analysis **(Figure 4.11 - C)** shows that, membrane in the presence of protein is more loosely organized. In this case, Rg value remained around 6.8 nm, which suggests a less compact membrane architecture.Taken together, differences observed in both protein-containing and control systems may represent initial steps of membrane destabilization that precede pore formation.

Figure 4.12 presents trajectory analysis results obtained from MD simulation of HolPhage-D29. Snapshots taken at different time points during the simulation reveal conformational changes in the positions of TMDs and C-terminal region over time. As the simulation progresses (particularly after 200 ns) C-terminal appears to fold and adopt a more compact conformation while moving closer to membrane. At the 300–400 ns time points, noticeable bending is observed within the TMD regions.

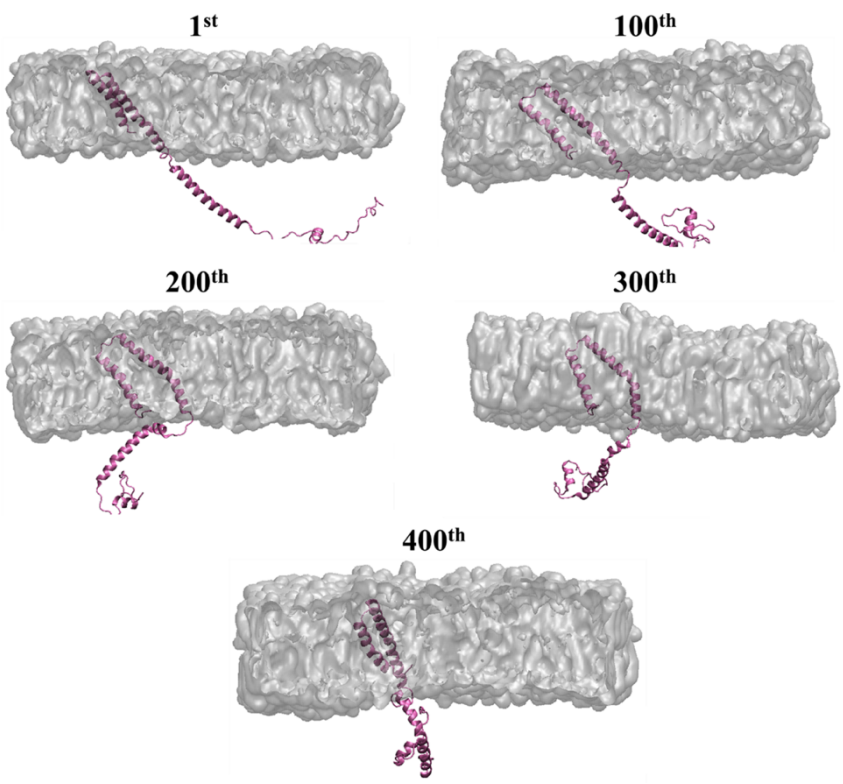


Figure 4.12: Snapshots from 400 ns MD simulation of HolPhage-D29 & *E.coli* cell membrane simulations. Shown respectively at 1st , 100th , 200th, 300th, and 400th ns.

Bendix analysis in **Figure 4.13** quantitatively demonstrates this structural alteration. Bendix is a method used to analyze the degree of bending in α-helical regions of

proteins over time. It illustrates the transition of helices from a linear to a more curved configuration based on a color scale **[170]**. Curvature (bendix) analysis performed for the C-terminal segment of HolPhage-D29, spanning residues 70–140, revealed notable structural alterations **(Figure 4.14)**. Helical segment exhibited a relatively straight and stable structure at the beginning of the simulation (1. ns). Later time points—particularly at 300 and 400 ns—marked bending and increased curvature were observed. High curvature values were especially prominent beyond residue 100, indicating that this region became conformationally more flexible over time. These structural changes suggest a partial loss of α-helical arrangement and a transition of the C-terminal region into a more dynamic state throughout the simulation. Overall, the results indicate that the C-terminal helix possesses an intrinsically flexible nature.

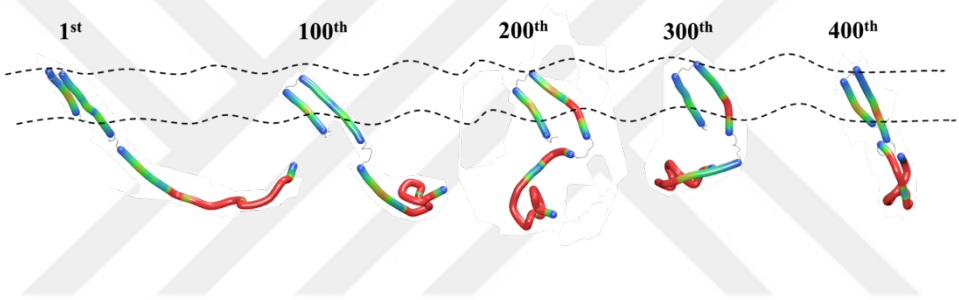


Figure 4.13: Bendix analysis of the HolPhage-D29 protein. Bendix analyses are mapped according to a color scale (blue: low – red: high). Shown respectively at 1st , 100th , 200th, 300th, and 400th ns.

HolPhage-D29 exhibited significant conformational flexibility within the membrane environment throughout the simulation. Notably, C-terminal region showed dynamic mobility in the aqueous environment, suggesting a higher potential for interaction with the membrane **(Figure 4.14)**.

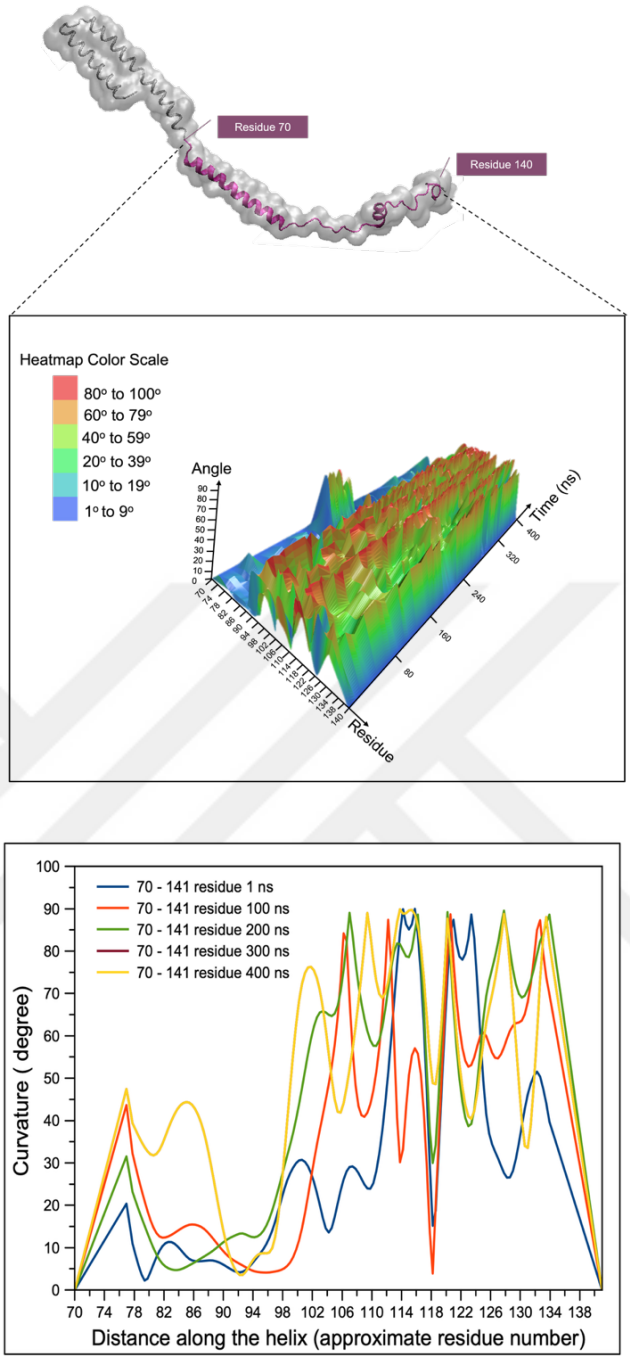


Figure 4.14: Time-dependent curvature analysis of the C-terminal segment (residues 70–140) of the HolPhage-D29 protein. The bottom panel presents the conformational and bending changes of the region from 1 ns to 400 ns. Curvature analyses are mapped according to a color scale (blue: low – red: high). The graph in the lower right corner shows the time-dependent variation in curvature degrees along the helical segment based on residue position.

To evaluate the impact of the HolPhage-D29 protein on membrane structure, the analyses presented in **Figure 4.15** were conducted. The fraction of contact with the

opposite leaflet (FCOL) measures the frequency with which phospholipids interact with the opposing leaflet. The fraction of mass overlap (FMO) and the width of the overlap region (WOR) quantify the degree of physical proximity and overlap between the two leaflets of the modeled membrane. Since FCOL and FMO are ratio-based analyses, their values are normalized between 0 and 1, where 0 indicates no contact or overlap, and 1 represents the maximum level. Upon examining the graphs, FCOL values were found to be similar in both systems (~0.041). However, FMO and WOR values showed a slight increase in the HolPhage-D29-containing system, suggesting enhanced physical proximity and structural alignment between the membrane leaflets **[171]**.

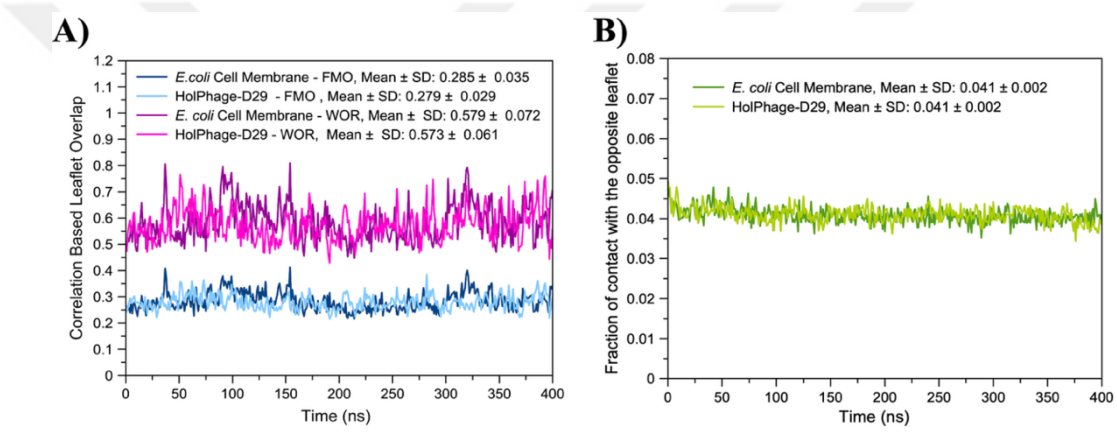


Figure 4.15: A) Correlation-based leaflet overlap analysis showing the FMO and WOR over time for systems with and without HolPhage-D29 (HolPhage-D29–containing system (dark blue) and the control system (light blue)), B) Time-dependent changes in the FCOL analysis (light green: HolPhage-D29, dark green: control).

In the 2D thickness maps shown in **Figure 4.16**, local thinning and fluctuations in membrane thickness are more pronounced in the HolPhage-D29-containing system (bottom). Analysis of the time-dependent thickness data revealed similar average membrane thickness values in both systems (Control: 37.91 ± 0.51 Å; HolPhage-D29: 37.86 ± 0.61 Å) **(Figure 4.16 - C)**. Greater fluctuation tendencies were observed over time in HolPhage-D29 system cell membrane. This indicated that the presence of the protein locally affects membrane flexibility and structural integrity.

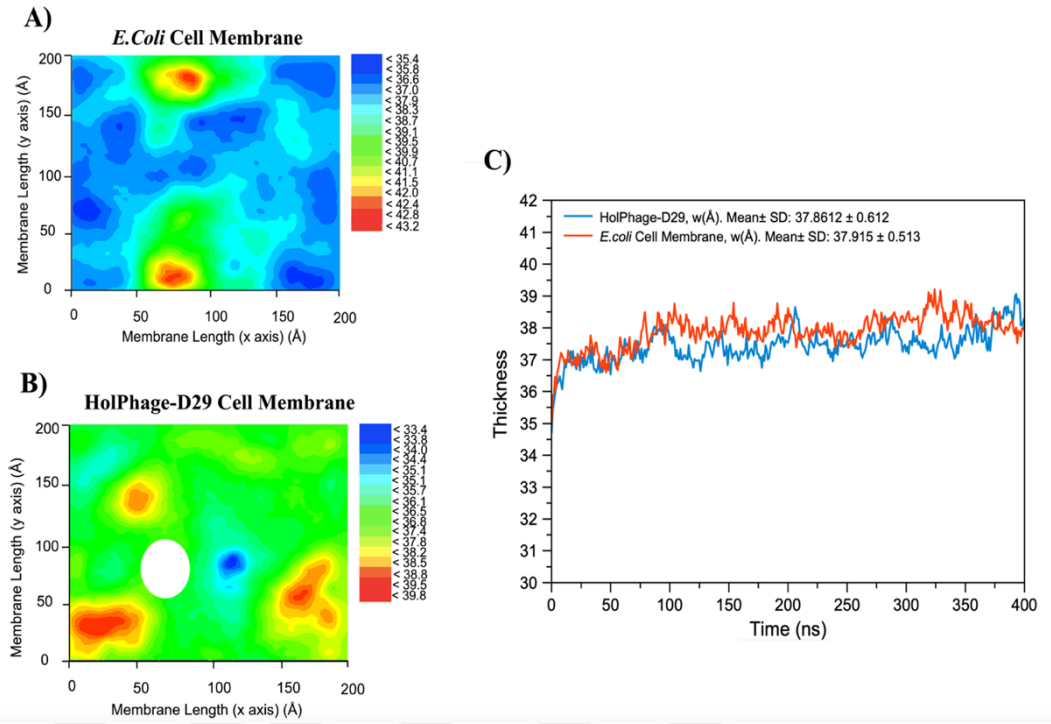


Figure 4.16: A) 2D membrane thickness map of the control system (top), B) 2D thickness map in the presence of HolPhage-D29, and C) Time-dependent changes in average membrane thickness.

4.3.3. *E.coli* Cell Membrane & HolPhage-D29 Dimer MD Simulations

4.3.3.1 HolPhage-D29 Dimer Alongside MD Simulations

RMSD, SASA, and Rg analyses were performed to evaluate the structural stability of the HolPhage-D29 dimer during the 300 ns MD simulation. RMSD plot **(Figure 4.17-A)** indicates that the protein underwent significant conformational changes over time, reaching approximately 3.5 nm, but stabilized during the final 50 ns of the simulation. The SASA analysis **(Figure 4.17-B)** shows a notable decrease in the solvent-accessible surface area, suggesting that the protein adopted a more compact structure. Similarly, observed decrease in Rg values **(Figure 4.17-C)** supports the notion that protein's overall dimensions became more condensed.

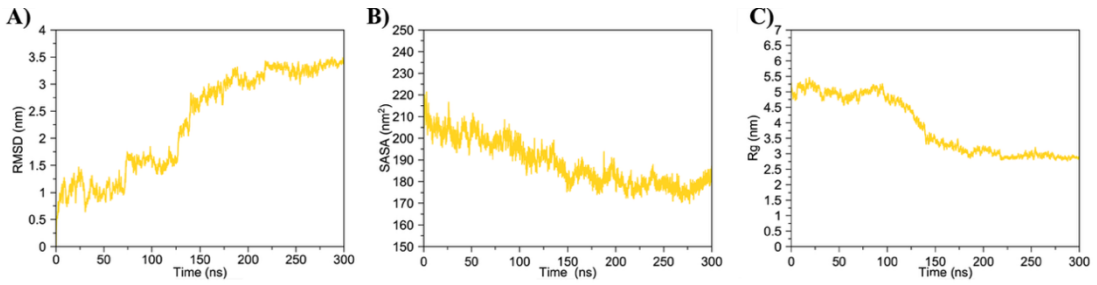


Figure 4.17: MD simulation of HolPhage-D29 dimer with time-dependent A) RMSD, B) SASA and C) Rg analyses.

Equilibration status of cell membrane structures of the system containing HolPhage-D29 dimer and control system throughout the simulation was evaluated by comparing RMSD, SASA and Rg values. RMSD values **(Figure 4.18 - A)** show that both systems undergo conformational changes, but presence of D29 dimer leads to a higher deviation and increased structural flexibility. In contrast, membrane structure in the simulation reached a stable structure starting from approximately 100 ns. SASA values **(Figure 4.18 - B)** and Rg values **(Figure 4.18 - C)** remained significantly higher in the system containing dimer. However, this is due to the presence of more lipid molecules in the HolPhage-D29 system. Decreasing SASA and Rg values in the system with D29 dimer indicate a compression between lipid molecules.

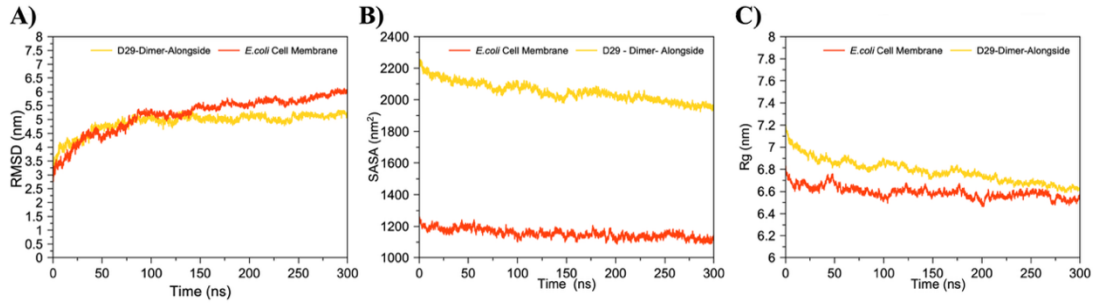


Figure 4.18: Comparison of A) RMSD, B) SASA, and C) Rg analyses between the membrane in the HolPhage-D29 dimer system (yellow) and the system containing only the *E. coli* cell membrane (orange).

Conformational change of the HolPhage-D29 dimer during the simulation was assessed by trajectory analysis. Initially, the dimer model showed a distinct reorientation, with C-terminal regions extending into the cytoplasmic space, particularly at 200 ns, with dimer aligning more tightly to the membrane plane. At 300 ns, the protein was found to be more deeply embedded in the lipid bilayer and the tail was packed very close to the membrane. These observations indicated that the

HolPhage-D29 dimer adapts to the membrane environment. The folds in the figure are consistent with the SASA and Rg results.

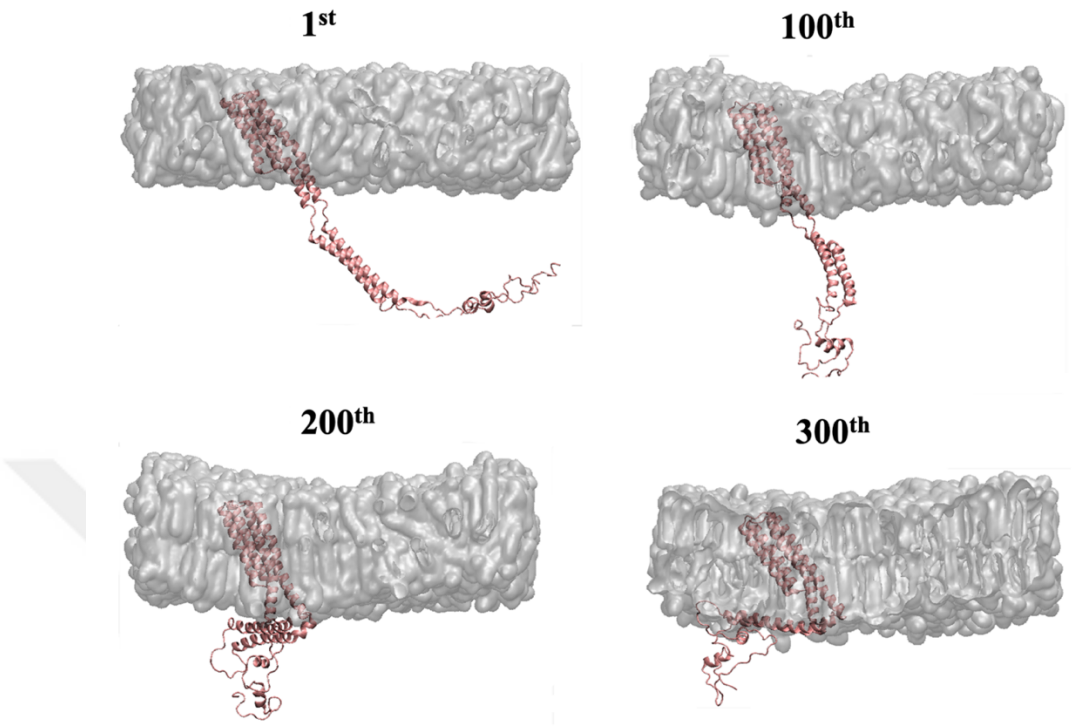


Figure 4.19: Snapshots from 400 ns MD simulation of HolPhage-D29 & *E.coli* dimer cell membrane simulations. Shown respectively at 1st , 100th , 200th, 300th, and 400th ns.

Distance analysis was performed to understand the interaction level between the C-terminal region of the HolPhage-D29 dimer and the *E. coli* membrane. Throughout the simulation, the distance variations between selected residues from the C-terminal region and the membrane were monitored **(Figure 4.20)**. Polar residues such as Thr70, Asn90, and Gln100 were observed to be positioned closer to the hydrophilic head groups of the lipids, while hydrophobic residues like Val80 and Ala105 interacted with the apolar interior regions of the membrane **(Figure 4.21)**. These findings suggest that the localization of residues may play a critical role in protein-lipid selectivity and physical compatibility with the membrane.

Upon evaluating the distance analyses, it was found that the selected residues in both chains of the dimer gradually approached the membrane during the simulation. In particular, when Ala105 residues in chains A and B were taken as reference points, a significant decrease in the distance between the C-terminal ends and the lipids was

observed. The similarity in distance dynamics across both chains indicates that the protein exhibits a symmetric lipid interaction profile across the membrane.

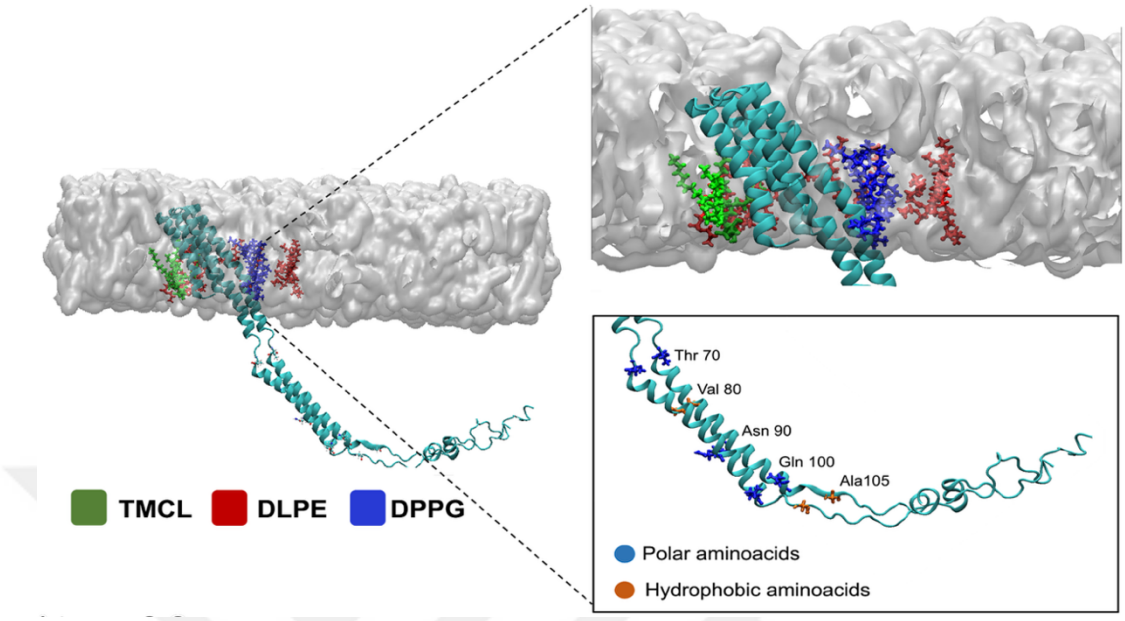


Figure 4.20: Location of HolPhage-D29 dimer in *E. coli* cell membrane and its relationship with various lipid species (TMCL – green, DLPE – red, DPPG – blue). In the zoomed section, selected polar (blue) and hydrophobic (orange) amino acid residues (Thr70, Val80, Asn90, Gln100, Ala105) on both chain are shown.

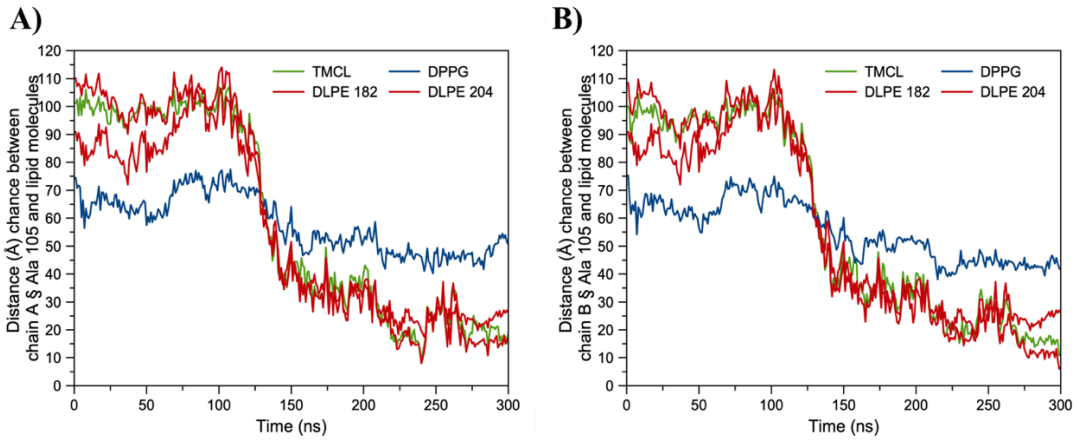


Figure 4.21: A) Comparison of the time-varying distances between the Ala105 residue on chain A and B) B of the HolPhage-D29 dimer and different lipid molecules (TMCL, DLPE, DPPG).

Thickness maps and time-dependent thickness changes **(Figure 4.22 - C)** of the *E. coli* cell membrane **(Figure 4.22 - A)** and the membrane system containing HolPhage-D29 dimer **(Figure 4.22. - B)** are presented. When the average thickness values were

compared, it was determined HolPhage-D29 dimer system (40.641 ± 1.218 Å) was 2.73 Å thicker than the control membrane (37.915 ± 0.513 Å). This indicated that a physical expansion along the cell membrane may occur in the presence of the dimer.

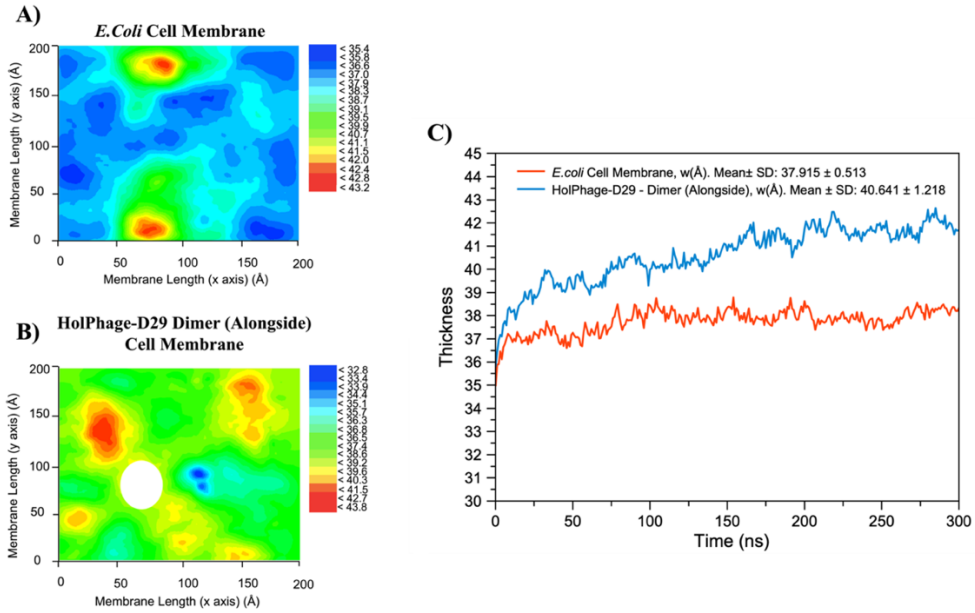


Figure 4.22: A) Membrane thickness heatmap of the *E. coli* cell membrane alone, B) Heatmap of the membrane containing the HolPhage-D29 dimer, C) Time-dependent comparison of average membrane thickness values between the two systems.

When the leaflet overlap analysis was examined **(Figure 4.23 –A)**, both the width of the overlapping region (0.722 ± 0.092 nm) and the fractional mass overlap (0.342 ± 0.036) were significantly higher in the dimer-containing system compared to the control. This increase indicates enhanced alignment and physical proximity between the membrane leaflets. In contrast, **Figure 4.23 – B** shows that the fraction of atoms in contact with the opposite leaflet remained at similar levels in both systems (approximately 4%). These findings suggest that the structural integrity of the membrane was preserved, with no evidence of collapse or pore formation.

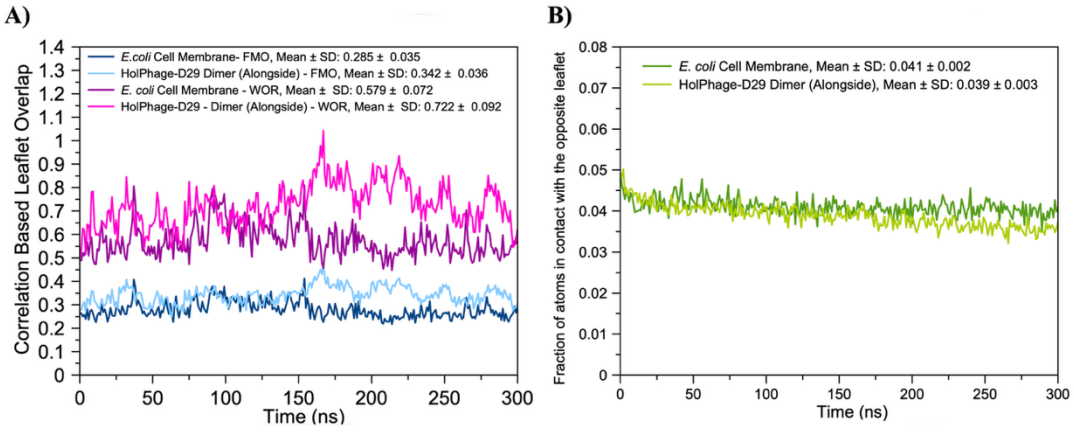


Figure 4.23: A) Change in overlap width and mass fraction values of *E. coli* membrane (blue) and HolPhage-D29 dimer-containing membrane (purple) over time in correlation-based leaflet overlap analysis, B) Comparison of the atom ratio in contact with the opposite leaflet over time between the two systems.

4.3.3.2 HolPhage-D29 Dimer Cross MD Simulations

300 ns MD simulation was conducted for the homodimeric form of HolPhage-D29 protein, in which the monomers were arranged in a cross-oriented configuration. RMSD plot indicates that the structure reached a stable conformation around 3.7–3.9 nm. SASA analysis showed a gradual decrease from approximately 260 nm² to 230 nm² throughout the simulation, suggesting a reduction in solvent-exposed surface area. Similarly, Rg decreased from ~5.5 nm to ~3.2 nm, confirming that the structural compactness increased over time **(Figure 4.24)**.

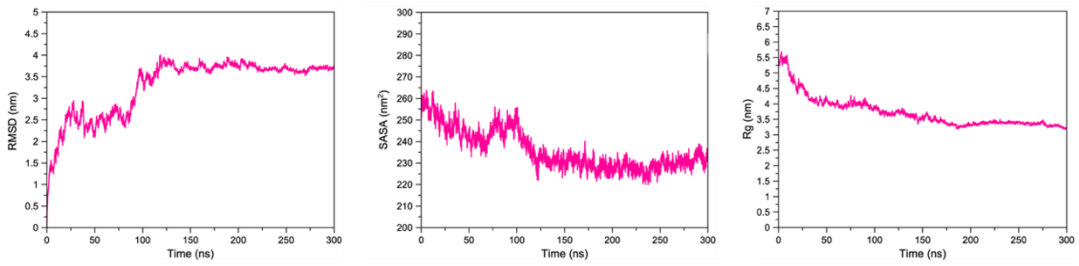


Figure 4.24: MD simulation of HolPhage-D29 dimer (cross) with time-dependent A) RMSD, B) SASA and C) Rg analyses.

Figure 4.25 A–C presents a comparative analysis of the structural parameters between *E. coli* cell membrane and membrane system containing cross-oriented HolPhage-D29 dimer. RMSD analysis shows a gradual increase in HolPhage-D29 dimer system,

reaching approximately 7.0 nm over time, which may indicate higher conformational flexibility. SASA and Rg values for the HolPhage-D29 dimer system were observed to be around 1700 nm² and 8.2 nm, respectively, and were markedly higher than control group. This increase is attributed to the greater number of atoms and volumetric expansion of system.

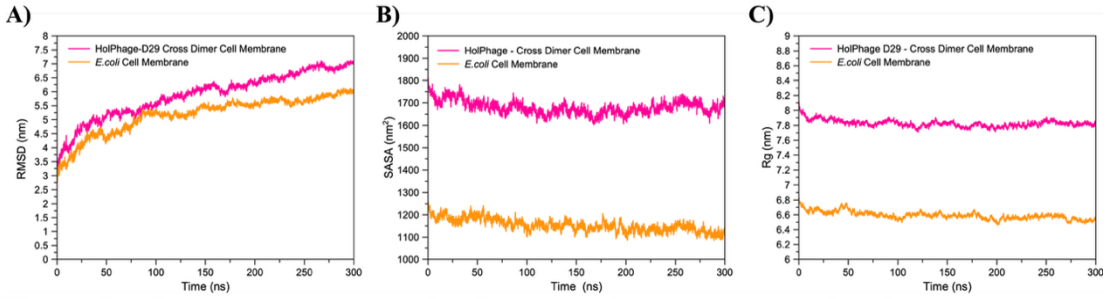


Figure 4.25: Comparison of A) RMSD, B) SASA, and C) Rg analyses between the membrane in the HolPhage-D29 dimer system (pink) and the system containing only the *E. coli* cell membrane (orange).

Conformational change of cross-positioned homodimer form of HolPhage-D29 was observed during 300 ns MD simulation **(Figure 4.26)**. It was observed that C-terminal regions, which were initially located outside the membrane, approache membrane during simulation. It was observed that, starting from 200 ns, C-terminal region interacted more with the membrane. This indicates that the protein had achieved a more stable arrangement along the membrane.

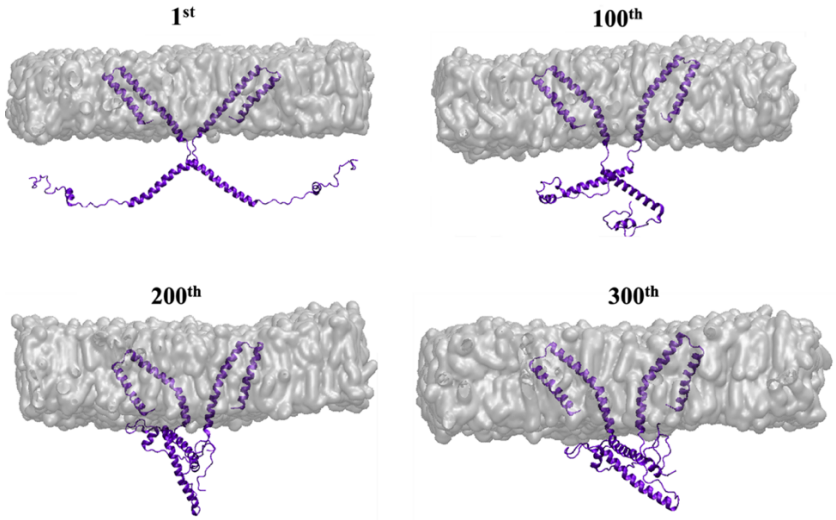


Figure 4.26: Snapshots from 400 ns MD simulation of HolPhage-D29 & *E.coli* dimer cell membrane simulations. Shown respectively at 1st , 100th , 200th, 300th, and 400th ns.

It was observed that the TMD regions of the HolPhage-D29 homodimer bent toward each other throughout the simulation. Structural flexibility that developed over time in the region spanning residues 33–68 was further examined through a detailed bending analysis. As shown in **Figure 4.27**, the analysis revealed that different bending degrees emerged in the TMD segments of chains A and B during the simulation. In chain A, bending angles exceeding 10° (indicated by orange to red regions) were particularly observed after 220 ns at specific positions. In contrast, chain B generally exhibited bending angles in the range of 4–8°.

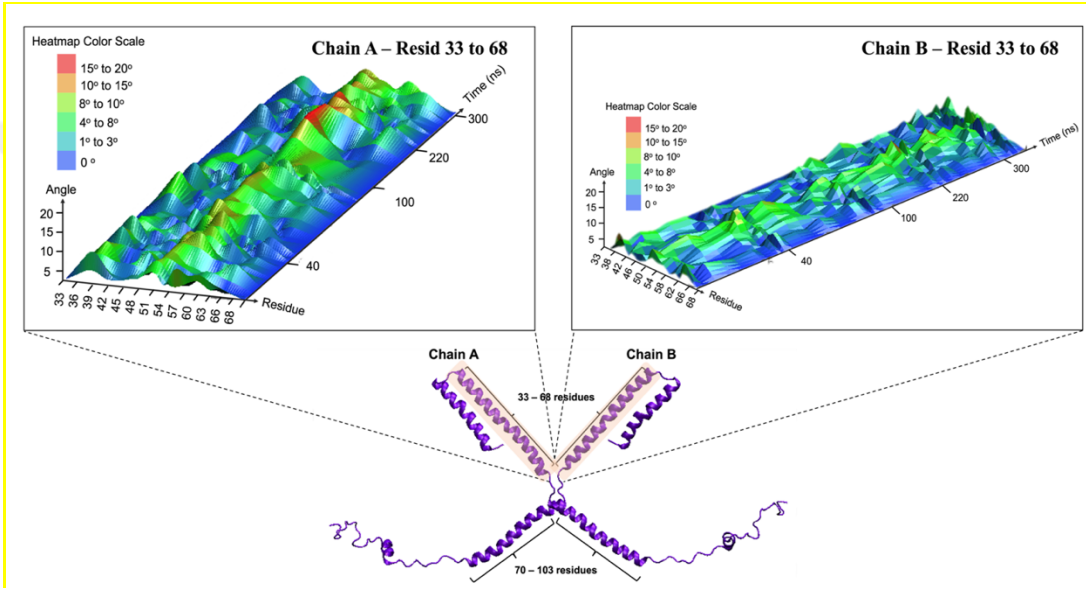


Figure 4.27: Bending analysis of the TMD regions (residues 33–68) of HolPhage-D29 cross homodimer. Top panels show time-resolved bending angles for Chain A (left) and Chain B (right), with color-coded heatmaps indicating angular ranges.

Distance analyses were conducted to investigate the relative motion of the C-terminal regions of monomers in the HolPhage-D29 homodimer, for selected residues (Thr71–Gln100) located on C-terminal of chains A and B , as shown in **Figure 4.28**. Distance profiles between residues exhibited considerable variability. Notably, residues such as Asp75 and Val95 remained relatively stable around ~15 Å, whereas others, including Gln100 and Asp79, showed pronounced fluctuations exceeding 50 Å.

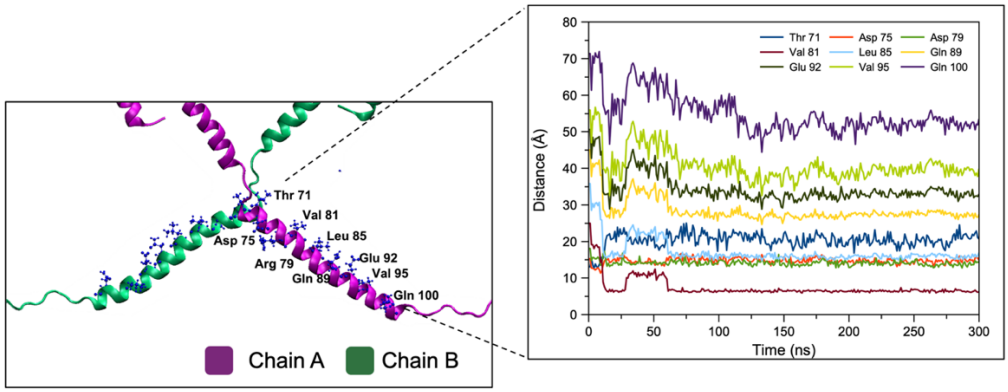


Figure 4.28: Distance analysis of selected residues (Thr71–Gln100) between Chain A and Chain B in the HolPhage-D29 dimer. Left: Structural depiction of interfacial residues. Right: Time-dependent distance profiles showing varying levels of proximity throughout the 300 ns simulation.

Snapshots form different simulation time points were obtained to visualize the dynamic behavior of the HolPhage-D29 dimer within the bacterial membrane **(Figure 4.29)**. At the beginning of simulation, protein complex was positioned nearly parallel to membrane plane. As the simulation progressed, noticeable conformational changes were observed in both chains, particularly characterized by the inward bending of the C-terminal regions toward each other. These structural rearrangements are consistent with the findings from the bending and distance analyses.

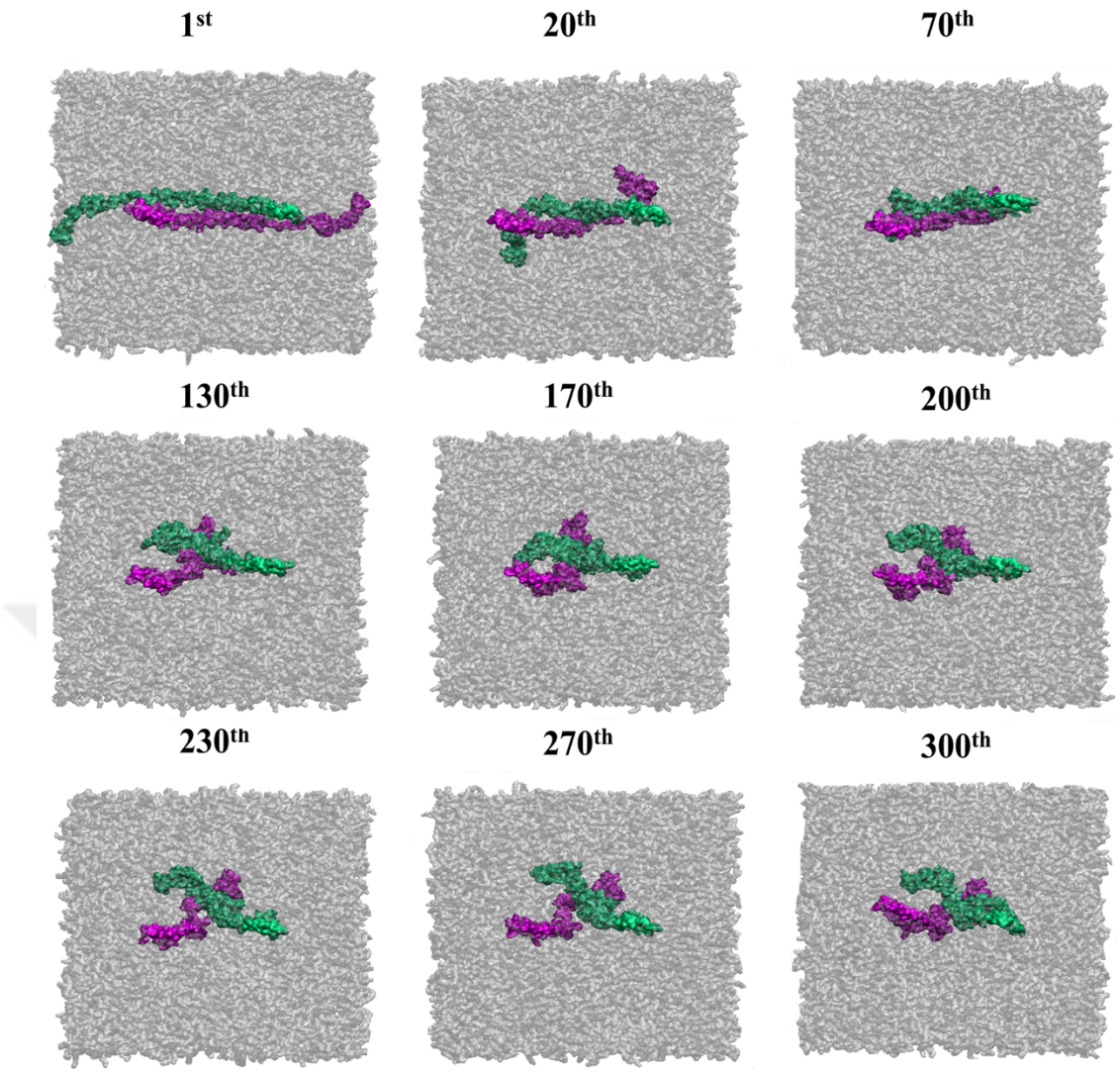


Figure 4.29: Time-lapse snapshots of HolPhage-D29 homodimer embedded in lipid bilayer, shown at selected time points (1–300 ns). Chain A and Chain B are colored in magenta and green, respectively.

Membrane thickness analysis of the *E. coli* cell membrane and the HolPhage-D29 cross dimer-containing system is presented in **Figure 4.30**. Heatmaps **(Figure 4.30 - A and B)** illustrate the spatial distribution of membrane thickness for both systems, while the time series plot **(Figure 4.30 - C)** shows the comparison of average thickness values. The average thickness of the *E. coli* control membrane was calculated as 37.915 ± 0.513 Å, whereas in the system containing the HolPhage-D29 cross dimer, this value was slightly lower at 37.403 ± 0.484 Å. Overall membrane integrity was preserved in both systems. However, the presence of the D-29 dimer led to localized thinning and increased heterogeneity in membrane thickness.

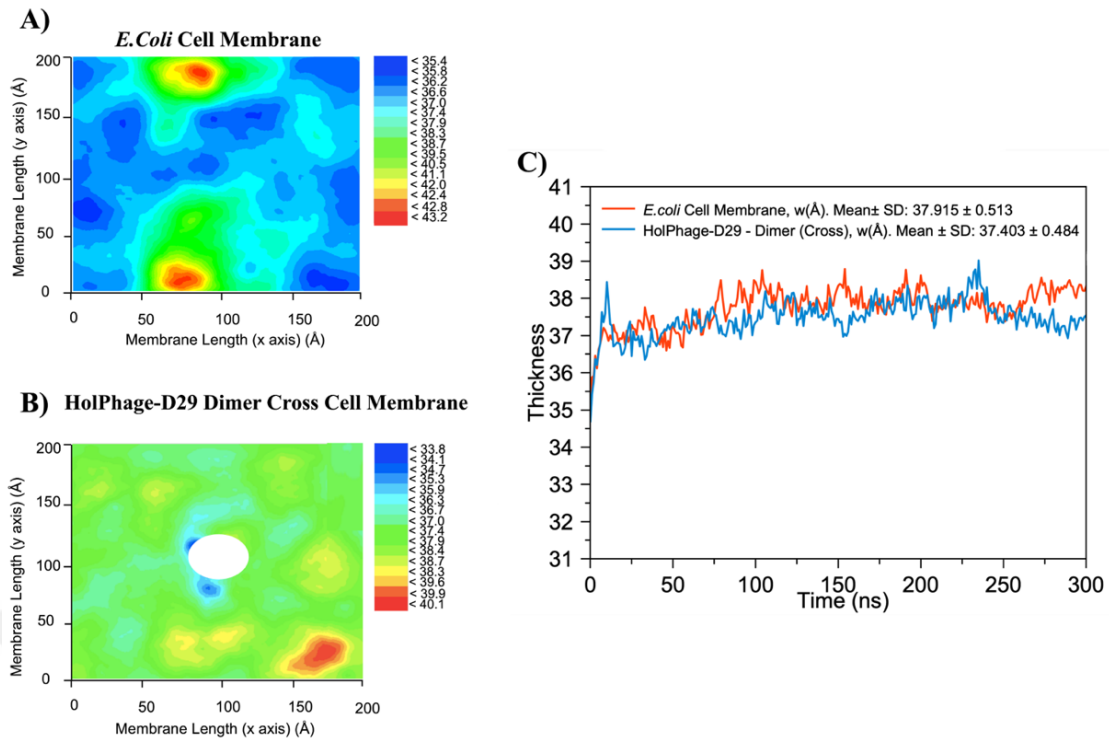


Figure 4.30: A) Membrane thickness heatmap of the *E. coli* cell membrane alone, B) Heatmap of the membrane containing the HolPhage-D29 cross dimer, C) Time-dependent comparison of average membrane thickness values between the two systems.

Leaflet overlap analysis revealed that both the width of the overlap region (0.652 ± 0.09 nm) and the fraction of mass overlap (0.332 ± 0.044) were higher in the HolPhage- D29 dimer-containing system compared to the *E. coli* control membrane. In contrast, the fraction of atoms in contact with the opposite leaflet remained at similar levels in both systems (~0.042).

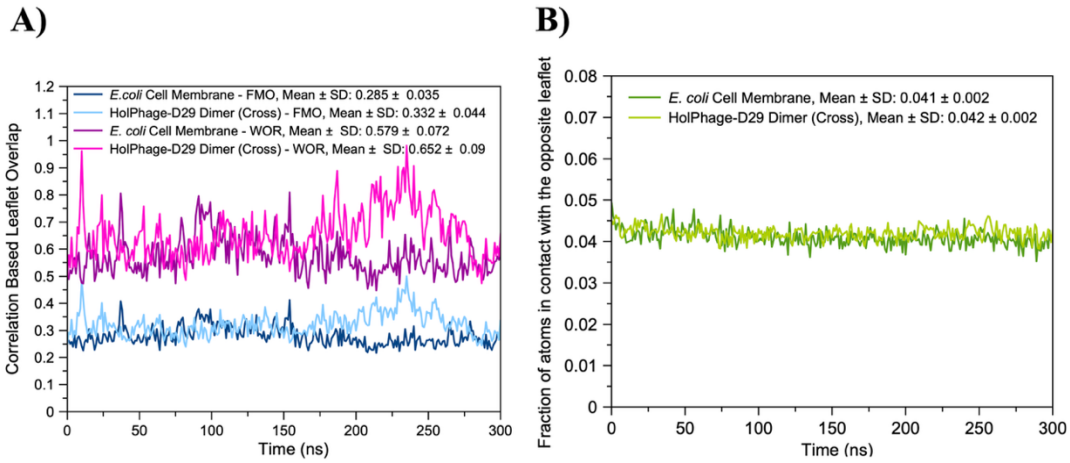


Figure 4.31: A) Change in overlap width and mass fraction values of *E. coli* membrane (blue) and HolPhage-D29 dimer-containing membrane (purple) over time in correlation-based leaflet overlap analysis, B) Comparison of the atom ratio in contact with the opposite leaflet over time between the two systems.

4.3.4. *E.coli* Cell Membrane & HolPhage-D29 Tetramer MD Simulations

Structural analysis results of the tetrameric form of HolPhage-D29, constructed by side-by-side arrangement of monomers, are presented in **Figure 4.32**. RMSD values **(Figure 4.32 - A)** stabilized around ~1.8–2.0 nm after the first 50 ns, indicating that the structure remained conformationally stable throughout the simulation. SASA analysis **(Figure 4.32 - B)** showed a gradual decrease from approximately 400 nm² to 330 nm², suggesting a reduction in the solvent-accessible surface area and an increase in structural compactness. Similarly, Rg values **(Figure 4.32 - C)** decreased from ~5.5 nm to ~4.5 nm over the course of the simulation, further supporting the compaction of the structure. These findings indicate that the tetrameric assembly gradually adopted a more compact conformation over time.

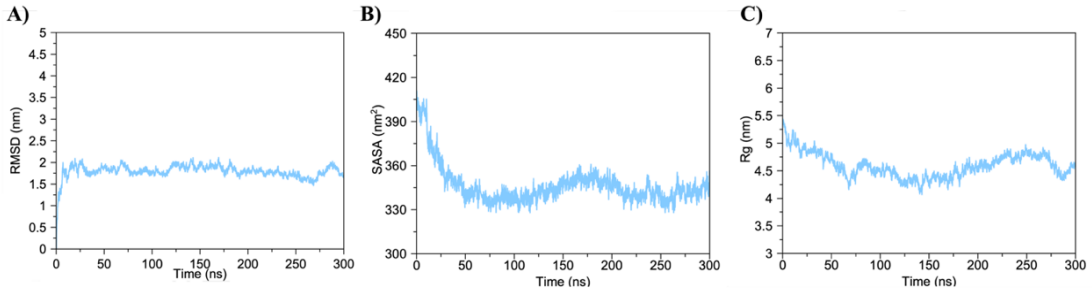


Figure 4.32: MD simulation of HolPhage-D29 tetramer with time-dependent A) RMSD, B) SASA and C) Rg analyses.

RMSD, SASA, and Rg data of membrane in HolPhage-D29 tetramer system and control *E. coli* cell membrane are compared in **Figure 4.33**. RMSD analysis **(Figure 4.33 - A)** indicates that both membrane systems maintained a stable conformation during the simulation. SASA values **(Figure 4.33 - B)** ranged between ~1600–1700 nm² in tetramer system, which is significantly higher than those observed in the control membrane. Similarly, Rg analysis **(Figure 4.33 - C)** showed higher values for HolPhage-D29-containing system (~7.4–7.8 nm). This increase is attributed to the greater volumetric expansion and higher atom count of the *E. coli* membrane system containing the tetramer.

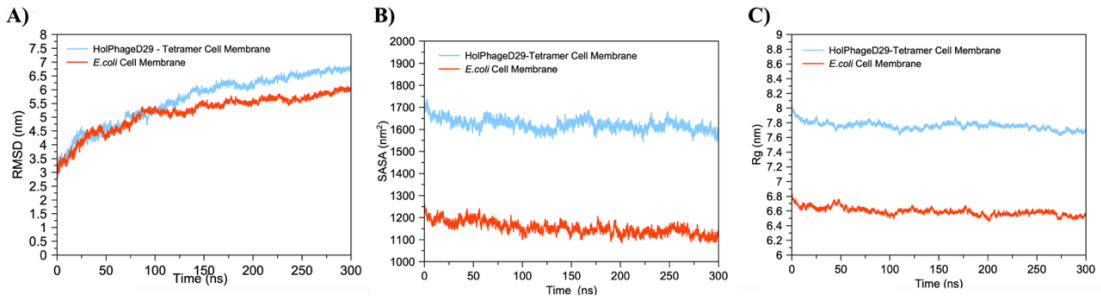


Figure 4.33: Comparison of A) RMSD, B) SASA, and C) Rg analyses between the membrane in the HolPhage-D29 tetramer system (light blue) and the system containing only the *E. coli* cell membrane (orange).

Figure 4.34 presents the trajectory analysis data of the HolPhage-D29 tetramer. At the beginning of the simulation, the protein complex was positioned perpendicularly and symmetrically within the membrane plane. Starting from approximately 100 ns, noticeable bending and outward orientation were observed in the C-terminal regions of each monomer within the homo-tetrameric structure.

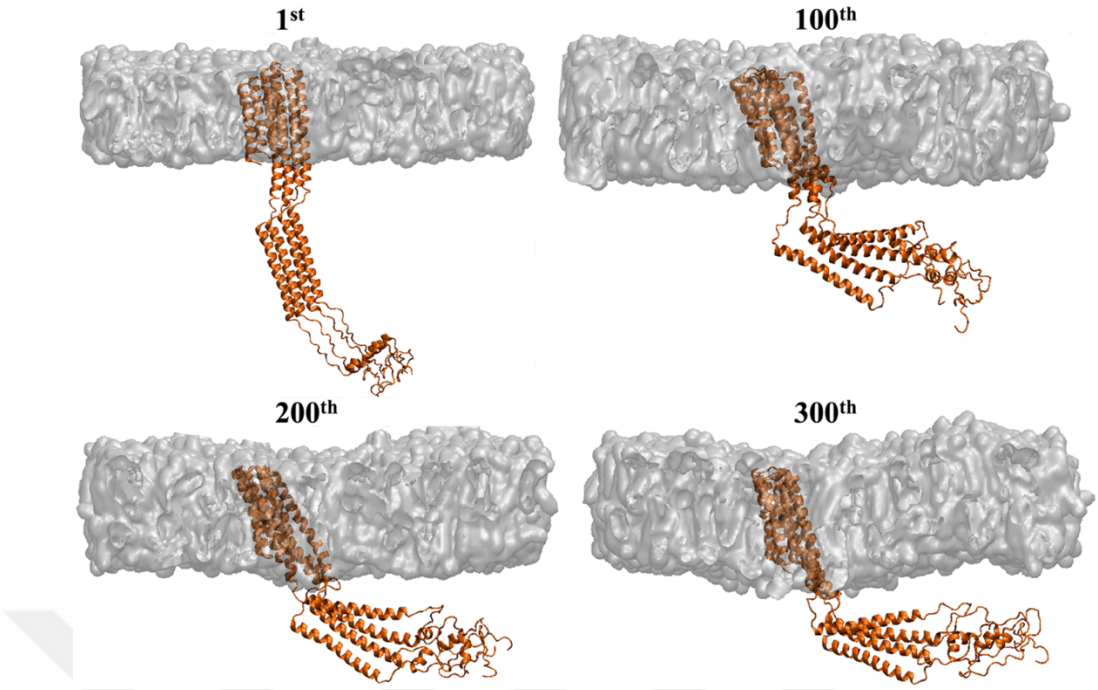


Figure 4.34: Snapshots from 400 ns MD simulation of HolPhage-D29 & *E.coli* tetramer cell membrane simulations. Shown respectively at 1st , 100th , 200th, 300th, and 400th ns.

Figure 4.35 presents the curvature analysis of three distinct regions of the HolPhage-D29 tetramer structure (residues 30–66, 72–103, and 105–134). In the first region, corresponding to TMD (residues 30–66), curvature values remained consistently low. This indicating that membrane-embedded orientation was largely maintained. In the second region (residues 72–103), a slight increase in curvature was observed over time. Overall structural integrity of this segment was preserved. The most pronounced conformational changes were detected in C-terminal region (residues 105–134), where curvature values showed a marked increase throughout the simulation.

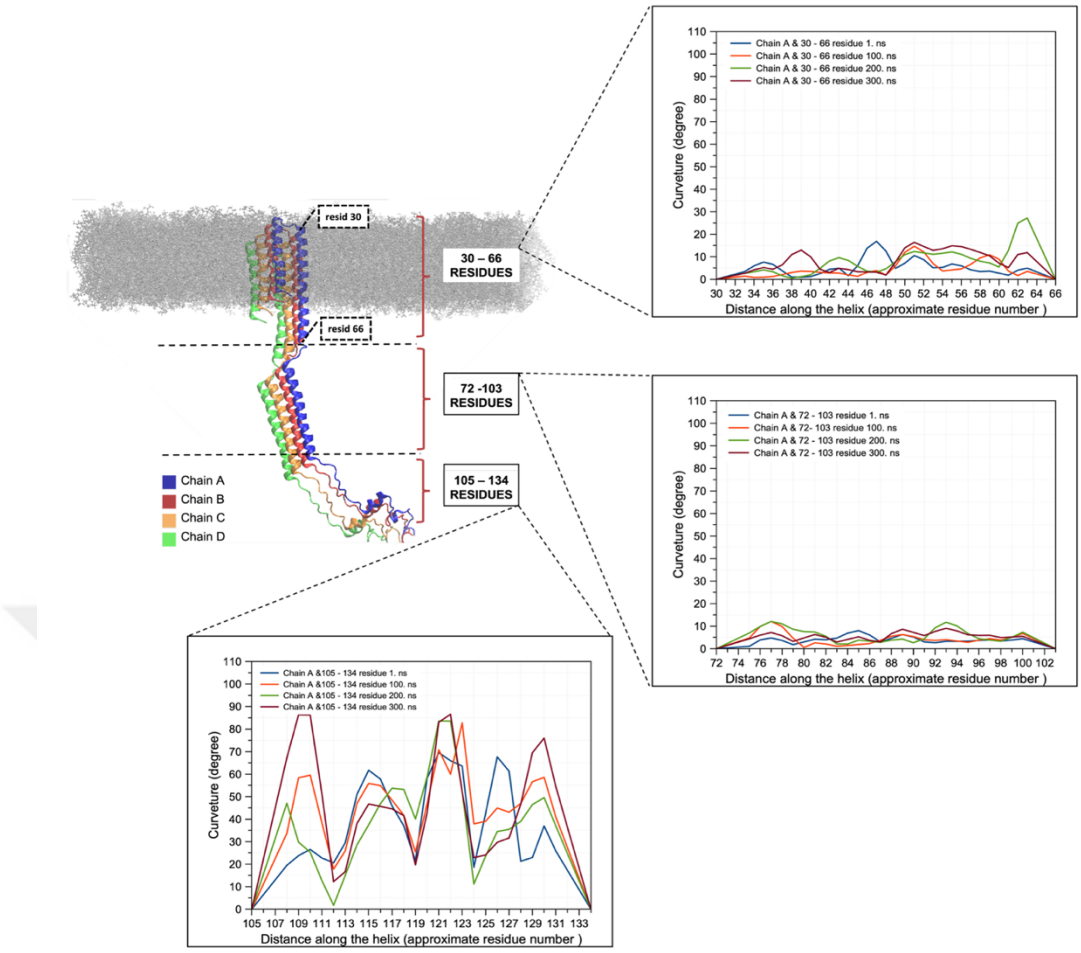


Figure 4.35: Curvature analysis of three distinct regions (residues 30–66, 72–103, and 105–134) of the HolPhage-D29 tetramer. Graphs show changes in curvature over the course of MD simulation at different time points.

These findings are consistent with the previously described trajectory analysis. In the trajectory images, noticeable bending and outward orientation of the C-terminal extensions were clearly observed, particularly after 100 ns. The curvature analysis quantitatively supports the bending behavior observed in the C-terminal domain.

Cell membrane thickness analysis of the *E. coli* control membrane and HolPhage-D29 tetramer membrane is presented in **Figure 4.36**. Heatmaps **(Figure 4.36 - A and B)** illustrate spatial distribution of membrane thickness. Time-dependent thickness graph **(Figure 4.36 - C)** indicates that overall membrane integrity was maintained in both systems. HolPhage-D29 tetramer system was calculated to be approximately 0.51 Å thinner than the *E. coli* membrane. Although the presence of the tetramer caused local thinning in certain regions of the membrane, it did not cause any disruption in the overall membrane structure.

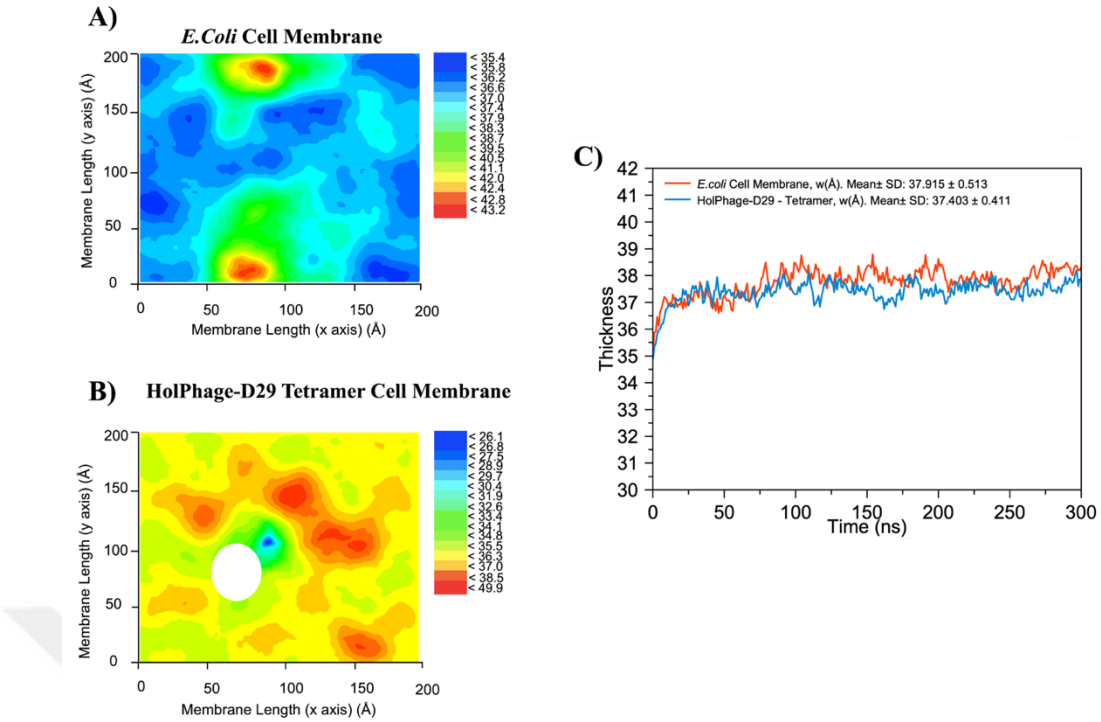


Figure 4.36: A) Membrane thickness heatmap of the *E. coli* cell membrane alone, B) Heatmap of the membrane containing the HolPhage-D29 tetramer, C) Time-dependent comparison of average membrane thickness values between the two systems.

WOR (0.718 ± 0.07 nm) and FMO (0.312 ± 0.032) calculated for the HolPhage-D29 tetramer-containing membrane were observed to be higher compared to the control membrane in the analysis presented in **Figure 4.37**. This indicates increased physical proximity between the leaflets. Fraction of atoms in contact with the opposite leaflet remained at similar levels in both systems (~0.042). These findings support the local thinning observed in the membrane thickness analysis.

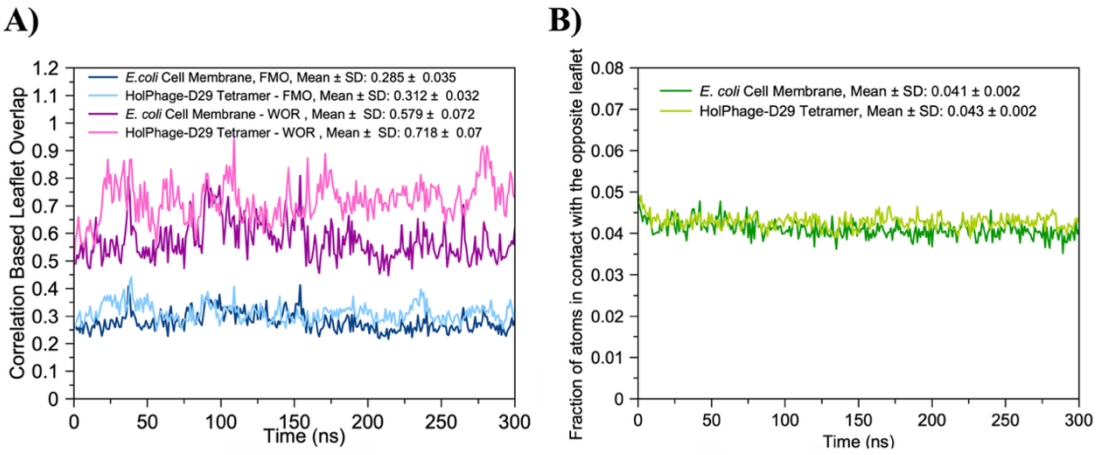


Figure 4.37: A) Change in overlap width and mass fraction values of *E. coli* membrane (blue) and HolPhage-D29 tetramer-containing membrane (purple) over time in correlation-based leaflet overlap analysis, B) Comparison of the atom ratio in contact with the opposite leaflet over time between the two systems.

4.3.5 *E.coli* Cell Membrane & HolPhage-D29 C-terminal MD Simulations

To evaluate the structural effects of the C-terminal region of the D29 phage holin on the *E. coli* inner membrane, the amino acid sequence of this region was modeled as a separate peptide. The peptide was positioned near the cytoplasmic side of the membrane, without making direct contact. 300 ns MD simulation was conducted for this system. Structural analyses obtained from the MD trajectory are presented in **Figure 4.38**. The RMSD values **(Figure 4.38 - A)** stabilized around ~2.4 nm, indicating conformational equilibration. SASA **(Figure 4.38 - B)** gradually decreased from ~80 nm² to ~65 nm², suggesting structural folding or compaction. Supporting the SASA results, the Rg, **(Figure 4.38 - C)** also decreased from ~3.2 nm to ~2.0 nm, indicating a compaction of the structure over time. These findings point to a folding behavior in the peptide near the membrane.

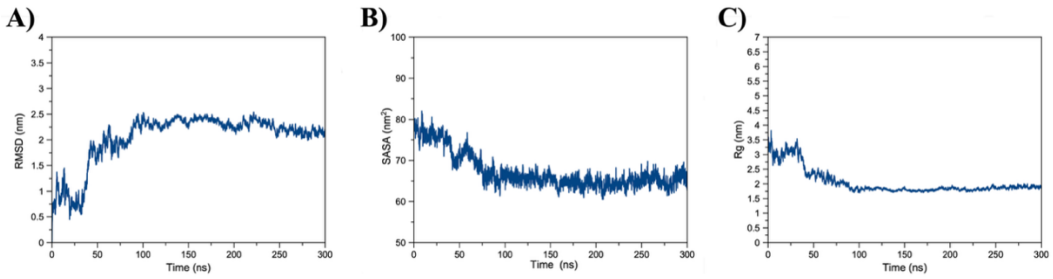


Figure 4.38: MD simulation of HolPhage-D29 C-terminal system with time-dependent A) RMSD, B) SASA and C) Rg analyses.

Figure 4.39 presents the comparative structural analyses of the HolPhage-D29 C-terminal membrane system and the *E. coli* cell membrane. RMSD values were found to be lower in the HolPhage-D29 C-terminal system **(Figure 4.39 - A)**. In SASA analysis, both systems exhibited a similar decreasing trend, although values remained slightly higher in the HolPhage-D29 C-terminal system **(Figure 4.39 - B)**. Rg showed comparable levels in both systems throughout the simulation **(Figure 4.39 - C)**.

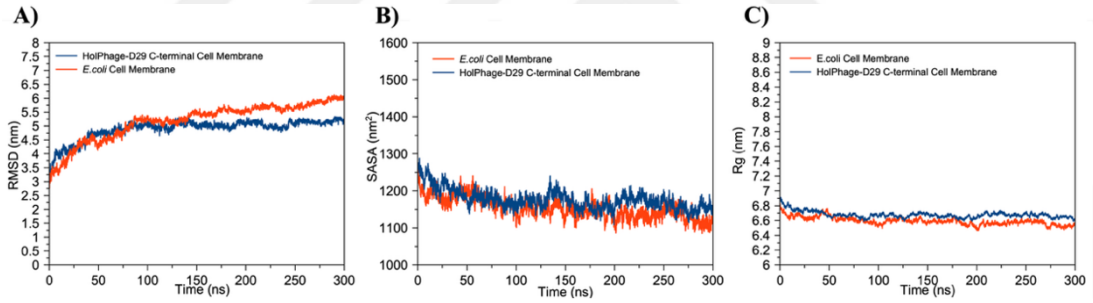


Figure 4.39: Comparison of A) RMSD, B) SASA, and C) Rg analyses between the membrane in the HolPhage-D29 C-terminal system (light blue) and the system containing only the *E. coli* cell membrane (orange).

Structural snapshots from different time points of the simulation are presented in **Figure 4.40**. Initially, the HolPhage-D29 C-terminal peptide was positioned near the cell membrane without direct contact. As the simulation progressed (100–300 ns), the peptide was observed to interact with the membrane surface and reorient itself parallel to the membrane plane.

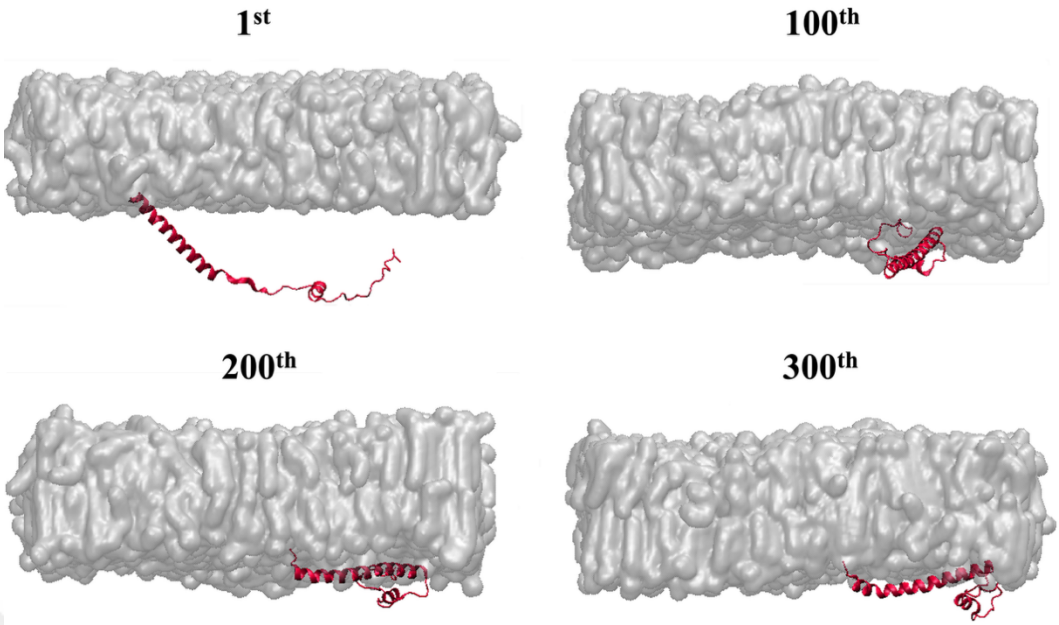


Figure 4.40: Snapshots from 400 ns MD simulation of HolPhage-D29 & *E.coli* tetramer cell membrane simulations. Shown respectively at 1st , 100th , 200th, 300th, and 400th ns.

Figure 4.41 presents the thickness analyses of the *E. coli* cell membrane and the membrane containing the HolPhage-D29 C-terminal peptide. According to the heat maps **(Figure 4.41 - A and B)**, more pronounced thinning was observed in certain regions of the peptide-containing membrane system. The time-dependent thickness plot **(Figure 4.41 - C)** showed that both systems exhibited similar average thickness profiles. The membrane containing the HolPhage-D29 C-terminal peptide was approximately 0.43 Å thinner than the control system.

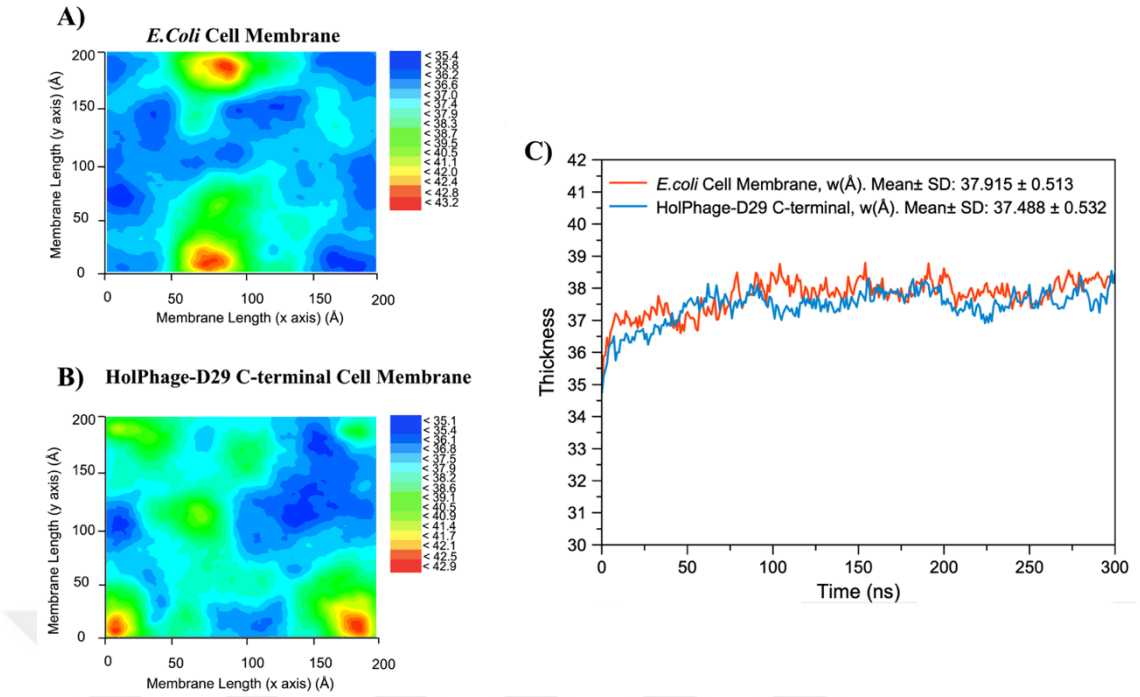


Figure 4.41: A) Membrane thickness heatmap of the *E. coli* cell membrane alone, B) Heatmap of the membrane containing the HolPhage-D29 C-terminal membrane, C) Time-dependent comparison of average membrane thickness values between the two systems.

In **Figure 4.42** inter-leaflet overlap and contact analyses are given. Ratio of atoms in contact with the opposite leaflet remained at similar levels in both systems and was calculated as an average of ~0.041 ± 0.002 **(Figure 4.42 - A)**. According to the correlation-based overlap analysis **(Figure 4.42 - B)**, WOR values were observed at similar levels in the HolPhage-D29 C-terminal containing system to the control system (~0.565 vs. ~0.579). FMO remained at the same level in both systems. No significant difference was observed between the values.

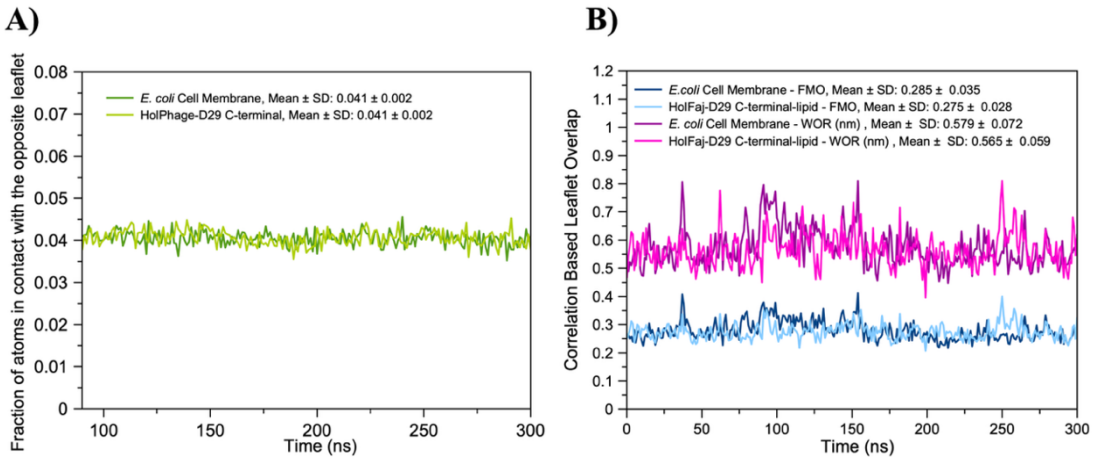


Figure 4.42: A) Change in overlap width and mass fraction values of *E. coli* membrane (blue) and HolPhage-D29 C-terminal-containing membrane (purple) over time in correlation-based leaflet overlap analysis, B) Comparison of the atom ratio in contact with the opposite leaflet over time between the two systems.

4.3.6. *S.Aureus* Cell Membrane Modeling And MD Simulations

Cell membrane structure of *S. aureus* was modeled and subjected to a 400 ns MD simulation. RMSD, SASA, and Rg values obtained from the simulation are presented in **Figure 4.43**. Analyses indicated that *S.aureus* membrane model exhibited a certain conformational stability during the simulation. Increase observed in RMSD graph suggests that the system underwent structural rearrangement and reached a more stable state after approximately 200 ns. A slight decrease in solvent-accessible surface area was observed. Constant Rg value indicates that structural integrity of system was maintained.

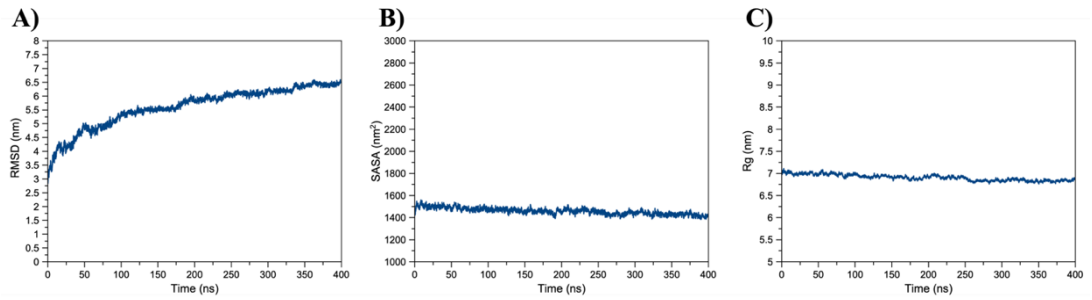


Figure 4.43: Results of A) RMSD, B) SASA, and C) Rg analyses throughout the 400 ns MD simulation.

Figure 4.44 presents the morphological changes experienced by the model membrane over a 400 ns simulation period. Membrane surface appeared relatively smooth and homogeneous at the beginning of the simulation. After 200 ns, pronounced undulations, curvatures, and surface irregularities emerged. This indicates that lipids reorganized and repositioned over time. These changes, which occurred in the absence of any protein influence, are likely attributed to high potential of membrane constituents such as cardiolipin to induce micro-fluctuations and curvature. These findings suggest that membrane topology can undergo substantial alterations over time.

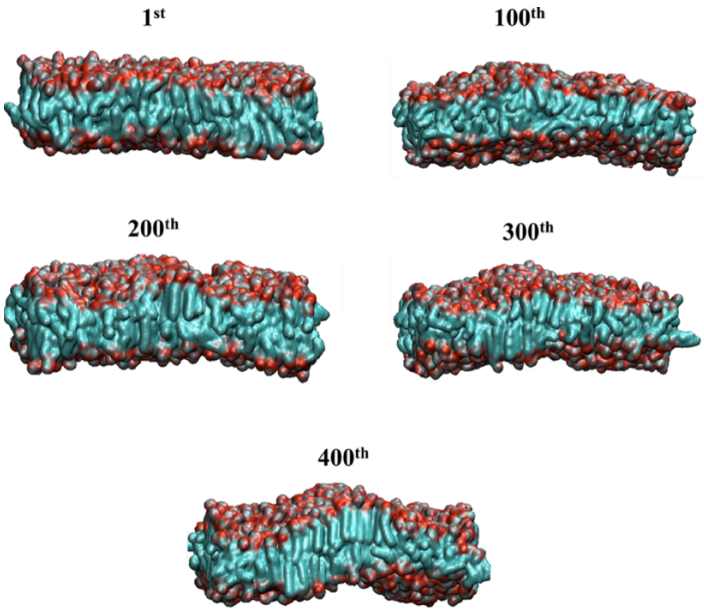


Figure 4.44: Snapshots from 400 ns MD simulation of *S. aureus* cell membrane simulations. Shown respectively at 1st, 100th, 200th, 300th, and 400th ns.

4.3.7. *S.aureus* Cell Membrane & HolPhage-K MD Simulations

Results of HolPhage-K MD simulation are presented in Figure 4.45. Protein exhibited structural fluctuations inthe range of 1.0–2.0 nm during first 100 ns of simulation in RMSD plot **(Figure 4.45 - A)**. A noticeable increase was observed after approximately 350 ns, indicating a structural rearrangement of protein. SASA values remained stable within the range of 145–165 nm² during the simulation **(Figure 4.45 - B)**. Rg values gradually decreased to 4.5–5.5 nm over time **(Figure 4.45 - C)**. These results are suggesting that protein adopted a more compact conformation.

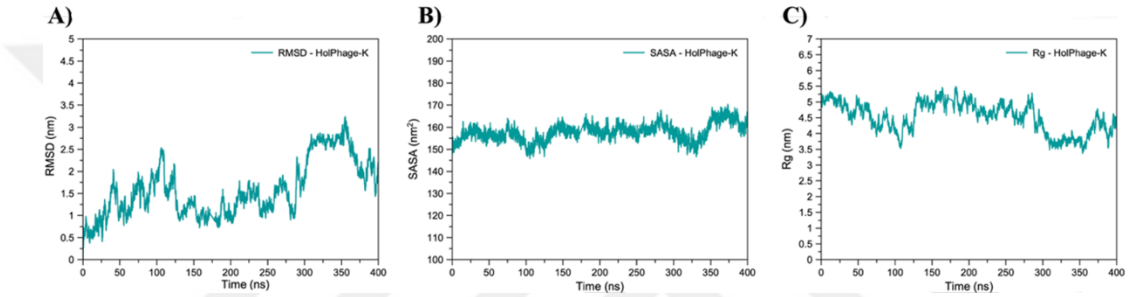


Figure 4.45: A) RMSD, B) SASA, and C) Rg values of HolPhage-K protein during the 400 ns MD simulation.

Figure 4.46 presents the trajectory analysis results of the HolPhage-K 400 ns MD simulation. Evaluation of the analysis results revealed that while TMDs of the protein preserved its structural integrity during the simulation, helices located at the C-terminal end underwent a pronounced conformational rearrangement. This region, which initially adopted an α-helical conformation, gradually transitioned into a coil structure over time. Additionally, bendix analysis in **Figure 4.47** quantitatively demonstrates this structural changes. Analysis clearly indicates an increased tendency for curvature, particularly in the helical segment of the C-terminal region.

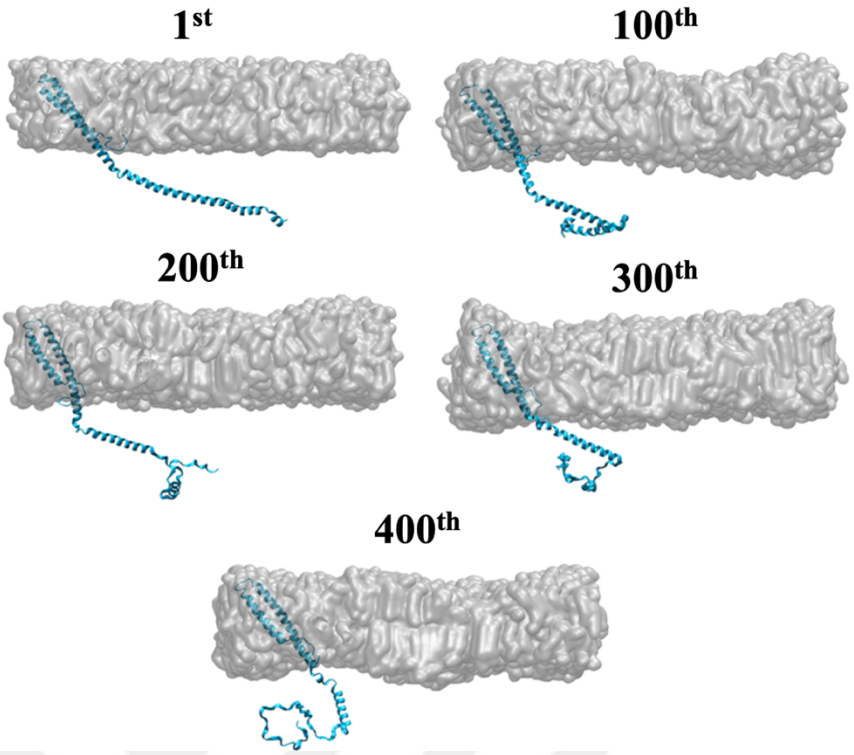


Figure 4.46: Snapshots obtained from MD simulations of HolPhage-K at the 1 st, 100th, 200th, 300th, and 400th ns.

Throughout the simulation, an increase in the flexibility of both the N-terminal (blue) and C-terminal (red) domains was observed. When the structures at 300 ns, 350 ns, and 400 ns are compared, it is evident that C-terminal segment progressively expanded and unfolded over a larger area. At around 300 ns, the C-terminal region appeared to be in close proximity and interacting with N-terminal. This interaction gradually weakened over time.

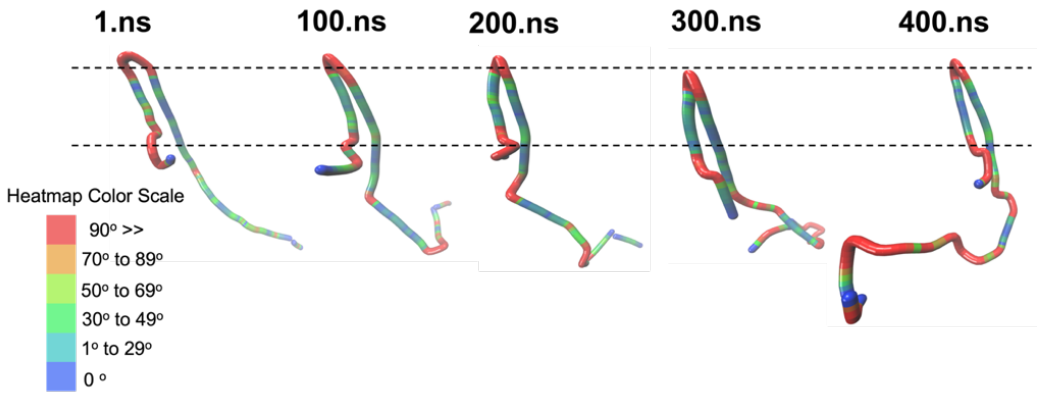


Figure 4.47:Bending angle values taken from the HolPhage-K MD simulation at the beginning, 100th, 200th, 300th, and 400th respectively. (Bending angle increases from blue to red).

RMSD, SASA, and Rg analyses were performed to evaluate the effect of the holin protein on the *S. aureus* cell membrane structure on two different systems: containing the protein (HolPhage-K & *S.aureus* Cell Memrane MD Simulations) and one without (*S.aureus* Cell Membrane MD Simulations). According to RMSD analysis **(Figure 4.48 - A)**, control membrane composed solely of lipid components exhibited lower deviations in the range of approximately 6.0–7.0 nm, whereas HolPhage-K system showed higher deviations, reaching up to 7.0–8.0 nm. This means that there is more conformational change in the presence of holin. The findings suggested that the presence of HolPhage-K increases the structural flexibility and disorder of the membrane. System with holin protein maintained SASA values around 2200 nm², while the control membrane remained near 1500 nm² **(Figure 4.48 - B)**. This increase reflected the conformational changes induced by HolPhage-K on the membrane. According the Rg graph **(Figure 4.48 - C)**, higher values were observed in holin-containing system, approximately within the 8.5–9.0 nm range. This observation suggested that the presence of the protein disrupts the membrane plane, leading to greater structural expansion.

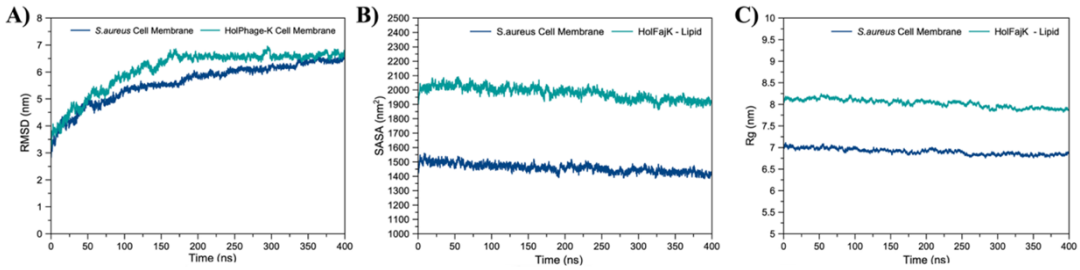


Figure 4.48: Comperative results of A) RMSD, B) SASA, and C) Rg analyses throughout the 400 ns *S.aureus* Cell Membrane MD simulation and HolPhage-K simulation.

Figure 4.49 presents membrane thickness variation analyses for *S. aureus* cell membrane in both simulation systems. The regional thickness maps illustrate topological differences across membrane surface. **Figure 4.49 - B** depicts the localized membrane thickness in HolPhage-K system. White circle indicates the position of protein on membrane. A significant thinning of membrane is observed in vicinity of this region. These map data reveal localized weakening of the membrane structure surrounding protein. **Figure 4.49 - C** compares the average membrane thickness values between protein-containing and protein-free systems. Control system is approximately 0.64 Å thicker than system containing holin protein. Although both systems showed an overall trend of increasing thickness over time, the membrane in the holin-containing system remained consistently thinner, suggesting that the protein causes structural changes in the membrane.

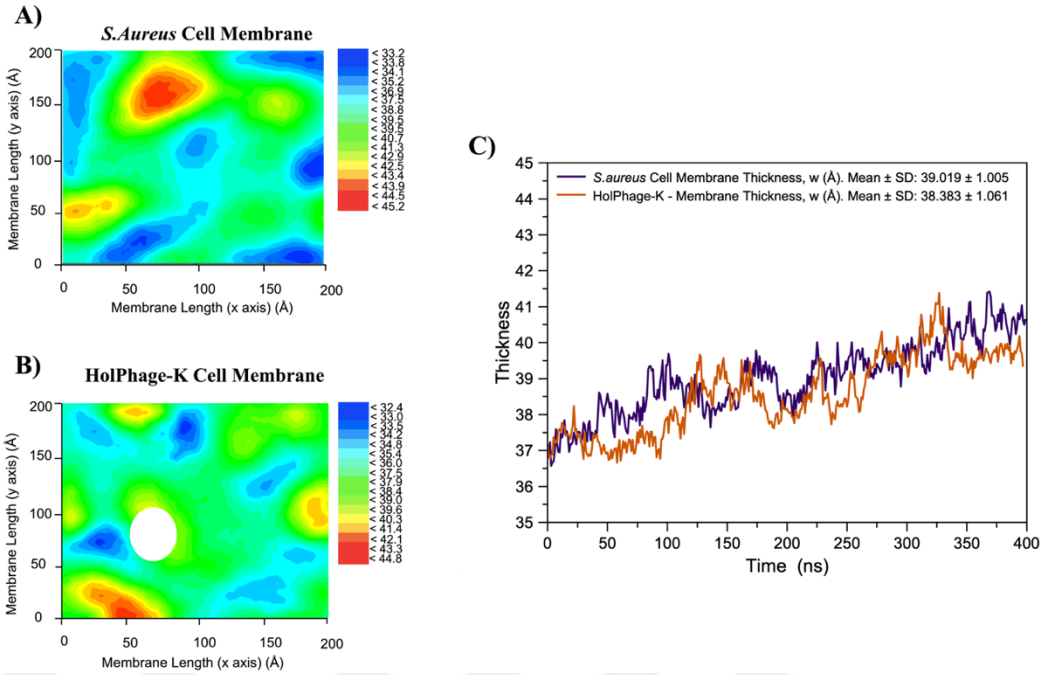


Figure 4.49:A) Membrane thickness heatmaps and time-dependent thickness plots, B) HolPhage-K containing membrane system, According to the color scale, blue tones represent thinner areas of membrane, whereas red tones indicate thicker regions. C) Average membrane thickness values measured over 400 ns for both systems.

Three different structural analyses were conducted to analyze how the membrane structure is affected by the presence of holin protein. In the correlation-based leaflet overlap analysis **(Figure 51 - A)**, an increase was observed in both the width of overlapping regions and the fractional mass ratio in the HolPhage-K system. Similarly, a slight increase in proportion of atoms in contact with the opposite leaflet was also detected in protein-containing system. These findings indicate a reduction in separation between lipid layers and suggest membrane thinning. Membrane thickness measurements support this conclusion, with average thickness measured as 38.38 Å in HolPhage-K system. This result implies that the membrane becomes thinner in presence of holin. Integration of HolPhage-K into the *S. aureus* cell membrane shown to impact the physical organization of the membrane.

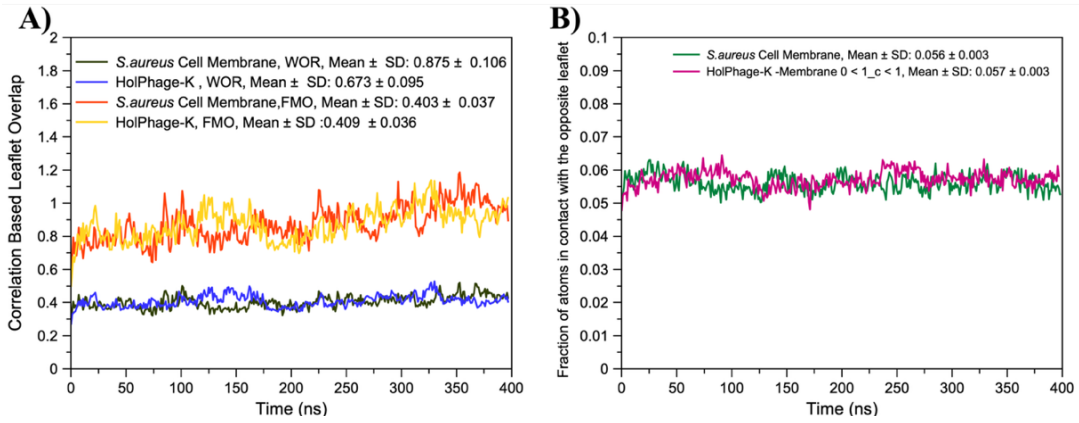


Figure 4.50: A) Leaflet overlap and contact analyses, the width of the overlapping region and mass fraction overlap were compared over time between the *S. aureus* and HolPhage-K containing systems. B) The fraction of atoms in contact with the opposite leaflet was evaluated for both systems over 400 ns.

4.3.8 *S. aureus* Cell Membrane & HolPhage-K Dimer MD Simulations

As a result of HolPhage-K MD simulation, it was observed that insertion of a single holin molecule into *S. aureus* cell membrane influenced membrane permeability. In the literature, it has been frequently reported that holin proteins typically form pores in cellular membranes in multimeric or oligomeric forms **[175], [176], [177]**.

Dimer model of HolPhage-K was constructed by aligning two monomers in a parallel and symmetric orientation. This approach was employed to test the hypothesis that holins may cluster on membrane surface to gain functional activity. RMSD, SASA, and Rg analyses obtained from the MD simulation are presented in **Figure 4.51**. Graphs demonstrate that HolPhage-K dimer structure maintained a certain degree of stability throughout the simulation. RMSD analysis indicates fluctuations within the range of 2.0–3.0 nm beginning from approximately 50 ns of the simulation. SASA values remained within the range of 280–310 nm² over 300 ns simulation period, with no significant variations observed in solvent accessibility. Examination of Rg results shows fluctuations between 4.8–5.4 nm, indicating that dimer structure preserved its overall globular form during the simulation.

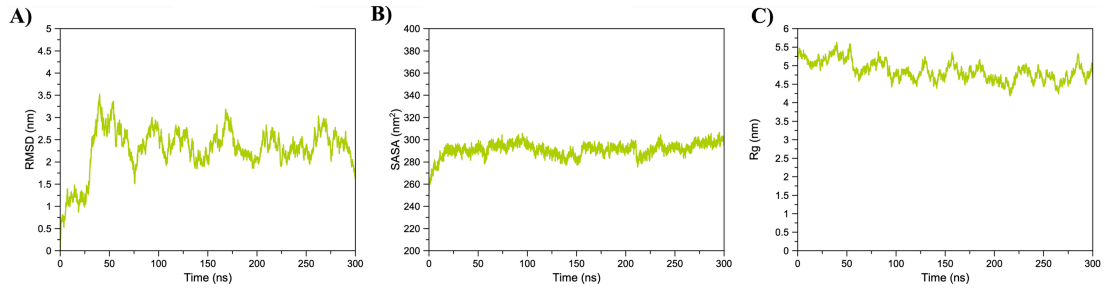


Figure 4.51: A) RMSD, B) SASA ve C) Rg analysis results obtained from the 300 ns MD simulation of the HolPhage-K dimer.

RMSD, SASA, and Rg values of the membrane containing the protein were compared to those of control membrane. Examination of RMSD values revealed that membrane structure in both systems reached a relatively stable structure, particularly after 250 ns. Presence of a larger number of atoms in dimer-containing system contributes to elevated values in parameters such as SASA and Rg. Therefore, increases that SASA and Rg graph are attributed to the initial physical dimensions of system **(Figure 4.52)**.

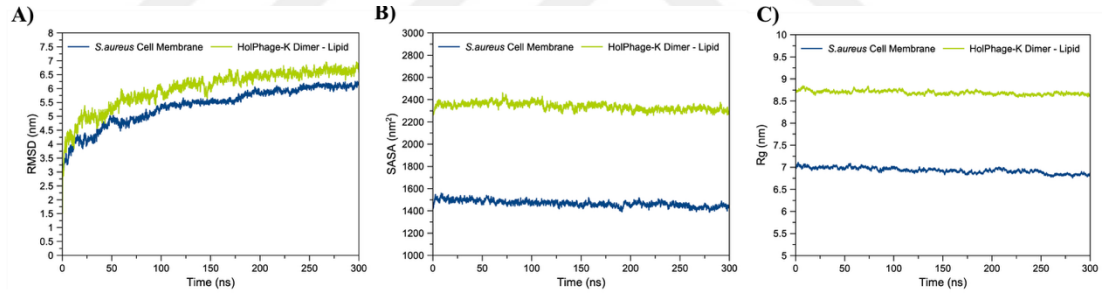


Figure 4.52: Comparative A) RMSD, B) SASA, and C) Rg analyses for system containing the *S. aureus* cell membrane and HolPhage-K dimer.

Trajectory data obtained from 300 ns MD simulation were analyzed. It was observed that HolPhage-K dimer became increasingly integrated into membrane over time. C-terminal region appeared to become more flexible and spread across the membrane surface.

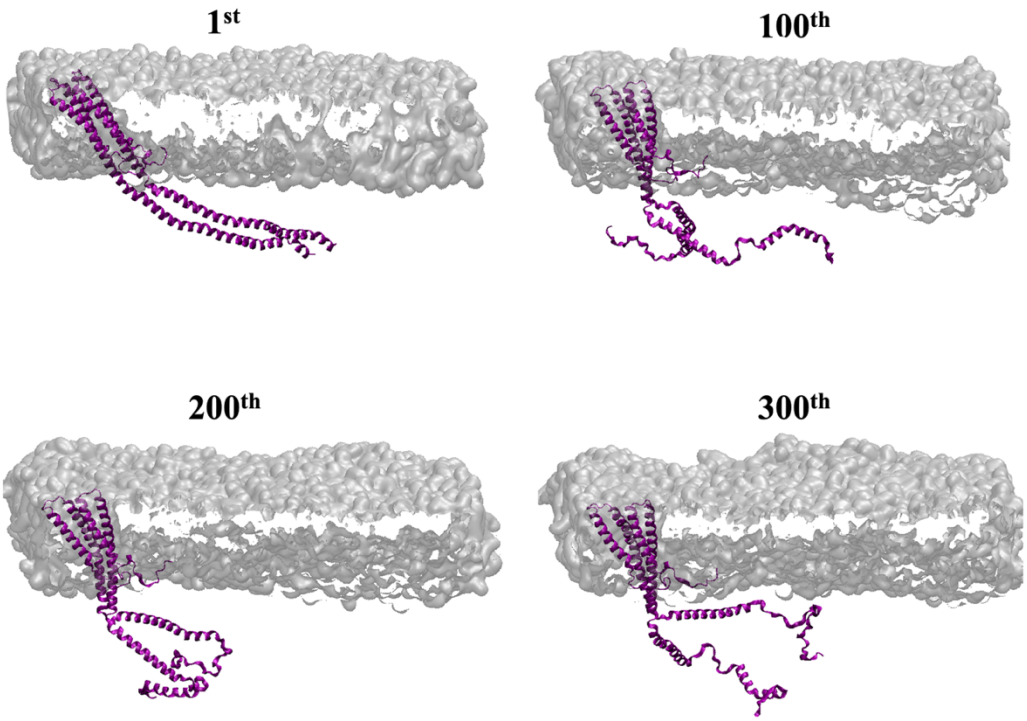


Figure 4.53: Snapshots obtained from MD simulations of HolPhage-K dimer at the 1 st, 100 th, 200th, 300th ns.

Figure 4.54 illustrate that both Chain A and Chain B underwent notable conformational changes during their interaction with membrane. At the beginning of the simulation, C-terminal regions of both monomers were aligned parallel to membrane surface. Over time, these regions moved closer to membrane, promoting the embedding of TMDs into the bilayer.

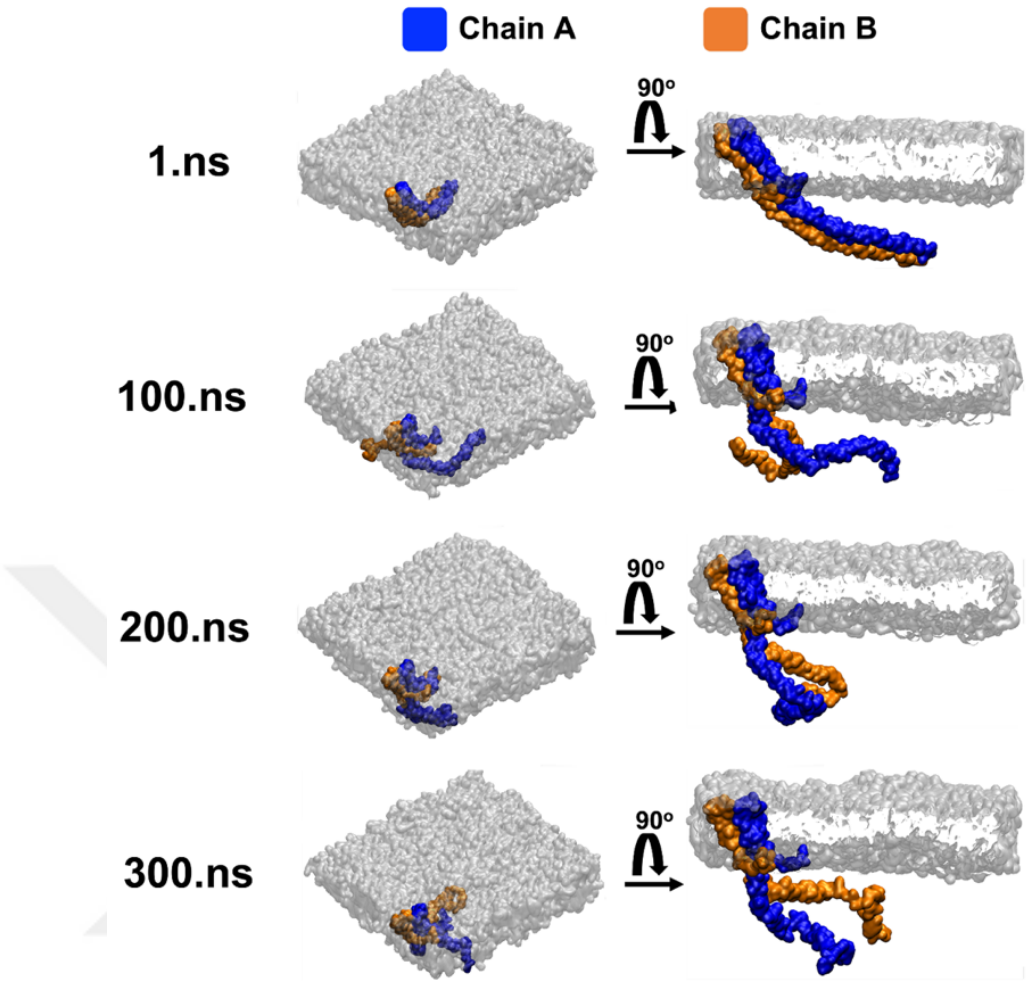


Figure 4.54: Relative positions of the monomers forming the HolPhage-K dimer throughout the simulation - Chain A (blue) and Chain B (orange). Snapshots taken at 1st ns, 100th ns, 200th ns, and 300th ns are shown sequentially.

Secondary structure analysis was performed to analyze the behavior of the C-terminal region throughout the simulation **(Figure 4.55)**. Helical backbone of HolPhage-K dimer remained generally stable during the simulations. Secondary structure disruptions were observed particularly in the C-terminal regions. Over time, coil structures emerged in these C-terminal segments.

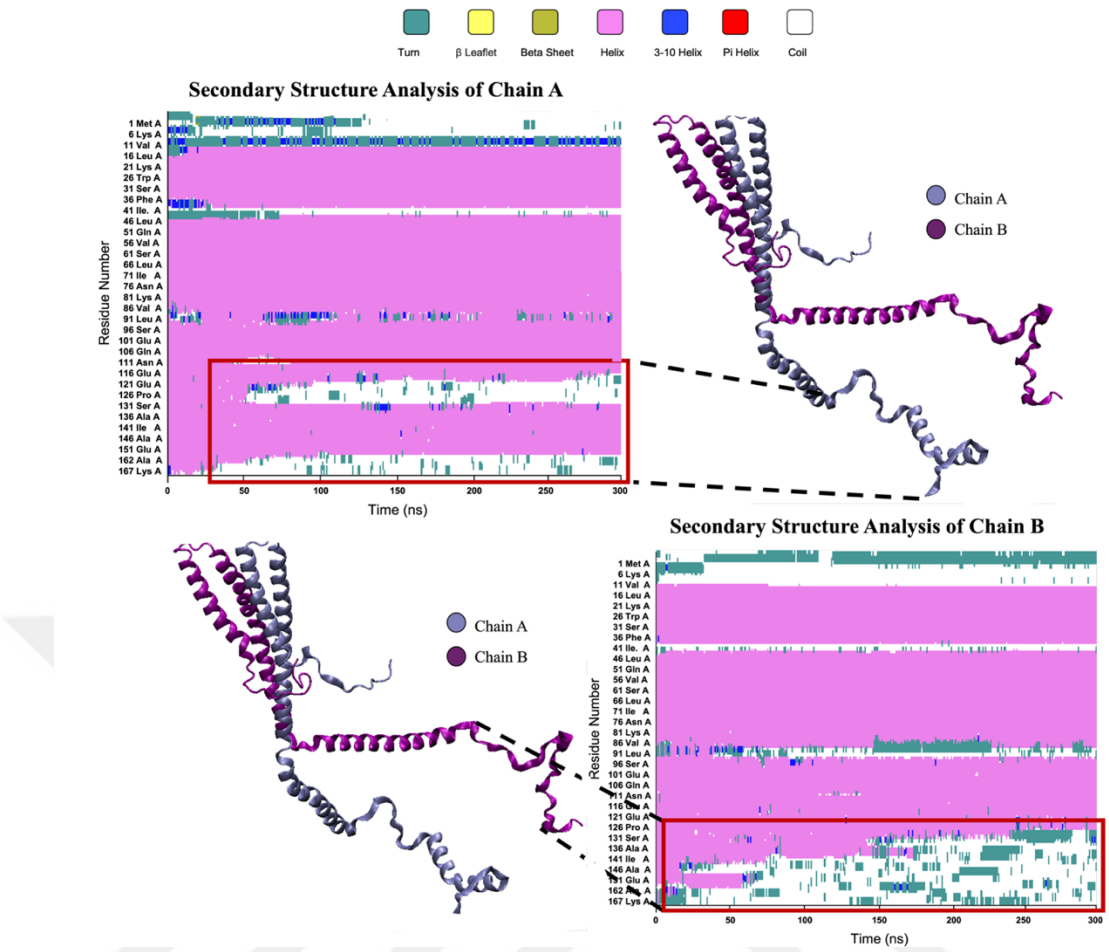


Figure 4.55: Secondary structure evolution of HolPhage-K dimer chains—Chain A (light purple) and Chain B (dark purple)—throughout the simulation, showing changes in helices, beta sheets, and coil regions.

Membrane thickness heatmap analysis revealed distinct regional thickness variations in the presence of the HolPhage-K dimer **(Figure 4.56 – B)**. Localized thinning of the membrane was observed in the dimer-containing system. In contrast, such variations were more limited in the membrane composed solely of *S. aureus*. Average thickness analysis further indicated a slight decrease in average membrane thickness in the presence of the HolPhage-K dimer (38.351 Å) compared to the control system (39.019 Å) **(Figure 4.56–C)**. These results are suggesting that protein disrupts lipid organization around its insertion site, thereby inducing local membrane flexibility.

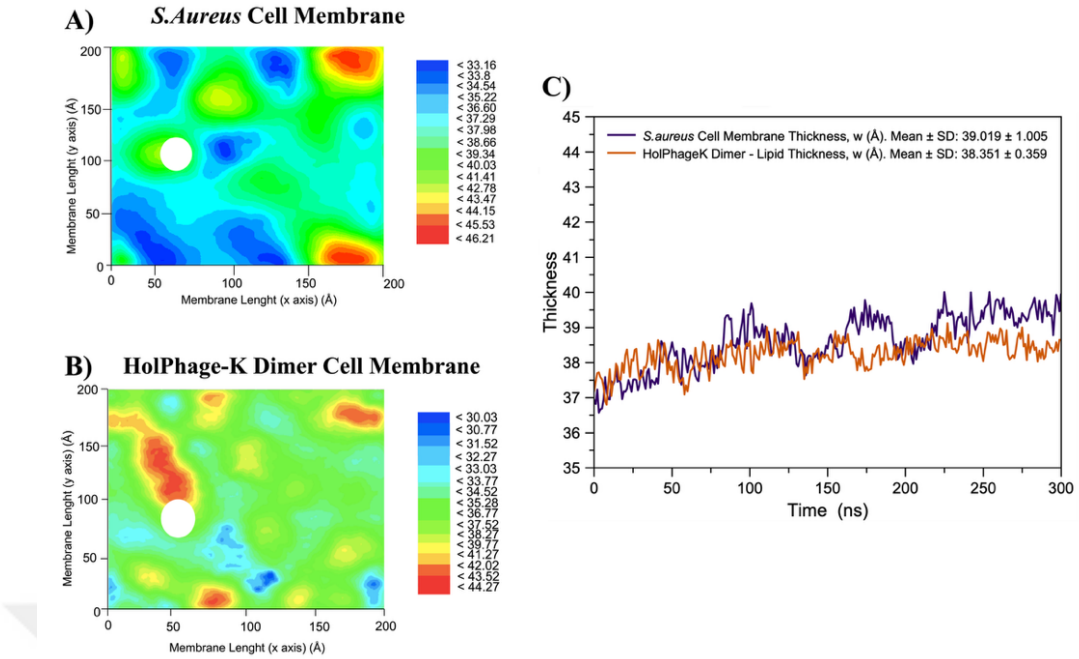


Figure 4.56: A) Thickness distribution map of the *S. aureus* cell membrane calculated over the simulation time. B) Thickness distribution map for the HolPhage-K dimer system. C)Time-dependent average membrane thickness plot for both systems.

Distance between the Met-1 residue located at the N-terminus of the HolPhage-K dimer and the DLPG and DPPG lipids during the simulation differs between Chain A and Chain B. As shown in Figure 4.57, Chain B maintained a more stable proximity to the membrane. This close association of the N-terminus with the cell membrane may play a critical role in the insertion and stability of the protein within the membrane.

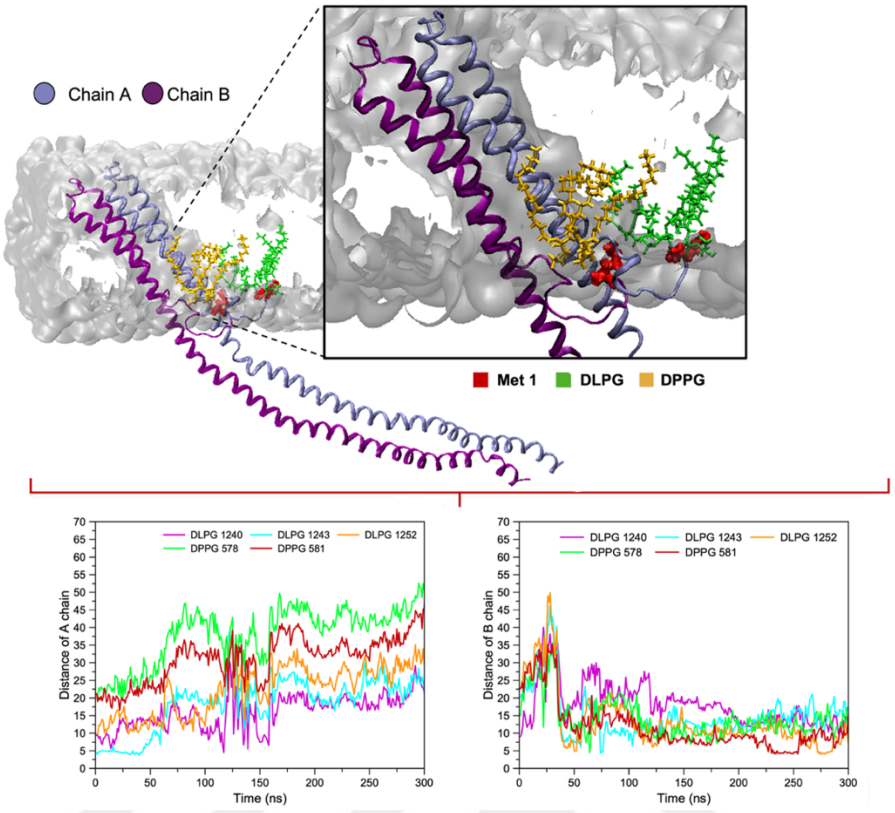


Figure 4.57: Representative structure (top) showing the interactions of the Met-1 residue located in the N-terminal region of the HolPhage-K dimer with selected DLPG (green) and DPPG (yellow) lipids within the membrane, and the time-dependent distance changes between these lipids and Chain A (left graph) and Chain B (right graph).

According to leaflet overlap analysis **(Figure 4.58 - A)**, both the WOR and the FMO significantly increased in the HolPhage-K dimer compared to control system. Similarly, proportion of atoms in contact with the opposing leaflet **(Figure 4.58- B)** was also higher in the HolPhage-K dimer system. These findings indicate that dimer form of holin protein induces structural alterations in membrane organization by enhancing the correlation and contact between membrane leaflets. FCOL was analyzed over time for the system containing the HolPhage-K dimer in **Figure 4.58 - B**. The average contact fraction was calculated as 0.063 ± 0.002 for the HolPhage-K system, compared to 0.056 ± 0.003 in the control system. This difference indicates that the presence of the dimer increases physical interactions between the leaflets.

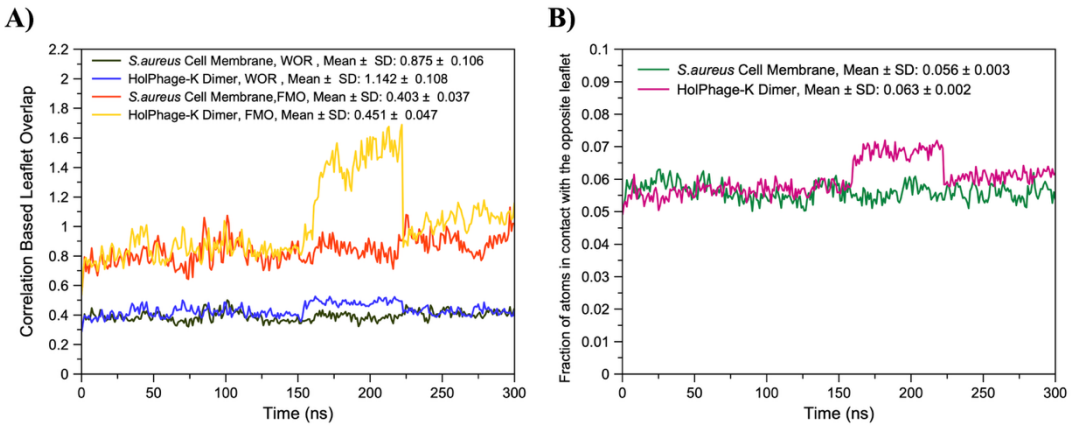


Figure 4.58: A) Leaflet overlap and contact analyses, the width of the overlapping region and mass fraction overlap were compared over time between the *S. aureus* and HolPhage-K dimer containing systems. B) The fraction of atoms in contact with the opposite leaflet was evaluated for both systems over 300 ns.

4.3.9 *S. aureus* Cell Membrane & HolPhage-K Tetramer MD Simulations

Tetrameric model, constructed by cross-arranging HolPhage-K monomers, was designed to mimic a potential pore or channel-like formation. Protein–lipid system was subjected to a 300 ns MD simulation.

RMSD, SASA, and Rg analyses calculated throughout 300 ns molecular dynamics simulation of HolPhage-K tetramer structure revealed a certain level of structural stability within the membrane environment. RMSD analysis **(Figure 4.59 - A)** showed a rapid increase during the first 50 ns, followed by fluctuating values in the range of 2.5–4.5 nm, indicating a system that had not fully equilibrated. SASA values **(Figure 4.59 - B)** exhibited only a minimal increase compared to initial state, fluctuating within the range of 550–580 nm². Rg data **(Figure 4.59 - C)** showed a gradual decreasing trend over the course of the simulation, suggesting that the tetramer structure evolved into a more compact form over time.

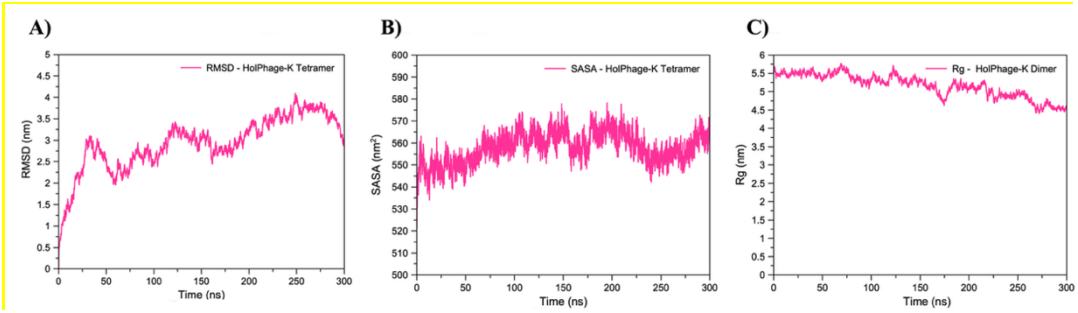


Figure 4.59: A) RMSD, B) SASA, C) Rg of the HolPhage-K tetramer over 300 ns MD simulations.

Trajectory data were examined to analyze the conformational changes of the tetrameric structure over the course of the simulation. HolPhage-K tetramer exhibited noticeable conformational rearrangements throughout simulation **(Figure 4.60)**. All four chains were oriented perpendicularly within the membrane at the beginning of the simulation. However, as simulation progressed, especially Chain A (blue) and Chain C (yellow) displayed altered orientations and terminal regions becoming more flexible and shifting outward. Especially at 300 ns, although the tetrameric structure was still in contact with the membrane, position differences and looseness between the monomers were observed.

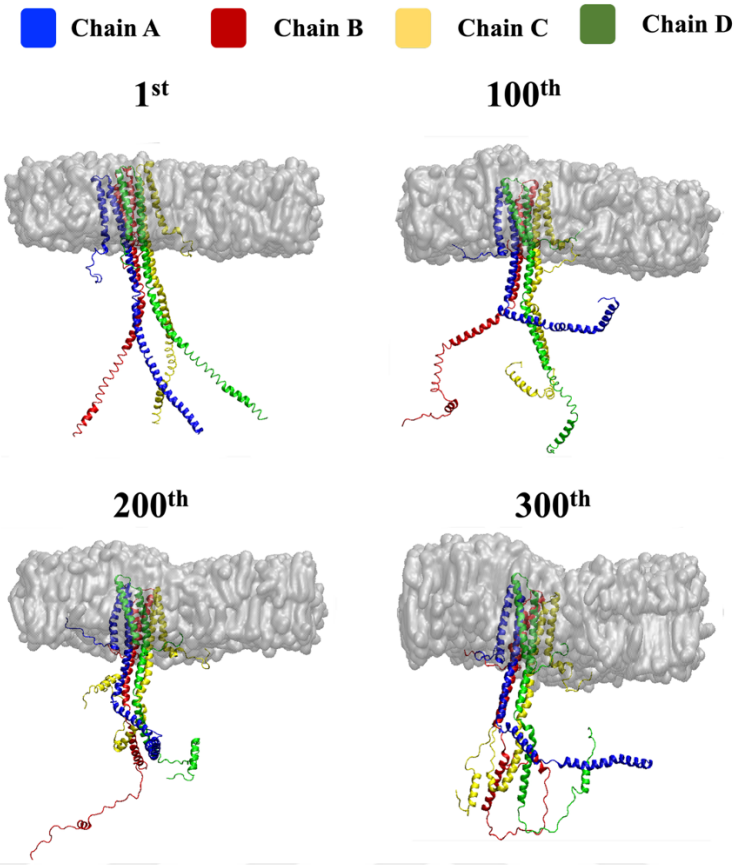


Figure 4.60: Snapshots showing the membrane-embedded positions of the four chains of the HolPhage-K tetramer (A: blue, B: red, C: yellow, D: green) at 1st ns, 100th ns, 200 th ns, and 300 th ns.

Time series images of the HolPhage-K tetramer show that there are significant conformational changes in the positions of four monomers (Chain A–D) in membrane. During the simulation, it was observed that especially Chain B (red) and Chain C (yellow) integrated deeper into lipid environment **(Figure 4.61)**. When trajectory data were examined, it was observed that there were differences in the degree of embedding of the chains forming tetramer in the membrane. Shift in the positions of some chains and an increase in the embedding depth in membrane are remarkable in 100–200 ns range. At the end of 300 ns, it was observed that monomers of tetramer structure came together, and structure became more compact.

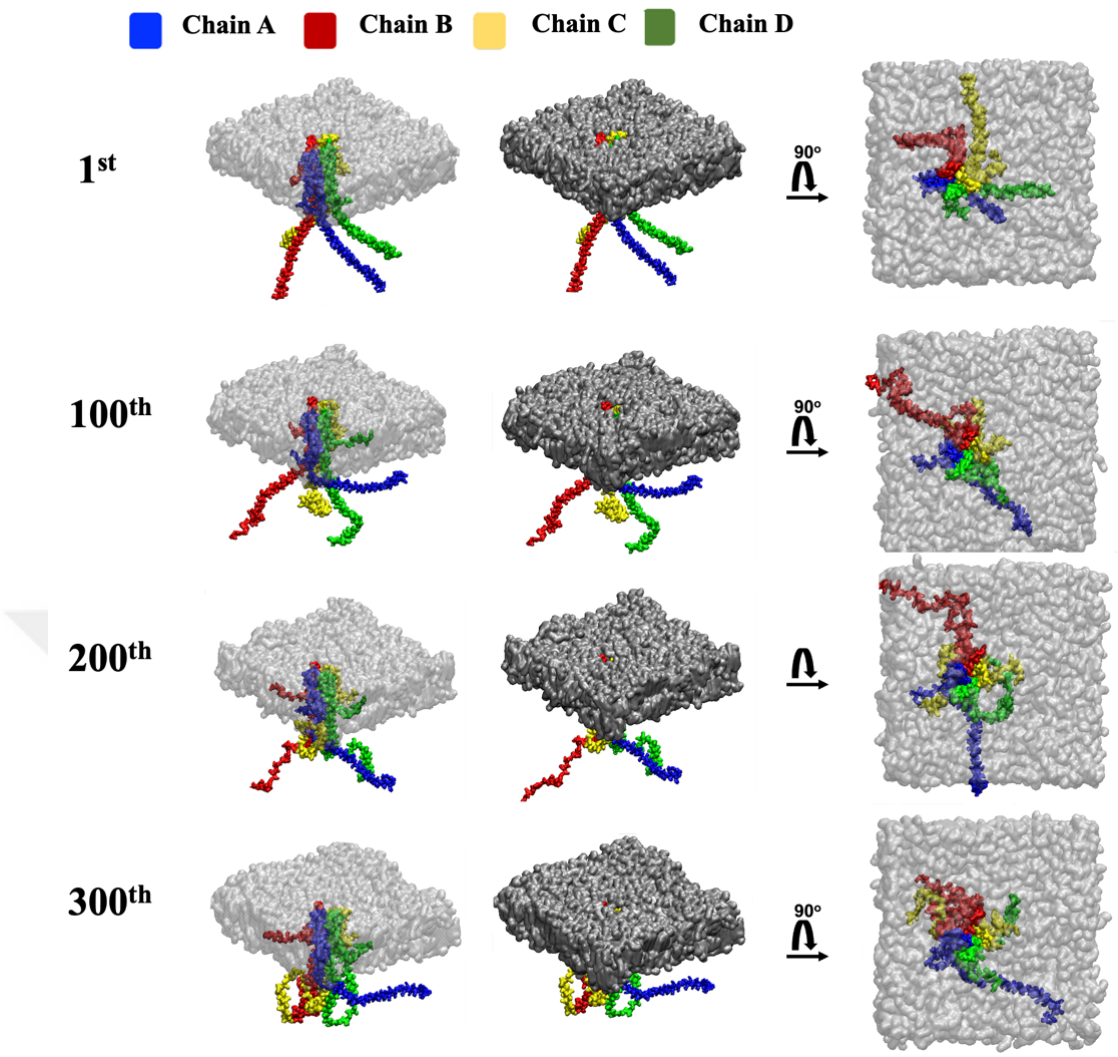


Figure 4.61: Position change of HolPhage-K tetramer protein on the cell membrane during the simulation, screenshots taken at 1st, 100th, 200th and 300th ns, respectively.

HolPhage-K tetramer model cell membrane did not exhibit significant differences in structural analysis parameters compared to the control *S. aureus* cell membrane **(Figure 4.62)**. Analysis results suggest that lipid environment in tetramer system maintained structural stability. Observed deviations in SASA and Rg values are likely attributable to the higher number of atoms present in the tetramer system.

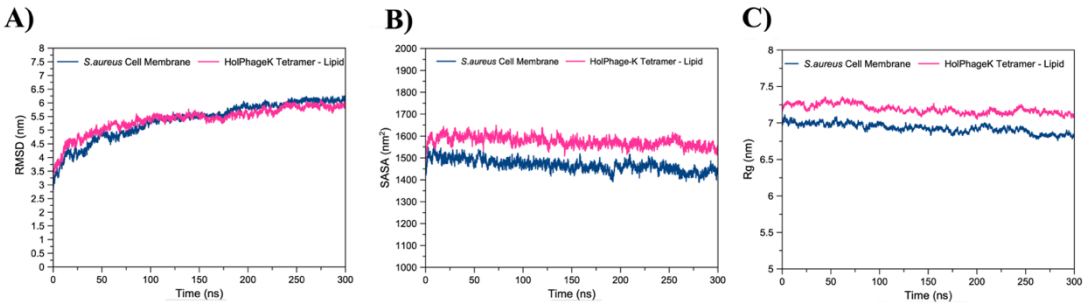


Figure 4.62: Comparison of structural parameters between the HolPhage-K tetramer–lipid system and the *S. aureus* cell membrane. A) RMSD, B) SASA, and C) Rg plots over 300 ns.

HolPhage-K tetramer model cell membrane did not exhibit significant differences in structural analysis parameters compared to the control *S. aureus* cell membrane. Analysis results suggest that lipid environment in tetramer system maintained structural stability. Observed deviations in SASA and Rg values are likely attributable to the higher number of atoms present in the tetramer system. *S. aureus* cell membrane is approximately 0.573 Å thicker than the membrane system containing the HolPhage-K tetramer. Color distribution diversity increased in the map analysis of the system containing HolPhage-K **(Figure 4.63 - A and B)**. This reveals regional thinning and thickening along the membrane.

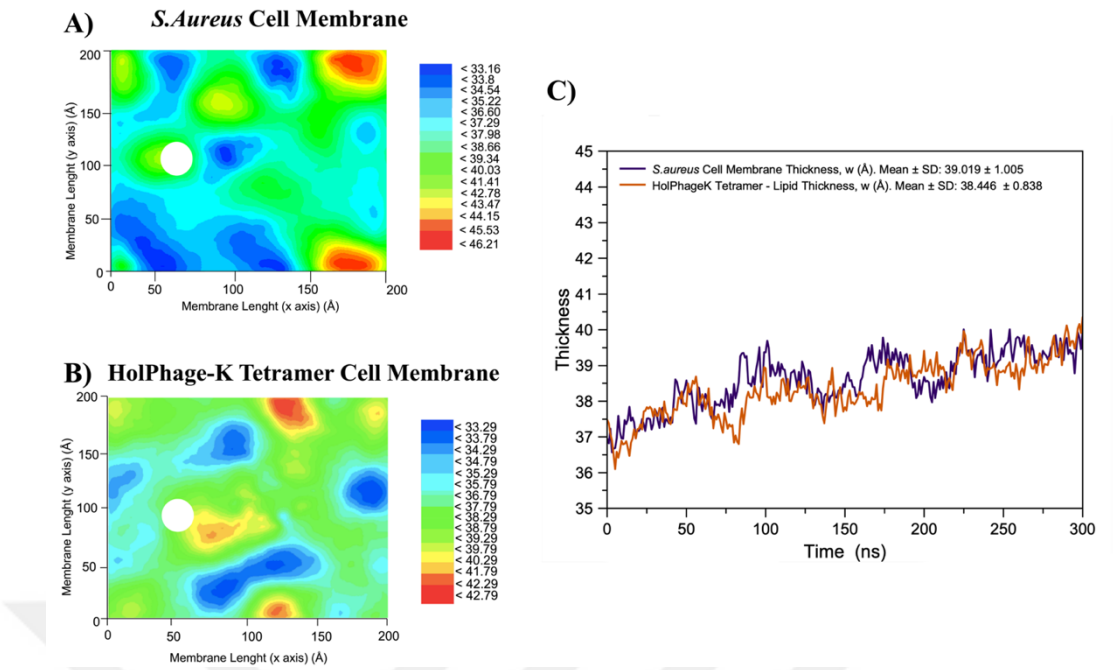


Figure 4.63: Membrane thickness analysis of A) *S. aureus* cell membrane and B) HolPhage-K tetramer embedded membrane. C) Time-averaged membrane thickness plot over 300 ns.

Figure 4.64 shows the results of leaflet interactions between the HolPhage-K tetramer system and control. In **Figure 4.64 - A**, fraction of atoms in contact with the opposite leaflet was compared. It was seen that this value was at the level of 0.056 ± 0.003 on average in both systems. In **Figure 4.64 - B**, two parameters related to leaflet overlap were analyzed. Overlap width was measured as 0.875 ± 0.106 nm in the control membrane, while this value was calculated as 0.830 ± 0.082 nm in the system containing holin. Overlap values according to mass fraction were found as 0.403 ± 0.037 (control) and 0.392 ± 0.031 (holin tetramer), respectively. In both parameters, presence of holin caused a minimal change in the membrane structure.

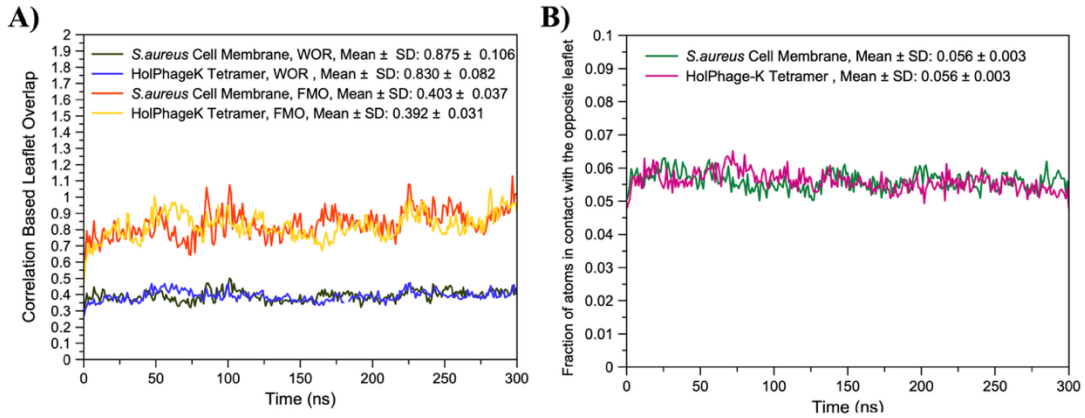


Figure 4.64: Leaflet overlap and contact analyses: A) The fraction of atoms in contact with the opposite leaflet was evaluated, B) The width of the overlapping region and mass fraction overlap were compared over time between the *S. aureus* and HolPhage-K dimer containing systems.

5. DISCUSSION AND CONCULUSION

5.1. Discussion

Experimental studies aimed at understanding the function of holin proteins present various challenges. Chief among these is that holins are membrane proteins, which makes their expression difficult, causes toxic effects in host cells, and requires expensive detergents and specialized laboratory equipment for purification. For these reasons, conducting experimental work on holins is particularly challenging. Although membrane proteins can be purified using various techniques, these methods demand significant time and resources. In contrast, computational approaches—especially MD simulations—offer a low-cost and scalable way to predict the structural properties of holins. Computational techniques can be considered a strategic first step in holin research. Indeed, there are no structural studies in the literature aimed at understanding how HolPhage-K and HolPhage-D29 proteins affect the bacterial cell membrane. This thesis aims to evaluate the structural effects of holin proteins on the cell membrane.

5.1.1 Evaluation of Structural Quality and Modeling Confidence of HolPhage-D29 and HolPhage-K

In the scope of this thesis, 3D structures of HolPhage-D29 and HolPhage-K were modeled. TMD of HolPhage-D29, as predicted by AlphaFold, was found to be structurally reliable, displaying high pLDDT scores (≥90) and low PAE values. These structural parameters indicate that the positions of both the protein backbone and side chains were predicted with high accuracy. It is well established in the literature that regions with pLDDT scores of 90 and above are highly reliable **[172], [173]**. In the structural modeling of HolPhage-D29, structural uncertainty was observed in the C-terminal region. The findings indicate that the C-terminal region is less conserved and possesses a more flexible structure.

In modeling the full-length HolPhage-D29 protein by AlphaFold, C-terminal region was perceived as like a TMD due to its hydrophobic character. Consequently, this region was predicted in a conformation embedded within the membrane. This artifact arises from AlphaFold's tendency to generate single-conformation solutions. For

terminal segments and other intrinsically disordered regions, multiple conformations exist in nature. These regions are typically less conserved evolutionarily, resulting in poor-quality MSAs, and lack well-defined single structural examples in AlphaFold's training dataset. As a result, AlphaFold assigns low confidence scores to such regions and fails to propose a reliable single structure. Due to this limitation, in modeling HolPhage-D29, the C-terminal segment was separated from the TMDs and modeled independently. Similar domain-by-domain modeling strategies, where different protein domains are predicted separately and subsequently assembled, have been reported in the literature.

HolPhage-K modeled using SWISS-MODEL was evaluated through Ramachandran plot analysis. The analysis revealed that 97.3% of the amino acid residues were in the most favored regions. This result indicated that the structure was energetically favorable. Ramachandran analysis is a highly reliable technique for assessing the accuracy of structures obtained through homology modeling **[174]**. Overall, both protein models used in this thesis provide a solid structural foundation for MD simulations.

5.1.2. Effect of HolPhage-D29 on *E. coli* Membrane Structure

HolPhage D29 was integrated into the *E. coli* cell membrane, and a 400 ns MD simulation was performed. The simulation findings generated various hypotheses regarding changes in both the protein and the cell membrane. Analysis of the protein's structure indicated that the system did not remain in a single stable conformation throughout the simulation; instead, it adopted transient interfacial conformations.

Previous literature investigating the oligomerization strategy of λ holin S105 demonstrated that changes in the flexibility of the holin protein induced the oligomerization process. In the case of HolPhage-D29, the structural rearrangements observed—especially in the C-terminal region—suggest a mechanism that induces oligomerization. Indeed, significant structural mobility was observed in HolPhage-D29 throughout the simulation **[76]**.

Increase in SASA values measured during the simulation of HolPhage-D29 was remarkable. This increase prove that more surface area of protein was exposed to solvent after it interacted with membrane. The findings are parallel to mechanism

observed in pore-forming toxins (PFTs) in the literature **[175]**. In the study conducted on PFTs, PFTs transformed from α helices to β hairpins after contact with the cell membrane. Oligomerization occurred and the surface area exposed to the solvent increased as PFTs settled into the membrane. The increase in SASA of HolPhage-D29, also indicates that protein was rearranged on the membrane. This may indicate monomer behavior before oligomerization.

Previous studies have disclosed that C-terminus of HolPhage-D29 plays an active role particularly in membrane disruption. The findings indicated that C-terminal helical segment gradually lost its linear structure, underwent bending, and exhibited dynamic motion throughout the simulation. This dynamic mechanism suggests that the monomer tends to move. Structural analyses of the protein designated that HolPhage-D29 possesses the structural flexibility required for membrane disruption **[176]**.

5.1.3. Effects of HolPhage-D29 Dimers on *E. coli* Membrane Structure and Holin Oligomerization Dynamics

Hole-forming mechanism of holins occurs through oligomerization. In addition to the single monomer simulation, the effects of two dimer configurations—cross-oriented and alongside—were comprehensively analyzed. This approach aimed to provide insights into both structural rearrangements and the oligomerization process. RMSD graphs of the *E. coli* cell membrane indicated that the membrane reached a stable conformation after approximately 200 ns. For this reason, the dimer and tetramer systems in this thesis were simulated for 300 ns

In the parallel dimer model, structural analyses indicated that the protein adopted a more compact conformation. Simulation results revealed that in the parallel model, the C-terminal segments tended to orient toward the membrane rather than interacting with each other. In contrast, in the cross-oriented model, the C-termini engaged in mutual interactions, leading to asymmetric bending in the TMDs. In the parallel arrangement, the C-termini may have favored membrane interactions, which are energetically more advantageous than inter-terminal interactions. In the cross model, the proximity of the C-terminal ends likely facilitated hydrophobic interactions between the monomers. Although not specific to holin proteins, previous studies on WALP peptides—synthetic transmembrane helices arranged in a parallel fashion—have demonstrated that rather than direct helix–helix interactions, changes in tilt and azimuthal rotation

optimize their interactions with the membrane. Coarse-grained MD simulations by Monticelli and Tieleman showed that the stabilization of parallel WALP23 dimers within the membrane was driven by such adjustments in tilt and rotation **[177], [178]**. Based on the literature, it can be inferred that the HolPhage-D29 alongside dimer undergoes structural rearrangements to facilitate interaction with the cell membrane.

Parallel dimer induced a significant increase in membrane thickness (40.64 ± 1.22 Å; control: 37.91 ± 0.51 Å) and promoted a more vertical alignment of lipid tails. Vertical tail alignment is a characteristic feature of the liquid-ordered phase and has been reported in the literature to reduce membrane permeability **[179]**. The membrane adopted a more compact structure. In the cross-oriented model, local thinning and heterogeneous thickness distribution were observed. Consistent with these findings, previous studies have reported that small membrane proteins can induce local lipid rearrangements and that hydrophobic mismatch can lead to changes in membrane thickness. This study demonstrates that, compared to the monomer, the dimer models exert distinct effects on membrane architecture, with the parallel configuration promoting a more pronounced increase in membrane compactness. Although different effects were observed in both models, the pronounced impact of the parallel dimer model on membrane thickness and structural parameters led to the construction of a tetramer model in which the monomers were positioned in a parallel configuration for the next stage of the simulation.

5.1.4. Effects of HolPhage-D29 Tetramer on *E. coli* Membrane Structure and Holin Oligomerization Dynamics

Structural changes in the monomers forming the tetramer revealed a pronounced bending and membrane-directed orientation in C-terminal regions, particularly after 100 ns. This behavior is a typical feature described in the literature for holin classes that contain a coiled-coil motif at the C-terminus. At this stage, the flexibility of the coiled-coil region may trigger oligomerization and membrane interaction **[180], [181]**. Similarly, in the parallel dimer model, monomers were also observed to orient toward the membrane. The results of both simulations suggest that the parallel alignment of monomers may serve as a strategy for reaching and interacting with the membrane. Tetramer model, like the dimer, exhibited a tighter and more compact conformation. Overall, the tetramer and parallel dimer simulations yielded comparable results.

Upon examining changes in membrane thickness and cell membrane integrity, it was observed that in the presence of the tetramer, the membrane thinned by approximately 0.51 Å. Supporting this finding, increases in FMO and WOR values, as well as greater overlap and proximity between phospholipid layers, were noted. Heatmap analysis of the simulation clearly revealed local membrane thinning, which may be associated with clustering in the C-terminal region. This phenomenon resembles the mechanism reported in the literature for TatA proteins, where amphipathic helix (APH) clustering pulls lipid head groups outward, reducing membrane thickness. Through this mechanism, local membrane thinning reportedly facilitates protein movement within the membrane **[182]**.

Considering our simulation data alongside the biological role of holin proteins, these localized membrane thinning could be interpreted as facilitating holin oligomerization and cluster formation within the membrane. Key effect mechanisms were identified in the presence of protein: membrane thinning, tighter oligomerization among protein monomers, C-terminus bending coupled with membrane interaction by the analysis of MD simulations.

5.1.5. Effects of HolPhage-D29 C-terminal on *E. coli* Membrane Structure

Potential of C-terminal region of HolPhage-D29 to interact independently with the cell membrane was investigated by modeling this region as a separate peptide and simulating it with the E. coli inner membrane. Previous studies have reported that this region alone may possess membrane-disruptive activity **[163], [183]**. Following a 300 ns MD simulation, the peptide was observed to remain near the membrane and reorient itself parallel to the membrane plane. Structural analyses showed that the peptide adopted a more stable and compact conformation throughout the simulation. Its persistent interaction with the membrane surface suggests that it adapted to the lipid environment and became stabilized within it.

The impact on membrane thickness was assessed and no statistically significant global alteration was detected. However, thickness heatmaps revealed localized thinning in the region where the C-terminal peptide remained associated. This suggested that the effect of the C-terminal might be spatially restricted and did not cause widespread structural disruption across the membrane.

Overall, these findings demonstrate that the C-terminal segment of HolPhage-D29 is capable of directly interacting with the membrane and exhibits a membrane-sensitive structural character.

5.1.6. Effect of HolPhage-K on *S. aureus* Membrane Structure

Structural changes in the protein were evaluated in the HolPhage-K simulation. Structural role of C-terminal region for HolPhage-K was clearly revealed. Snapshots of the structure obtained during the MD simulation and Bendix analysis showed that this region underwent a structural change. During this structural transition process, C-terminal segment extended outward to the membrane, like that seen in HolPhage-D29, and gradually folded and approached the membrane. This observation suggested that the C-terminal region has high flexibility and may play an active role in membrane destabilization.

As a result of the protein-free *S. aureus* membrane simulation, the membrane thickness was measured as ~38.38 Å. This value is consistent with previously measured S. aureus cell membrane thickness values in the literature **[184], [185].** The effect of HolPhage-K on the *S.aureus* membrane was evaluated. When the thickness analysis and heat map analysis were examined, it was seen that thinned membrane regions were formed locally in the lipid regions around HolPhage-K. In the literature, it was shown that local thinning and lipid shifting may occur in the cell membrane because of elastic stress caused by protein placement **[186] [187]**. The analysis results performed on the cell membrane indicate weakening of the membrane, sliding of lipid layers on each other and a change in the direction of general thinning in terms of thickness. This thinning may constitute a prerequisite for holin oligomerization and endolysin activity.

5.1.7. Effects of HolPhage-K Dimer and Tetramer on *S.aureus* Membrane Structure and Holin Oligomerization Dynamics

The primary motivation behind modeling the dimeric and tetrameric structures of HolPhage-K stems from the fact that, according to the literature, the functional activity of holin proteins typically emerges in oligomeric forms. Numerous studies have demonstrated that holins embed into cell membranes and form ring-like or channel-like structures composed of multiple monomers **[188], [189], [190], [191]**.

Previous studies on HolPhage-D29 reported the most pronounced membrane alterations in the parallel dimer model. Consequently, the dimeric structure of HolPhage-K was modeled by aligning the monomers in a parallel orientation. MD simulations performed using the parallel dimer model revealed localized membrane thinning. These results are like those observed with the HolPhage-D29 dimer (alongside) and with the HolPhage-K simulation. The simulation data clearly showed a gradual increase in flexibility in the C-terminal regions of the HolPhage-K dimer and a tendency toward coiled-coil formation over the course of the simulation.

A literature review indicates that flexibility of the C-terminal regions in membrane-penetrating proteins with holin-like mechanisms plays a crucial role in membrane insertion. One study emphasized that coil formation at the termini of gamma-hemolysin serves as a trigger for entering membrane defects. Following the acquisition of flexibility, the C-terminal regions orient toward the inner leaflet of the membrane, acting as a step that weakens local membrane integrity and increases permeability **[192]**. Unlike the HolPhage-D29 dimer (alongside) and HolPhage-D29 tetramer, the monomers comprising the HolPhage-K dimer also interact with each other during parts of the simulation. The secondary structure changes occurring at the C-terminal ends—which engage both intra-protein and lipid interactions—may indicate a protein refolding process.

HolPhage-K dimer model did not induce membrane alterations as prominently as the parallel dimer of HolPhage-D29. Therefore, in the HolPhage-K tetramer model, a configuration was designed in which the TMDs were arranged back-to-back (cross-oriented, tube-like) to test whether a channel-like structure could span the membrane. Interestingly, each monomer within the tetramer exhibited a distinct pattern; however, all C-terminal regions gradually transitioned into random coils over time. Despite these conformational changes, membrane thickness remained very similar to that of the control system, and leaflet overlap measurements remained nearly unchanged. These findings suggest that the channel-like conformation adopted in this tetrameric arrangement does not represent a functional oligomerization form.

5.1.8. Importance of Cell Membrane Thickness Changes

Evaluation of different HolPhage-D29 models in terms of membrane thickness and regional variations in cell membrane thickness revealed that the parallel dimer model markedly increased membrane thickness, while also inducing localized thinning in certain areas. Thickness changes and interdigitation analyses indicated that lipid tails were more uprightly aligned, resulting in a more compact and rigid membrane structure. In the cross-oriented dimer model, localized thinning and heterogeneous thickness distributions were observed, potentially causing irregularities in membrane fluidity and permeability across different regions of the cell membrane. The tetramer model exhibited localized thinning and increased overlap and proximity between phospholipid leaflets. Simulation of the C-terminal peptide alone did not lead to a significant change in global thickness; however, it induced localized thinning in the membrane region it interacted with. Similar patterns of thinning and thickening were also observed in HolPhage-K parallel dimer models. The observed changes in membrane thickness—particularly thickening—can be attributed to a more orderly arrangement of lipid tails, which may reduce lateral diffusion, thereby decreasing membrane fluidity. This reduction in fluidity may, in turn, restrict membrane permeability and enhance the stability of proteins embedded within the membrane. Conversely, regions of thinning promote localized fluidity and increased curvature of lipid tails, creating favorable sites for membrane protein insertion or oligomerization. Literature reports include MD simulation studies examining the effects of membrane thickness on protein localization, permeability, and lipid phase behavior. These studies have shown that increased membrane thickness can slow the translocation rates of membrane proteins, and that an inverse relationship exists between thickness and permeability. In summary, the average and regional lipid thickness changes obtained from the lipid models in this study demonstrate that the mechanical and dynamic properties of membranes can be altered in distinct ways.

5.2. Conclusion

This thesis presents a comprehensive investigation of the effects of the holin proteins HolPhage-D29 and HolPhage-K on bacterial cell membranes using MD simulations. The results demonstrated that both holins induced substantial alterations in membrane

architecture. In particular, the parallel dimer and tetramer conformations of HolPhage-D29 exhibited rearrangements that favored oligomerization. Since the activity of HolPhage-D29 in *E. coli* membranes was experimentally proven, the structural changes observed in HolPhage-D29 MD simulations were considered representative of the membrane-disrupting activity of the protein. Based on these results, additional simulations were conducted to evaluate the behavior of HolPhage-K. Similar membrane effects were observed in its monomeric and dimeric forms, suggesting that oligomerization in holins occurs through parallel alignment of monomers. Outcomes of this study represent an important step toward elucidating the intramembrane dynamics of holin proteins and their potential oligomerization pathways. Nevertheless, this study has several limitations. Simulations employed a limited number of initial structural arrangements and orientations, and alternative dimeric and tetrameric configurations were not systematically explored. This constraint introduces the possibility that other biologically relevant conformations may have been overlooked. To address this, future studies should involve extended simulations with multiple initial conformations to capture a broader range of structural transitions. Moreover, integrating additional components of the bacterial envelope, such as the peptidoglycan layer and outer membrane, would enable the construction of more physiologically relevant models.

The approach used in our thesis enabled us to understand the behavior of holin proteins within the cell membrane. Modeling the membrane system in a more comprehensive manner—including the cell wall and peptidoglycan structures—could allow for a more accurate analysis of the effects of holins on the membrane. Additionally, different holin proteins can be modeled within various types of membranes to better evaluate specific interactions. Holins that are found to be effective in disrupting the membrane can be targeted to optimize protein engineering and expression systems accordingly. Since isolating holins is both expensive and time-consuming, a structure-based pre-screening step could provide substantial savings in time and resources prior to experimental studies.

Looking forward, holin proteins hold considerable promise for various biotechnological applications. These include the induction of controlled cell death mechanisms, development of targeted antibacterial agents, and design of synthetic systems for modulating bacterial membrane permeability. In this context, insights

gained from MD simulations not only advance fundamental understanding but also provide a strategic foundation for the translational exploitation of holin proteins.

In conclusion, this thesis has elucidated key aspects of the membrane interaction dynamics of HolPhage-D29 and HolPhage-K. It has highlighted the structural flexibility and membrane-oriented behavior of their C-terminal regions. Understanding the early structural events underpinning holin

REFERENCES

[1] Whitman, W. B., Coleman, D. C., & Wiebe, W. J., (1998), "Prokaryotes: The unseen majority", Proceedings of the National Academy of Sciences, 95 (12), 6578–6583. doi: 10.1073/PNAS.95.12.6578.

[2] Porter, J. R., (1976), "Antony van Leeuwenhoek: tercentenary of his discovery of bacteria", Bacteriological Reviews, 40(2), 260–269. doi: 10.1128/BR.40.2.260-269.1976.

[3] https://www.etymonline.com/word/bacteria. Accessed Date: 9.04.2025.

[4] Smith, K. A., (2012), "Louis Pasteur, the father of immunology?", Frontiers in Immunology, 3.

[5] Gal, J., (2008), "The discovery of biological enantioselectivity: Louis Pasteur and the fermentation of tartaric acid, 1857- A review and analysis 150 yr later", Chirality, 20(1), 5–19.

[6] Brock, T. D., (1988), "Robert Koch: a life in medicine and bacteriology", *Choice Reviews Online*, 26 (6), 26-3255-26–3255,

[7] Bardell, D., (2002), "Bacillus anthracis (Anthrax) Has a Unique Place in the History of Microbiology. Bios", 73(4), 133–136. http://www.jstor.org/stable/4608647.

[8] Gradmann, C., (2001), "Robert Koch and the Pressures of Scientific Research: Tuberculosis and Tuberculin", Medical History, 45(1), 1–32. doi:10.1017/S0025727300000028.

[9] Byrd, A. L., Segre, J. A., (2016), "Adapting Koch's postulates: Criteria for disease causation must take microbial interactions into account", Science, 351(6270), 224–226.

[10] Tan, S. Y., Berman, E., (2008), "Robert Koch (1843-1910): father of microbiology and Nobel laureate". Singapore medical journal, 49 (11), 854-855

[11] Dosani, S., (2005). "Penicillin Man: Alexander Fleming and the Antibiotic Revolution", 330 (7481), 50.

[12] Seber, E., (2010), "Tüberkülozun dünü", Ankem, 24, 52-60.

[13] Liu, F., & Myers, A. G., (2016), "Development of a platform for the discovery and practical synthesis of new tetracycline antibiotics", Current Opinion in Chemical Biology, 32, 48–57.

[14] Kayser, F. H., Bienz, K. A., Eckert, J., Zinkernagel, R. M., (2005), "Kaiser, Medical Microbiology", Microbiology, 725.

[15] Tortora G. J., Funke B. R., Case C. L., Al-Mukhtar T., (2010), "Microbiology : An Introduction with 10th Edition", 10th Edition, 0–960.

[16] Martínez-Palomo A., (1970), “The Surface Coats of Animal Cells”, International Review of Cytology, 29(C), 29–75.

[17] Vollmer W., (2012), “Bacterial growth does require peptidoglycan hydrolases”, Molecular Microbiology, 86(5), 1031–1035.

[18] Costerton J. W., Irvin R. T., & Cheng K. J., (1981), “The bacterial glycocalyx in nature and disease”, Annual Review of Microbiology, 35, 299–324.

[19] Srivastava D., (2021), “Elementary Microbiology,” Wallnut Publication.

[20] Rogers H. J., Perkins H. R., & Ward J. B., (1980), “Structure of peptidoglycan”, Microbial Cell Walls and Membranes, 190–214.

[21] Galinier A., Delan-Forino C., Foulquier E., Lakhal H., & Pompeo F., (2023), “Recent Advances in Peptidoglycan Synthesis and Regulation in Bacteria”, Biomolecules, 13(5).

[22] Armstrong J. J., Baddiley J., Buchanan J. G., Carss B., Greenberg G. R., (1958), “Isolation and structure of ribitol phosphate derivatives (teichoic acids) from bacterial cell wall”, Journal of the Chemical Society, 4344–4354.

[23] Kojima N., Araki Y., Ito E., (1985), “Structure of the linkage units between ribitol teichoic acids and peptidoglycan. Journal of Bacteriology”, 161(1), 299–306.

[24] Navarre W. W., Schneewind O., (1999), “Surface Proteins of Gram-Positive Bacteria and Mechanisms of Their Targeting to the Cell Wall Envelope”, Microbiology and Molecular Biology Reviews, 63(1), 174–229. doi: 10.1128/MMBR.63.1.174-229.1999.

[25] Rajagopal M., Walker S., (2017), “Envelope Structures of Gram-Positive Bacteria”, Current Topics in Microbiology and Immunology, 404, 1.

[26] de Petris S., (1967), “Ultrastructure of the cell wall of *Escherichia coli* and chemical nature of its constituent layers”, Journal of Ultrasructure Research, 19(1–2), 45–83.

[27] Seltmann G., & Holst O., (2002), “The Bacterial Cell Wall”.

[28] Lüderitz O., Galanos C., Lehmann V., Nurminen M., Rietschel E. T., Rosenfelder G., Simon M., Westphal O., (1973), “Lipid a: Chemical structure and biological activity”, Journal of Infectious Diseases, 128, 17–29.

[29] Rothfield L., Romeo D., (1971), “Role of lipids in the biosynthesis of the bacterial cell envelope”, Bacteriological Reviews, 35(1), 14–38.

[30] Dirienzo J. M., Nakamura K., Inouye M., (1978), “The outer membrane proteins of Gram-negative bacteria: biosynthesis, assembly, and functions”, Annual Review of Biochemistry, 47, 481–532.

[31] Bayer M. E., Bayer M. H., (1994), "Periplasm. New Comprehensive Biochemistry", 27, 447–464.

[32] Miller S. I., Salama, N. R., (2018), "The gram-negative bacterial periplasm: Size matters", PLoS Biology, 16 (1).

[33] Leigh J., Dodsworth J., (2007), "Bakteri ve arkelerde azot düzenlenmesi". Annu. Rev. Microbioly, 67, 349-377.

[34] Shimshick E. J., Hebert R. R., (1979), "Binding Characteristics of N 2 -Fixing Bacteria to Cereal Roots", Applied and Environmental Microbiology, 38 (3), 447–453.

[35] Delogu G., Sali M., (1999), "The biology of *Mycobacterium tuberculosis* infection"., Mediterranean Journal Of Hematology And İnfectious Diseases, 5(1).

[36] Gast R. K., Porter R. E., (2019), "Salmonella infections", Diseases of Poultry, 719–753.

[37] Love T. E., Jones B., (2008), "Introduction to Pathogenic Bacteria", Principles of Bacterial Detection: Biosensors, Recognition Receptors and Microsystems, 3 (13).

[38] Uluseker C., Kaster K. M., Thorsen K., Basiry D., Shobana S., Jain M., Kumar G., Kommedal R., Pala-Ozkok I., (2021). "A Review on Occurrence and Spread of Antibiotic Resistance in Wastewaters and in Wastewater Treatment Plants: Mechanisms and Perspectives", Frontiers in Microbiology, 12.

[39] Davison H. C., Woolhouse M. E. J., & Low J. C., (2000)", What is antibiotic resistance and how can we measure it?", Trends in Microbiology, 8 (12), 554–559.

[40] Schneider E., Paul D., Ivy P., & Cowan K. H., (1999). "Multidrug resistance. Cancer Chemotherapy and Biological Response Modifiers", 18, 152–177.

[41] ABUT L. İ., (2007), "Enterotoksijenik *Escherichia Coli*", Türkiye Klinikleri Tıp Bilimleri Dergisi, 27 (5), 768–773.

[42] Fatima R., Nguyen A. D., & Aziz M., (2025), "Enterohemorrhagic *Escherichia coli",* StatPearls.

[43] Nisa S., Scanlon K. M., Donnenberg M. S., (2013), "Enteropathogenic *Escherichia coli*", *Escherichia Coli*: Pathotypes and Principles of Pathogenesis: Second Edition, 75–119. doi: 10.1016/B978-0-12-397048-0.00004-8.

[44] Demirtürk N., Demirdal T., (2004), "The Problem of The Antimicrobial Drug Resistance", The Medical Journal of Kocatepe, 5, 17–21.

[45] Paterson D. L., (2000), "Recommendation for treatment of severe infections caused by Enterobacteriaceae producing extended-spectrum β-lactamases (ESBLs)", Clinical Microbiology and Infection, 6 (9), 460–463. doi: 10.1046/J.1469-0691.2000.00107.X/PDF

[46] *Escherichia coli* (Scenning Electron Microscopy). Wikimedia commons. https://upload.wikimedia.org/wikipedia/commons/a/a6/Escherichia_coli_%28SEM%29.jpg. Accessed: 22.08.2025.

[47] Costa A. R., Batistão D. W. F., Ribas R. M., Sousa A. M., Pereira M. O., Botelho C. M., (2014), "*Staphylococcus aureus* virulence factors and disease", Microbial Pathogens and Strategies for Combating Them: Science, Technology and Education, 3, 1668–1674.

[48] Bohach G. A., Fast D. J., Nelson R. D., & Schlievert P. M., (1990), *Staphylococcal* and *Streptococcal* Pyrogenic Toxins Involved in Toxic Shock Syndrome and Related Illnesses", Critical Reviews in Microbiology, 17 (4), 251–272. doi: 10.3109/10408419009105728.

[49] Dayan G. H., Mohamed N., Scully I. L., Cooper D., Begier E., Eiden J., Jansen K. U., Gurtman A., & Anderson A. S., (2016), "*Staphylococcus aureus*: the current state of disease, pathophysiology and strategies for prevention", Expert Review of Vaccines, 15(11), 1373–1392. doi: 10.1080/14760584.2016.1179583.

[50] Pantosti A., Venditti M., (2009), "What is MRSA?", European Respiratory Journal, 34(5), 1190–1196. doi: 10.1183/09031936.00007709.

[51] Gould I. M., (2013), "Treatment of bacteraemia: meticillin-resistant *Staphylococcus aureus* (MRSA) to vancomycin-resistant *S. aureus* (VRSA)", International Journal of Antimicrobial Agents, 42 (Sppl.1),17–21.

[52] Masters E. A., Muthukrishnan G., Ho L., Gill A. L., de Mesy Bentley K. L., Galloway C. A., McGrath J. L., Awad H. A., Gill S. R., Schwarz E. M., (2021), "*Staphylococcus aureus* Cell Wall Biosynthesis Modulates Bone Invasion and Osteomyelitis Pathogenesis. Frontiers in Microbiology", 12, 723498.

[53] Chwalibog A., Sawosz E., Hotowy A., Szeliga J., Mitura S., Mitura K., Grodzik M., Orlowski P., & Sokolowska A., (2010), "Visualization of interaction between inorganic nanoparticles and bacteria or fungi", International Journal of Nanomedicine, 5(1), 1085–1094. doi: 10.2147/IJN.S13532.

[54] Lu J., Zhang Y., Wu J., Wang J., (2022), "Intervention of antimicrobial peptide usage on antimicrobial resistance in aquaculture", Journal of Hazardous Materials, 427, 128154. doi: 10.1016/J.JHAZMAT.2021.128154.

[55] Yasir M., Willcox M. D. P., Dutta D., (2018), "Action of Antimicrobial Peptides against Bacterial Biofilms", Materials, 11 (12), 2468.

[56] Tao S., Chen H., Li N., & Liang W., (2022), "The Application of the CRISPR-Cas System in Antibiotic Resistance. Infection and Drug Resistance", 15, 4155–4168. doi: 10.2147/IDR.S370869.

[57] Elshaghabee F. M. F., Rokana N., (2022), "Mitigation of antibiotic resistance using probiotics, prebiotics and synbiotics. A review", Environmental Chemistry Letters, 20 (2), 1295–1308. doi: 10.1007/S10311-021-01382-W

[58] Hadidi A., Sun L., Randles J. W., (2022), “Modes of Viroid Transmission”, Cells, 11(4), 719. doi: 10.3390/CELLS11040719.

[59] “The Actinobacteriophage Database Phage D29.” [https://phagesdb.org/phages/D29/ . Accessed Date: 10.04.2025

[60] Ford M. E., Sarkis, G. J., Belanger A. E., Hendrix R. W., Hatfull G. F., (1998), “Genome structure of mycobacteriophage D29: implications for phage evolution”, Journal of Molecular Biology, 279(1), 143–164. doi: 10.1006/JMBI.1997.1610.

[61] Hobbs Z., Abedon S. T., (2016), “Diversity of phage infection types and associated terminology: the problem with ‘Lytic or lysogenic”, Microbiology Letters, 363 (7).

[62] Guttman B., Raya R., Kutter E., (2005), “Basic phage biology. Bacteriophages: Biology and applications”, 4, 30-63.

[63] Fernandes S., Sofia C., São-José C., (2016), “More than a hole: the holin lethal function may be required to fully sensitize bacteria to the lytic action of canonical endolysins”, Molecular Microbiology, 102 (1).

[64] Kamilla S., Jain V., (2016), “Mycobacteriophage D29 holin C-terminal region functionally assists in holin aggregation and bacterial cell death”, FEBS Journal, 283 (1), 173–190.

[65] Grabowski Ł., Łepek K., Stasiłojć M., Kosznik-Kwaśnicka K., Zdrojewska K., Maciąg-Dorszyńska M., Węgrzyn G., Węgrzyn A., (2021), “Bacteriophage-encoded enzymes destroying bacterial cell membranes and walls, and their potential use as antimicrobial agent”, Microbiological Research, 248.

[66] Fernandes S., Sofia C., São-José C., (2016), “More than a hole: the holin lethal function may be required to fully sensitize bacteria to the lytic action of canonical endolysins”, Molecular Microbiology, 102 (1).

[67] White R., Chiba S., Pang T., Dewey J. S., Savva C. G., Holzenburg A., Pogliano K., & Young R., (2011), “Holin triggering in real time”, Proceedings of the National Academy of Sciences of the United States of America, 108(2), 798–803.

[68] Kochhar R., (2020), “The virus in the rivers: histories and antibiotic afterlives of the bacteriophage at the sangam in Allahabad”, Notes and Records, 74(4), 625–651.

[69] Slopek S., Kucharewicz-Krukowska A., Weber-Dabrowska B., Dabrowski M., (1985), “Results of bacteriophage treatment of suppurative bacterial infections”, Archivum Immunologiae et Therapiae Experimentalis, 33 (2), 219–240

[70] Rhoads D. D., Wolcott R. D., Kuskowski M. A., Wolcott B. M., Ward L. S., Sulakvelidze A., (2009), “Bacteriophage therapy of venous leg ulcers in humans: Results of a phase i safety trial”, Journal of Wound Care, 18 (6), 237–243.

[71] Aminov R. I., (2010), “A brief history of the antibiotic era: lessons learned and challenges for the future”, Frontiers in Microbiology, 1.

[72] Hutchings M., Truman A., Wilkinson B., (2019), “Antibiotics: past, present and future. Current Opinion in Microbiology”, 51, 72–80.

[73] Harper D. R., Parracho H. M. R. T., Walker J., Sharp R., Hughes G., Werthén M., Lehman S., Morales S., (2014), “Bacteriophages and Biofilms”, Antibiotics, 3 (3), 270.

[74] Cunha B. A., (2001), “Antıbıotıc Sıde Effects”, Medical Clinics of North America, 85 (1), 149–185.

[75] Leviton I., (2005), “Separating Fact from Fiction: The Data Behind Allergies and Side Effects Caused by Penicillins, Cephalosporins, and Carbapenem Antibiotics”, Current Pharmaceutical Design, 9 (12), 983–988.

[76] Zhou B., Wu Y., Su Z., (2021), “Computational simulation of holin s105 in membrane bilayer and its dimerization through a helix-turn-helix motif”, The Journal of Membrane Biology, 254 (4), 397.

[77] Krysiak-Baltyn K., Martin G. J. O., Gras S. L., (2018), “Computational modeling of bacteriophage production for process optimization”, Methods in Molecular Biology, 1693, 195–218.

[78] Nilsson A. S., (2022), “Cocktail, a Computer Program for Modelling Bacteriophage Infection Kinetics”, Viruses, 14 (11).

[79] Duda R. L., Huet A., (2016), “Bacteriophages: Tailed”, Encyclopedia of Life Sciences, 1 (8).

[80] Catalão M. J., Gil F., Moniz-Pereira J., São-José C., Pimentel M., (2013), “Diversity in bacterial lysis systems: bacteriophages show the way”, FEMS Microbiology Reviews, 37 (4), 554–571.

[81] O’Flaherty S., Coffey A., Edwards R., Meaney W., Fitzgerald G. F., Ross R. P., (2004), “Genome of Staphylococcal Phage K: A New Lineage of Myoviridae Infecting Gram-Positive Bacteria with a Low G+C Content”, Journal of Bacteriology, 186 (9), 2862–2871.

[82] Bavda V. R., Yadav A., Jain V., (2021), “Decoding the Molecular Properties of Mycobacteriophage D29 Holin Provides Insights into Holin Engineering”, Journal of Virology, 95 (10).

[83] National Center for Biotechnology Information, Protein Structure, NCBI, https://www.ncbi.nlm.nih.gov/protein/NP_046826.1?report=fasta . Accessed date: 2025

[84] “holin [*Staphylococcus* faj K]- Protein- NCBI.” https://www.ncbi.nlm.nih.gov/protein/YP_009041295.1 . Accessed: 15.03.2025.

[85] Nussinov R., Zhang M., Liu Y., Jang H., (2022), "AlphaFold, Artificial Intelligance (AI) and allostery", Fiziksel Dergisi, 126 (34), 6372–6383.

[86] Jumper J., Evans R., Pritzel A., Green T., Figurnov M., Ronneberger O., Tunyasuvunakool K., Bates R., Žídek A., Potapenko A., Bridgland A., Meyer C., Kohl S. A. A., Ballard A. J., Cowie A., Romera-Paredes B., Nikolov S., Jain R., Adler J., Hassabis D., (2021), "Highly accurate protein structure prediction with AlphaFold", Nature, 596 (7873), 583–589. doi: 10.1038/s41586-021-03819-2.

[87] Baker D., Sali A., (2001)., "Protein structure prediction and structural genomics". Science (New York, N.Y.), 294 (5540), 93–96.

[88] Blattmann B., Sticher P., "Proteinleri kristallere büyütme", Science in School, https://www.scienceinschool.org/tr/article/2010/lysozyme-tr/. Accessed date: 15.03.2025

[89] Zheng H., Handing K., B., Zimmerman M. D., Shabalin I. G., Almo S. C., Minor W., (2015), "X-ray crystallography over the past decade for novel drug discovery–where are we heading next?", Expert opinion on drug discovery, 10 (9), 975-989.

[90] Keeler J., (2011), " Understanding NMR spectroscopy", John Wiley & Sons.

[91] Gronwald W., Kalbitzer H. R., (2004), " Automated structure determination of proteins by NMR spectroscopy", Progress in Nuclear Magnetic Resonance Spectroscopy, 44 (1–2), 33–96.

[92] Bai X., chen, McMullan G., Scheres S. H. W., (2015), "How cryo-EM is revolutionizing structural biology", Trends in Biochemical Sciences, 40 (1), 49–57.

[93] Jumper J., Evans R., Pritzel A., Green T., Figurnov M., Ronneberger O., Hassabis D., (2021), "Highly accurate protein structure prediction with AlphaFold", Nature, 596 (7873), 583-589.

[94] Varadi M., Bertoni D., Magana P., Paramval U., Pidruchna I., Radhakrishnan M., Tsenkov M., Nair S., Mirdita M., Yeo J., Kovalevskiy O., Tuny Asuvunakool K., Ata La Y Don A. G., Žídek A., Tomlinson H., Hariharan D., Abrahamson J., Green T., Jumper Ji, Velankar S., (2024), "2024'te AlphaFold Protein Yapı Veritabanı: 214 milyondan fazla protein dizisi için yapı kapsamı sağlıyor", Nükleik Asitler, 52, 368–375.

[95] Doğa E. C., (2020), "Her şeyi değiştirecek": DeepMind'ın yapay zekası protein yapılarını çözmede devasa bir sıçrama yapıyor", https://go.gale.com/ps/i.do?id=GALE%7CA649545694&sid=googleScholar&v=2.1&it=r&linkaccess=abs&issn=00280836&p=AONE&sw=w . Accessed Date: May 2025.

[96] "Groups Analysis: zscores- CASP14." https://predictioncenter.org/casp14/zscores_final.cgi . Accessed date: Mar 16, 2025.

[97] Fiser A., Šali A., (2003), “Modeller: generation and refinement of homology-based protein structure models”, In Methods in enzymology, 374, 461-491).

[98] Dayringer H. E., Tramontano A., Sprang S. R., Fletterick R. J., (1986), “Interactive program for visualization and modelling of proteins, nucleic acids and small molecules”, Journal of Molecular Graphics, 4 (2), 82–87.

[99] Hansmann U. H. E., Okamoto Y., (1999), “New Monte Carlo algorithms for protein folding”, Current Opinion in Structural Biology, 9 (2), 177–183.

[100] Fiser A., Do R. K. G., Šali A., (2000), “Modeling of loops in protein structures”, Protein Science: A Publication of the Protein Society, 9 (9), 1753–1773.

[101] Venselaar H., Krieger E., Vriend G., (2000), “Homology Modeling”.

[102] Morris A. L., MacArthur M. W., Hutchinson E. G., Thornton J. M., (1992), “Stereochemical quality of protein structure coordinates”, Proteins, 12 (4), 345–364.

[103] Baumann G., Engineering C. F., (1989), “Polarity as a criterion in protein design”, https://academic.oup.com/peds/article-abstract/2/5/329/1441149 , Mar 18 2025.

[104] Chothia C., Lesk A. M., (1986), “The relation between the divergence of sequence and structure in proteins”, The EMBO Journal, 5 (4), 823–826.

[105] Jumper J., Evans R., Pritzel A., Green T., Figurnov M., Ronneberger O., Hassabis D., (2021), “Highly accurate protein structure prediction with AlphaFold”, Nature, 596 (7873), 583-589.

[106] Tunyasuvunakool K., Adler J., Wu Z., Green T., Zielinski M., Žídek A., Bridgland A., Cowie A., Meyer C., Laydon A., Velankar S., Kleywegt G. J., Bateman A., Evans R., Pritzel A., Figurnov M., Ronneberger O., Bates R., Kohl S. A., (2021), “Highly accurate protein structure prediction for the human proteome”, Nature, 596(7873), 590–596.

[107] Jefferies D., Khalid S., (2021), “Atomistic and coarse-grained simulations of membrane proteins: A practical guide”, Methods, 185, 15–27.

[108] Land H., Humble M. S., (2018), “YASARA: A Tool to Obtain Structural Guidance in Biocatalytic Investigations”, Methods in Molecular Biology, 1685, 43–67.

[109] “holin [*Staphylococcus* faj K]- Protein- NCBI.”. https://www.ncbi.nlm.nih.gov/protein/YP_009041295.1/ . Accessed: Mar. 17, 2025

[110] Guex N., Peitsch M. C., (1997), “ SWISS-MODEL and the Swiss-Pdb Viewer: an environment for comparative protein modeling”, Electrophoresis, 18 (15), 2714-2723.

[111] "Shi Y., Xin Y., Wang C., Blankenship R. E., Sun F., Xu X., (2020), "Cryo-EM structures of the air-oxidized and dithionite-reduced photosynthetic alternative complex III from *Roseiflexus castenholzii* ". Science advances, 6 (31), 2739.

[112] "Shi Y., Xin Y., Wang C., Blankenship R. E., Sun F., Xu X., (2020), " 6LOD: Cryo-EM structures of the air-oxidized and dithionite-reduced photosynthetic alternative complex III from *Roseiflexus castenholzii".* https://www.ncbi.nlm.nih.gov/Structure/pdb/6LOD . Accessed date: Mar 17, 2025.

[113] Laskowski R. A., MacArthur M. W., Moss D. S., Thornton J. M., (1993), "PROCHECK: a program to check the stereochemical quality of protein structures", 26 (2), 283–291.

[114] Hansson T., Oostenbrink C., Van Gunsteren W. F., (2002), "Molecular dynamics simulations", Current Opinion in Structural Biology, 12 (2), 190–196.

[115] Fermi E., Pasta P., Ulam S., Tsingou M., (1955), "Studies of the nonlinear problems (No. LA-1940)", Los Alamos National Laboratory (LANL).

[116] Alder B. J., Wainwright T. E., (1957), "Phase transition for a hard sphere system", The Journal of chemical physics, 27 (5), 1208.

[117] Rahman A., (1964), "Correlations in the motion of atoms in liquid argon", Physical review, 136 (2A), A405.

[118] Berendsen H. J., Postma J. V., Van Gunsteren W. F., DiNola A. R. H. J., Haak J. R., (1984), "Molecular dynamics with coupling to an external bath", The Journal of chemical physics, 81 (8), 3684-3690.

[119] McCammon J. A., Gelin B. R., Karplus M., (1977), "Dynamics of folded proteins", Nature, 267 (5612), 585-590.

[120] Phillips J. C., Braun R., Wang W., Gumbart J., Tajkhorshid E., Villa E., Chipot C., Skeel R. D., Kalé L., Schulten K., (2005), "Scalable molecular dynamics with NAMD", Journal of Computational Chemistry, 26 (16), 1781–1802.

[121] Van Der Spoel D., Lindahl E., Hess B., Groenhof G., Mark A. E., Berendsen H. J. C., (2005), "GROMACS: Fast, flexible, and free", Journal of Computational Chemistry, 26 (16), 1701–1718.

[122] Brooks Bernard R., Bruccoleri R. E., Olafson B. D., States D. J., Swaminathan S., Karplus M., (1983), "CHARMM: A program for macromolecular energy, minimization, and dynamics calculations", Journal of Computational Chemistry, 4 (2), 187–217.

[123] Hospital A., Goñi J. R., Orozco M., Gelpí J. L., (2015), "Molecular dynamics simulations: advances and applications", Advances and Applications in Bioinformatics and Chemistry, 37-47.

[124] González M. A., (2011), “Force fields and molecular dynamics simulations”, École thématique de la Société Française de la Neutronique, 12, 169-200.

[125] Watanabe H., Suzuki M., Ito N., (2011), “Efficient Implementations of Molecular Dynamics Simulations for Lennard-Jones Systems”, Progress of Theoretical Physics, 126 (2), 203–235.

[126] Schwerdtfeger P., Wales D. J., (2024), “100 Years of the Lennard-Jones Potential”, Journal of Chemical Theory and Computation, 20 (9), 3379–3405.

[127] González M. A., (2011), “Force fields and molecular dynamics simulations”, École thématique de la Société Française de la Neutronique, 12, 169-200.

[128] Hospital A., Goñi J. R., Orozco M., Gelpí J. L., (2015), “Molecular dynamics simulations: advances and applications”, Advances and Applications in Bioinformatics and Chemistry, 37-47.

[129] Kolafa J., Perram J. W., (1992), “Cutoff errors in the Ewald summation formulae for point charge systems”, Molecular Simulation, 9 (5), 351-368.

[130] van Gunsteren W. F., Berendsen H. J., (1977), “Algorithms for macromolecular dynamics and constraint Dynamics”, Molecular Physics, 34 (5), 1311-1327.

[131] Andersen H. C., (1983), “Rattle: A “velocity” version of the shake algorithm for molecular dynamics calculations”, Journal of Computational Physics, 52 (1), 24-34.

[132] Hess B., Bekker H., Berendsen H. J., Fraaije J. G., (1997), “LINCS: A linear constraint solver for molecular simulations”, Journal of Computational Chemistry, 18 (12), 1463-1472.

[133] Sharma S., Kumar P., Chandra R., (2019), “Introduction to Molecular Dynamics. Molecular Dynamics Simulation of Nanocomposites Using BIOVIA Materials Studio”, Lammps and Gromacs, 1–38.

[134] Schmidtke P., Bidon-chanal A., Luque F. J., Barril X., (2011), “MDpocket: open-source cavity detection and characterization on molecular dynamics trajectories”, Bioinformatics, 27 (23), 3276–3285.

[135] De Souza O. N., Ornstein R. L., (1997), “Effect of periodic box size on aqueous molecular dynamics simulation of a DNA dodecamer with particle-mesh Ewald method”, Biophysical journal, 72 (6), 2395-2397.

[136] Frenkel D., Smit B., (2023), “Understanding Molecular Simulation: From Algorithms to Applications, Third Edition”, 1–728.

[137] Weiner S. J., Kollman P. A., Nguyen D. T., Case D. A., (1986), “An all atom force field for simulations of proteins and nucleic acids”, Journal of Computational Chemistry, 7 (2), 230–252.

[138] Vanommeslaeghe K., Hatcher E., Acharya C., Kundu S., Zhong S., Shim J., Darian E., Guvench O., Lopes P., Vorobyov I., Mackerell A. D., (2010), "CHARMM general force field: A force field for drug-like molecules compatible with the CHARMM all-atom additive biological force fields", Journal of Computational Chemistry, 31 (4), 671–690.

[139] Wang J., Wolf R. M., Caldwell J. W., Kollman P. A., Case D. A., (2004), "Development and testing of a general Amber force field", Journal of Computational Chemistry, 25 (9), 1157–1174.

[140] Jorgensen W. L., Tirado-Rives J., (1988)," The OPLS [optimized potentials for liquid simulations] potential functions for proteins, energy minimizations for crystals of cyclic peptides and crambin", Journal of the American Chemical Society, 110 (6), 1657–1666.

[141] Ponder J. W., Case D. A., (2003), "Force Fields for Protein Simulations", Advances in Protein Chemistry, 66, 27–85.

[142] Marrink S. J., De Vries A. H., Mark A. E., (2004), "Coarse grained model for semiquantitative lipid simulations", Journal of Physical Chemistry B, 108 (2), 750–760.

[143] Brown D., Clarke J. H. R., (1984), "A comparison of constant energy, constant temperature and constant pressure ensembles in molecular dynamics simulations of atomic liquids", Molecular Physics, 51 (5), 1243–1252.

[144] Jorgensen W. L., Chandrasekhar J., Madura J. D., Impey R. W., Klein M. L., (1983), "Comparison of simple potential functions for simulating liquid water", The Journal of Chemical Physics, 79 (2), 926–935.

[145] Berendsen H. J. C., Postma J. P. M., Van Gunsteren W. F., Hermans J., (1981), "Intermolecular Forces", 331–342.

[146] Khalak Y., Baumeier B., Karttunen M., (2018), "Improved general-purpose five-point model for water: TIP5P".

[150] Robustelli P., Piana S., Shaw D. E., (2018), "Developing a molecular dynamics force field for both folded and disordered protein states", Proceedings of the National Academy of Sciences of the United States of America, 115 (21).

[147] Karplus M., McCammon J. A., (2002), "Molecular dynamics simulations of biomolecules", Nature Structural Biology, 9 (9), 646-652.

[148] MacKerell Jr A. D., Nilsson L., (2008), "Molecular dynamics simulations of nucleic acid–protein complexes", Current Opinion in Structural Biology, 18 (2), 194-199.

[149] Pasquinelli M. A., Yingling Y. G., (2012), "Molecular Dynamics Simulations of Nano-Bio Materials. In Encyclopedia of Nanotechnology", Springer, 1454-1463.

[150] Enkavi G., Javanainen M., Kulig W., Róg T., Vattulainen I., (2019), "Multiscale Simulations of Biological Membranes: The Challenge To Understand Biological Phenomena in a Living Substance", Chemical Reviews, 119 (9), 5607–5774.

[151] Ulmschneider J. P., Ulmschneider M. B., (2018), "Molecular Dynamics Simulations Are Redefining Our View of Peptides Interacting with Biological Membranes", Accounts of Chemical Research, 51 (5), 1106–1116.

[152] Rowlett V. W., Mallampalli V. K. P. S., Karlstaedt A., Dowhan W., Taegtmeyer H., Margolin W., Vitrac H., (2017), "Impact of Membrane Phospholipid Alterations in *Escherichia coli* on Cellular Function and Bacterial Stress Adaptation", Journal of Bacteriology, 199 (13).

[153] Chakraborty A., Kobzev E., Chan J., De Zoysa G. H., Sarojini V., Piggot T. J., Allison J. R., (2021), "Molecular Dynamics Simulation of the Interaction of Two Linear Battacin Analogs with Model Gram-Positive and Gram-Negative Bacterial Cell Membranes", ACS Omega, 6 (1), 388–400.

[154] Brooks B. R., Bruccoleri R. E., Olafson B. D., States D. J., Swaminathan S. A., Karplus M., (1983), "CHARMM: a program for macromolecular energy, minimization, and dynamics calculations", Journal of Computational Chemistry, 4 (2), 187-217.

[155] São-José C., (2018), "Engineering of phage-derived lytic enzymes: improving their potential as antimicrobials", Antibiotics, 7 (2), 29.

[156] Fernandes S., São-José C., (2018), "Enzymes and mechanisms employed by tailed bacteriophages to breach the bacterial cell barriers", Viruses, 10 (8), 396.

[157] S Miyamoto S., Kollman P. A., (1992), "Settle: An analytical version of the SHAKE and RATTLE algorithm for rigid water models", Journal of Computational Chemistry, 13 (8), 952–962.

[158] Hess B., Bekker H., Berendsen H. J., Fraaije J. G., (1997), "LINCS: A linear constraint solver for molecular simulations", Journal of Computational Chemistry, 18 (12), 1463-1472.

[159] Di Pierro M., Elber R., Leimkuhler B., (2015), "A Stochastic Algorithm for the Isobaric-Isothermal Ensemble with Ewald Summations for All Long Range Forces", Journal of Chemical Theory and Computation, 11 (12), 5624–5637.

[160] Kamilla S., Jain, V., (2016), "Mycobacteriophage D29 holin C-terminal region functionally assists in holin aggregation and bacterial cell death", The FEBS Journal, 283 (1), 173-190.

[161] Bavda V. R., Yadav A., Jain V., (2021), "Decoding the molecular properties of mycobacteriophage D29 holin provides insights into holin engineering", Journal of Virology, 95 (10), 10-1128.

[162] Vieira I. H. P., Botelho E. B., de Souza Gomes T. J., Kist R., Caceres R. A., Zanchi F. B., (2023), "Visual dynamics: a WEB application for molecular dynamics simulation using GROMACS", BMC bioinformatics, 24 (1), 107.

[163] Hollingsworth S. A., Dror R. O., (2018), "Molecular Dynamics Simulation for All", Neuron, 99 (6), 1129–1143.

[164] Eisenhaber F., Lijnzaad P., Argos P., Sander C., Scharf M., (1995), "The double cubic lattice method: Efficient approaches to numerical integration of surface area and volume and to dot surface contouring of molecular assemblies", Journal of Computational Chemistry, 16 (3), 273–284.

[165] Grant B. J., Rodrigues A. P. C., ElSawy K. M., McCammon J. A., Caves L. S. D., (2006), "Bio3d: an R package for the comparative analysis of protein structures", Bioinformatics, 22 (21), 2695–2696.

[166] Paradies G., Paradies V., Ruggiero F. M., Petrosillo G., (2019), "Role of cardiolipin in mitochondrial function and dynamics in health and disease: Molecular and pharmacological aspects", Cells, 8 (7).

[167] Renner L. D., Weibel D. B., (2011), "Cardiolipin microdomains localize to negatively curved regions of *Escherichia coli* membranes", Proceedings of the National Academy of Sciences of the United States of America, 108 (15), 6264–6269.

[168] "Bendix", https://sbcb.bioch.ox.ac.uk/Bendix/?utm_source=chatgpt.com . Accessed Date: 20.06.2025

[169] Leonenko Z. V., Finot E., Ma H., Dahms T. E. S., Cramb D. T., (2004), "Investigation of temperature-induced phase transitions in DOPC and DPPC phospholipid bilayers using temperature-controlled scanning force microscopy", Biophysical Journal, 86 (6), 3783–3793.

[170] Wang I. N., Smith D. L., Young R., (2000), "Holins: The protein clocks of bacteriophage infections", Annual Review of Microbiology, 54, 799–825.

[171] Grundling A., Blasi U., Young R., (2000), "Genetic and biochemical analysis of dimer and oligomer interactions of the λ S holin", Journal of Bacteriology, 182 (21), 6082–6090.

[172] Graschopf A., Bläsi U., (1999), "Functional assembly of the λ S holin requires periplasmic localization of its N-terminus", ArMic, 172 (1), 31–39.

[173] Jumper J., Evans R., Pritzel A., Green T., Figurnov M., Ronneberger O., Hassabis D., (2021), "Highly accurate protein structure prediction with AlphaFold", Nature, 596 (7873), 583-589.

[174] Varadi M., Anyango S., Deshpande M., Nair S., Natassia C., Yordanova G., Velankar S., (2022), "AlphaFold Protein Structure Database: massively expanding the structural coverage of protein-sequence space with high-accuracy models", *Nucleic acids research*, *50* (D1), D439-D444.

[175] Lovell S. C., Davis I. W., Arendall W. B., De Bakker P. I. W., Word J. M., Prisant M. G., Richardson J. S., Richardson D. C., (2003), "Structure validation by Cα geometry: φ,ψ and Cβ deviation", Proteins: Structure, Function and Genetics, 50 (3), 437–450.

[176] Ilangumaran Ponmalar, I., Sarangi N. K., Basu J. K., Ayappa K. G., (2021), "Pore Forming Protein Induced Biomembrane Reorganization and Dynamics: A Focused Review", Frontiers in Molecular Biosciences, 8, 737561.

[177] Killian J. A., (1998), "Hydrophobic mismatch between proteins and lipids in membranes", Biochimica et Biophysica Acta- Reviews on Biomembranes, 1376 (3), 401–416.

[178] Monticelli L., Tieleman D. P., Fuchs P. F. J., (2010), "Interpretation of 2H-NMR Experiments on the Orientation of the Transmembrane Helix WALP23 by Computer Simulations", Biophysical Journal, 99 (5), 1455.

[179] Weiss T. M., Van der Wel P. C. A., Killian J. A., Koeppe R. E., Huang H. W., (2003), "Hydrophobic Mismatch between Helices and Lipid Bilayers", Biophysical Journal, 84 (1), 379–385.

[180] Sodt A. J., Sandar M. L., Gawrisch K., Pastor R. W., Lyman E., (2014), "The molecular structure of the liquid-ordered phase of lipid bilayers", Journal of the American Chemical Society, 136 (2), 725–732.

[181] Bläsi U., Fraisl P., Chang C. Y., Zhang N., Young R. Y., (1999), "The C-terminal sequence of the lambda holin constitutes a cytoplasmic regulatory domain", Journal of Bacteriology, 181 (9), 2922–2929.

[182] Zhou B., Wu Y., Su Z., (2021), "Computational simulation of holin S105 in membrane bilayer and its dimerization through a helix-turn-helix motif", The Journal of membrane biology, 254 (4), 397-407.

[183] Brüser T., Mehner-Breitfeld D., (2022), "Occurrence and potential mechanism of holin-mediated non-lytic protein translocation in bacteria", Microbial Cell, 9 (10), 159.

[184] Dewey J. S., Savva C. G., White R. L., Vitha S., Holzenburg A., Young, R., (2010), "Micron-scale holes terminate the phage infection cycle", Proceedings of the National Academy of Sciences of the United States of America, 107 (5), 2219–2223.

[185] Grigor'eva A. E., Bardasheva A. V., Ryabova E. S., Tupitsyna A. V., Zadvornykh D. A., Koroleva L. S., Ryabchikova E. I., (2023), "Changes in the ultrastructure of *Staphylococcus aureus* cells make it possible to identify and analyze the injuring effects of ciprofloxacin, polycationic amphiphile and their hybrid", Microorganisms, 11(9), 2192.

[186] Joodaki F., Martin L. M., Greenfield M. L., (2022), “Generation and Computational Characterization of a Complex Staphylococcus aureus Lipid Bilayer”, Langmuir, 38 (31), 9481–9499.

[187] Huster D., Maiti S., Herrmann A., (2024), “Phospholipid Membranes as Chemically and Functionally Tunable Materials”, Advanced Materials, 36 (23), 2312898.

[188] To K. H., Dewey J., Weaver J., Park T., Young R., (2013), “Functional analysis of a class I holin, P2 Y”, Journal of Bacteriology, 195 (6), 1346-1355.

[189] Young R. F., White R. L., (2008), “Lysis of the host by bacteriophage”, Encyclopedia of Virology, 248-258.

[190] Ramanculov E., Young R., (2001), “Functional analysis of the phage T4 holin in a lambda context”, Molecular Genetics and Genomics, 265 (2), 345–353.

[191] Vukov N., (2002), “Functional analysis of heterologous holin proteins in a lDSthf genetic background”, Doctoral dissertation, Technische Universität München.

[192] Paternoster C., Tarenzi T., Potestio R., Lattanzi G., (2023), “Gamma-Hemolysin Components: Computational Strategies for LukF-Hlg2 Dimer Reconstruction on a Model Membrane”, International Journal of Molecular Sciences, 24 (8), 7113.

BIOGRAPHY

Nurgül ERAYDIN commenced her undergraduate studies in 2017 at Istanbul Arel University, majoring in Molecular Biology and Genetics with a full scholarship. During her undergraduate education, she completed a 6-month internship at Gebze Technical University under the TÜBİTAK 2210-C program. Additionally, she participated in a TÜBİTAK 2209-B funded project for one year. She graduated from her undergraduate program in 2022. In September 2022, she began her master's degree in the Department of Biotechnology at the Graduate School of Gebze Technical University. Throughout her graduate studies, she actively contributed to various projects and served as a scholarship holder in a TÜBİTAK-1001 project for one year. In 2024, she embarked on her professional career as an R&D and Project Specialist. Currently, she continues her work as an Incentive and Project Specialist at a software company focusing on healthcare software solutions.

PUBLICATIONS AND PRESENTATIONS FROM THE THESIS

Nurgul K., Ozbil M., (2023).” Computational evalution of cell membrane destruction by Bacteriophage – K holin protein”, 9th International BAU Drug Design Congress 2023